Relation between the Chiari I malformation and syringomyelia from a mechanical perspective

Karen-Helene Støverud

Thesis submitted for the degree of Philosophiae Doctor
Department of Informatics
Faculty of Mathematics and Natural Sciences
University of Oslo
March 2014

Series of dissertations submitted to the
Faculty of Mathematics and Natural Sciences, University of Oslo
No. 1499

ISSN 1501-7710

Cover: Inger Sandved Anfinsen.
Printed in Norway: AIT Oslo AS.

Produced in co-operation with Akademika Publishing.
The thesis is produced by Akademika Publishing merely in connection with the thesis defence. Kindly direct all inquiries regarding the thesis to the copyright holder or the unit which grants the doctorate.

This thesis consists of an introduction and the following five papers:

Paper I: *Modeling Concentration Distribution and Deformation during Convection-Enhanced Drug Delivery into Brain Tissue*

Published in Transport in Porous Media (2012).
This paper is co-authored with Melanie Darcis, Rainer Helmig, S. Majid Hassanizadeh.

Paper II: *CSF flow in Chiari I and syringomyelia from the perspective of Computational Fluid Dynamics*

Published in The Neuroradiology Journal (2011)
This paper is co-authored with Kent-André Mardal, Victor Haughton, Hans Petter Langtangen.

Paper III: *CSF pressure and velocity in obstructions of the subarachnoid spaces*

Published in The Neurodiology Journal (2013).
This paper is co-authored with Hans Petter Langtangen, Victor Haughton, and Kent-André Mardal.

Paper IV: *Effect of pia mater, central canal, and geometry on wave propagation and fluid movement in the cervical spinal cord*

Submitted to Journal of Biomechanics (2014).
This paper is co-authored with Martin Alnæs, Hans Petter Langtangen, Victor Haughton and Kent-André Mardal

Paper V: *Computational investigation of CSF dynamics in the 4th ventricle, cranial and cervical subarachnoid space*

Technical report (2014).
This paper is co-authored with Kent-André Mardal and Hans Petter Langtangen

Acknowledgments

This thesis is a product of about four years of work at Simula Research Laboratory. It has been a pleasure working in an environment with so many talented people, but it has also been a great challenge and at times I was close to give up. Thanks to all of you who supported, listened, and believed in me throughout these years!

First of all I wish to express my gratitude to my main supervisor Kent-André Mardal for his constant support and availability. He always kept calm, encouraged me, and assured me that I was good enough.

Second, I would like to thank my co-supervisors Victor Haughton and Hans Petter Langtangen. You are both extraordinary capacities that have inspired and taught me a lot through fruitful discussions and close collaborations. A special thanks to Vic and his wife Kirsti who treated me as a family member during my stay in Madison.

Many thanks goes to my office mates Benjamin and Øyvind for helping me communicating with my computer and making me laugh almost every day. My sisters and their families for always reminding me that the world outside science is the most important one. And my parents for their true interest in everything I do and their unconditional love.

Finally, I would like to thank André for his patience, love and support. You are my everything!

Karen-Helene Støverud, Oslo, March 2014

Introduction

Contents

1 Introduction

Chronic pains affect the quality of life of a large number of people in today's society. To help these patients and offer optimal treatment, it is important to understand the underlying cause, the pathogenesis, of the pain. One group of patients suffering from chronic pain is patients with Chiari I. The Chiari I malformation is a neurological condition in which parts of the cerebellum are displaced into the spinal column (see Figure 1.1). Once Chiari I was thought of as a rare disease, but with the advent of Magnetic Resonance Imaging (MRI) an increasing number of patients have been diagnosed, and it has become clear that not all individuals who have Chiari I are symptomatic. This means that if a Chiari I patient is referred to a physician due to severe headaches, the physician still needs to determine whether the headache is related to the Chiari malformation or caused by another mechanism e.g. migraine. In association with Chiari I about 2/3 of the patients develop fluid filled cavities, syrinxes, within the spinal cord tissue (Figure 1.1). These Chiari patients are usually treated by a decompression surgery with the goal of creating more space around the cerebellum. After a decompression surgery the syrinx often resolves. Clinicians, scientists, and engineers have proposed numerous explanations for the pathogenesis of syringomyelia. However, the exact relation between the two conditions remains unknown. This thesis addresses the relation between Chiari I and syringomyelia from a biomechanical perspective, and investigates alternative measures that can help clinicians distinguish Chiari patients who have symptoms related to their malformation.

Biomechanics is the study of mechanical principles in living organisms. Today this is an emerging field in which computer simulations play an important role. Computational mechanics have given new insight to blood flow, heart disease, and bone strength to mention a few. In the near future, it is likely to play an important role also in clinical medicine. In this thesis, we apply computational mechanics to study spinal cord tissue and pulsatile flow of cerebrospinal fluid (CSF). This requires interdisiplinary work; we need knowledge about anatomy and physiology, MR imaging, computer science, fluid and solid mechanics. Reflecting this, we aim at publishing papers both in clinical and mechanical journals.

The thesis consists of an introduction and a collection of papers. The introduction first provides a medical background and a brief introduction to MRI (Section 2 and 3). In Section 4 we define Chiari I and syringomyelia, before a literature review on the topic with emphasis on mechanical models is given in Section 5. In Section 6 the equations used to model the spinal cord tissue

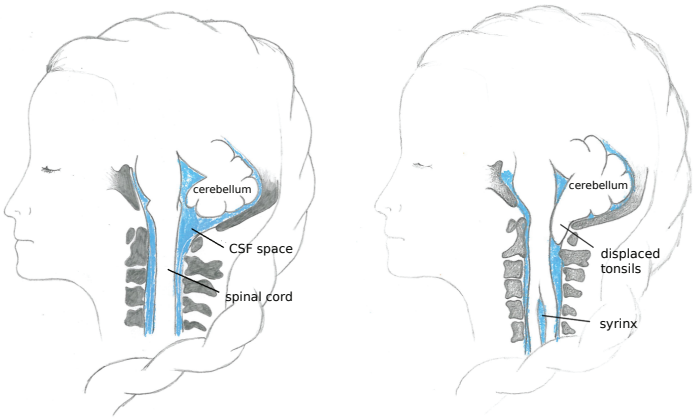

(a) (b)

Figure 1.1: Schematic drawing of the spinal cord, cerebellum, and CSF space in (a) a healthy subject and (b) a Chiari I patient.

and CSF flow are introduced, followed by a note on computationally expensive simulations (Section 7). There are several limitations to the simulations in this study, and in Section 8 we propose future work to improve the current models. Finally, a summary of the papers included in the thesis is given (Section 9).

1.1 A note on Paper I

Before continuing it should be noted that Paper I has a different focus than the remaining papers. It considers Convection-Enhanced Delivery (CED), which is a technique where a therapeutic agent is infused under positive pressure directly into the brain tissue. CED is a promising method for treatment of patients with brain tumors. To predict the concentration distribution computational mechanics has proven to be useful. The paper is included because it uses the same mathematical model as used later in Paper II and Paper IV and because it forms the foundation for the subsequent studies.

1.2 Thesis objectives

The objectives of this thesis are to:

- Simulate CSF flow in healthy subjects and Chiari patients under subject specific anatomy and flow conditions.
- Simulate wave propagation and fluid movement through the spinal cord.
- Relate results from the simulations to syrinx formation and suggest alternative measures for abnormal CSF flow.

1.3 Main results

- Obstructions of the CSF space, as seen in Chiari patients, causes increased pressure gradients and decreased phase lag between velocity and pressure. A significant increase in the pressure drop across the foramen magnum may be used to distinguish a moderate from a severe obstruction (Paper III and V).
- By including parts of the cranial CSF space we reproduced complex flow patterns seen in vivo in Chiari patients [17] (Paper V)
- An open segment of the central canal and/or a stiff and thick pia mater causes increased pressure gradients and enhance fluid flow in the central canal of the spinal cord (Paper II and IV).

2 Anatomy and physiology of the central nervous system

The central nervous system (CNS) includes the brain and the spinal cord, whereas all nerves outside the CNS are part of the peripheral nervous system. Nerve tissue is composed mainly of neurons, glial cells and vasculature. The glial cells support and nourish the nerve cells. Between the neuron and glial cells there is a thin, fluid filled space referred to as the interstitial space (ISF). Within the nerve tissue we distinguish between white matter and gray matter, which are different both in structure and functioning. White matter mainly consist of long axon fibers, while gray matter has a high density of cell bodies. Processing of information requires cell function in the gray matter and communication between gray matter regions through white matter tracts.

The brain can be divided into different regions: Brain stem, cerebellum, cerebral hemisphere and diencephalon [61]. Every part can be subdivided into numerous smaller areas all controlling different body functions, both conscious and unconscious. The outer part of the cerebral hemisphere, the cortex, consists of grey matter, while the inner part mainly consists of white matter. Also the cerebellum (from Latin; the little brain) can be divided into white and grey matter in a similar way. Within the brain there are four interconnected fluid filled cavities, known as the ventricular system.

In the spinal cord the gray matter has an H or a butterfly shape and is surrounded by white matter (Figure 2.1). On the anterior surface of the spinal cord there is a narrow crevice called the anterior median fissure. The anterior median fissure is about 3 mm deep and covered by the pia. In the center of the gray matter we find the central canal; a channel running longitudinally along the spinal cord. Generally the central canal occludes with aging, but larger or smaller fluid-filled segments may remain open [63].

The brain is protected by the rigid skull and the spinal cord by the spine. The spine can be divided into four main regions: cervical, thoracic, lumbar and sacral (Figure 2.2). The spinal cord starts immediately below the brain and extends to the lumbar region. At the base of the skull there is a wide opening, foramen magnum, through which the spinal cord enters and exits the skull. The peripheral and central nervous system is connected through the nerve roots, which origins in the gray matter of the spinal cord. At the level of each vertebra one pair of nerves exits the spinal cord and connects to different parts of the body.

Covering the brain and spinal cord there are three meningeal layers. The outermost is the dura mater, the middle layer is called the arachnoid mater, and innermost the pia mater is situated. The pia is adherent to the brain and spinal cord (Figure 2.1). Between the arachnoid and the pia mater there is a space called the sub-arachnoid space (SAS), which is filled with cerebrospinal fluid (CSF). CSF has similar properties as water [15] and does also occupy the ventricular system of the brain.

The SAS is penetrated by the spinal nerve roots, blood vessels, dental ligaments, and the arachnoid trabeculae [61]. Dental ligaments consist of 21 pairs of thin sheets that connect the pia to the arachnoid mater. The trabeculae consists of a large number of filaments that form a cobweb like structure and becomes a part of the pial membrane.

The SAS and the central canal is hydraulically connected through the interstitial space and perivascular spaces. Perivascular spaces are fluid filled gaps surrounding blood vessels for a short distance as they enter the spinal cord tis-

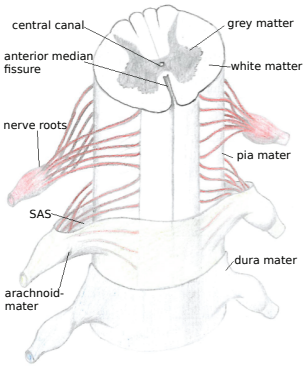

Figure 2.1: Schematic drawing of a segment of the spinal cord displaying the nerves and meningeal layers. In between the arachnoid and pia mater the SAS is located. Gray matter is given a darker shade than white matter. In the center of the grey matter the central canal is indicated. Note that the pia folds into the anterior median fissure.

sue. Elliott [23] estimated that there are about 225 major perivascular spaces along the length of the spinal cord.

CSF is produced in the ventricles by the choroid plexus. The choroid plexus consists of capillaries covered with ephethelial cells through which fluid is secreted. The tight junctions between the endothelial cells prevent the majority of substances from leaving the blood and therefore CSF is a water like fluid where the composition is governed by active transport. Every day about 500 ml CSF is produced and the total volume of the CSF space is about 125 ml, thus the CSF is totally replaced about 4 times each day [46]. This implies that there is a bulk flow from the production sites within the ventricles to the absorption site. Formerly, it was believed that CSF is absorbed exclusively by the arachnoid granulations located in the dura just above the brain. More recently alternative routes have been discovered along the spinal nerves and through the SAS surrounding the cranial nerves entering the nose and eyes [46]. It is also likely that CSF is absorbed by capillaries [31].

In addition to the bulk flow from production to absorption sites there is an oscillatory flow related to the cardiac cycle. With every heartbeat between 0.3 and 1.0 ml CSF is displaced from the cranial SAS towards the spinal SAS

[6, 33, 34]. This oscillatory CSF flow is generated by temporal increase in the blood volume in the CNS during the cardiac cycle. In systole when the heart contracts, CSF leaves the cranial SAS and in diastole when the heart relaxes, CSF returns to the cranium. There are two sources of the CSF pulsations. First, the intracranial pressure generates pressure waves that travel down the spinal canal. Second, there is a direct transfer of the oscillatory pressure in the spinal arteries [42].

The spinal cord is supplied with blood mainly by the anterior spinal artery and the right and left posterior spinal arteries running caudally along the spinal cord. In addition, arteries enter the spinal canal through the same channels as the nerve roots. Below the cervical spine these arteries provide the main blood supply to the spinal canal.

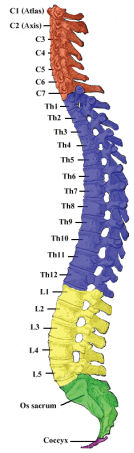

Figure 2.2: Anatomy of the spine indicating the vertebraes. The cervical, thoracic, lumbar, and sacral spine are indicated in red, purple, yellow, and green respectively. (*Illustration from www.wikipidia.org*)

3 Magnetic Resonance Imaging (MRI)

MRI produces high quality medical images of the body and has revolutioned diagnostics in medicine since it was introduced in clinical use in the 1980's. For

an introduction to the basics of MRI the reader is referred to Hashemi et al. [37].

MRI takes advantage of the fact that our body mainly consists of fat and water. Fat and water have an abundance of hydrogen atoms, which act as tiny magnets. The MR scanner sets up a strong magnetic field and a fraction of the protons in the body align with this field. Then radio frequency waves are applied to excite the protons. After the radio frequency pulse is turned off, the atoms eventually return to their initial state, i.e., they align with the magnetic field set up by the scanner, and a signal can be detected by a receiver coil. These signals are decoded through Fourier transformations and turned into spatial images.

The contrast in the image can be weighted, dependent on which anatomical structures or pathologies that are of interest. This is possible because the time it takes from the application of a radiofrequency pulse to recovery of baseline magnetization depends on the tissue type. This recovery time can be divided into two separate processes, referred to as T1 and T2 relaxation. T1 relaxation characterizes the rate at which the magnitude of the magnetization recovers after the radio frequency pulse is applied, while T2 relaxation characterizes the rate at which the transverse component of the magnetization decreases. As mentioned the relaxation time depends on the tissue type. In a T1 weighted MR image water has a low signal; solid tissue an intermediate signal; and fat has a high signal intensity. In a T2 weighted image water has a high signal; solid tissue has an intermediate signal and fat has a low signal intensity. In other words, CSF appears dark on a T1 image and bright on a T2 image, while white matter is brighter than grey matter on a T1 image due to its fatty myelin sheets, in T2 images it is the opposite (see Figure 3.1).

There are numerous MRI modalities used in clinics and for research today. Two of these techniques, to which we will refer later in this thesis, are phase contrast MR (PC MR) and diffusion tensor imaging (DTI). PCMR detects the magnetization's phase shift of hydrogen atoms moving through magnetic field gradients with respect to static hydrogen atom. Based on the phase shift the velocity can be computed [6]. Usually, in 2D imaging only a gradient perpendicular to the chosen slice is encoded, but with three directions encoded the entire velocity vector can be described (Figure 3.2).

In DTI the self diffusion of water within the tissue is measured. Diffusion along a magnetic gradient decreases the signal, i.e, in regions with high diffusion we get low signal intensity. For a heterogeneous and anisotropic medium, such as white matter, the diffusion coefficient takes the form of a full tensor and must be estimated for every voxel. To obtain a full diffusion tensor image the diffusion gradients are therefore applied in at least seven non-parallel directions

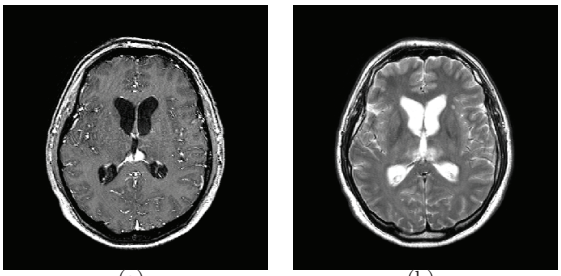

(a) (b)

Figure 3.1: (a) T1 weighted image, where white matter appears white and fluid filled cavities black. (b) T2 weighted image, where white matter appears darker than grey matter and fluid filled cavities appears white.

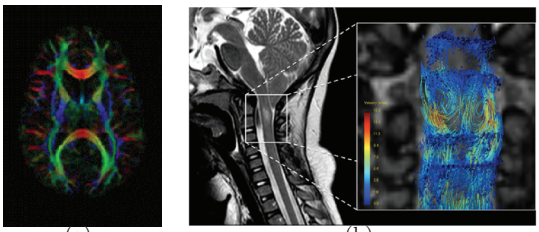

(a) (b)

Figure 3.2: (a) DTI color map (*from Wikipidia*). (b) T2 weighted image of a Chiari patient with corresponding flow field obtained with 4D PCMR (*Courtesy of Bunck et al. [16]*)

[65]. This enables visualization of how the nerve fibers in the white matter are connected (Figure 3.2), and possible damages can effectively be diagnosed.

4 Chiari I and Syringomyelia

4.1 Chiari I Malformation

Chiari malformations were first described by the pathologist Hans Chiari in the 19th century and were graded from 1 to 4 after their severity. In this thesis we do only consider Chiari I, which is a condition were parts of the cerebellar tonsils are displaced into the spinal canal. Figure 1.1 displays a schematic representation and Figure 2.1 displays MR images of the cerebellum and spinal cord in a healthy subject and a Chiari I patient. Displaced tonsils compress the cerebellum, partially obstruct the SAS at the level of foramen magnum and disturb the pulsatile CSF flow. Today a Chiari malformation can be diagnosed with MRI, as a consequence more patients are diagnosed and what was previously thought of as a rare condition is today estimated to affect approximately 1 in 1000 [48].

Chiari patients may experience a wide range of symptoms. The most common symptom is severe headaches located at the back of the skull. The headache usually occurs after coughing, sneezing, or straining. Other symptoms include sleep apnea, hearing or visual disturbances, coordination disorders and muscle weakness. Yet, many patients do not have any symptoms at all and there are no direct correlation between symptoms in Chiari patients and extent to which the cerebellar tonsils are displaced. In addition to pain medication, the most common treatment for symptomatic Chiari I patients is surgery. The procedure is called posterior fossa decompression, in which the surgeon removes part of posterior fossa and the lamina (back of the vertebra) of C1 to give more space to the cerebellum and restore the CSF flow. Often the dura is opened and enlarged to improve the result. How much of the skull that is removed depends on the judgement of the surgeon. In most cases the surgery reduces symptoms and stops the progression of pathologic changes, but it will not reverse damage that already occurred.

When Hans Chiari first discovered the Chiari I malformation in 1891 it was described as a deformation of the cerebellar tonsils in hydrocephalus patients. Later MRI revealed that most Chiari patients do not have hydrocephalus and that it is not the cerebellum itself that is abnormal, but rather the skull. Marin-Padilla and Marin-Padilla [56] measured the size of the posterior fossa in Chiari

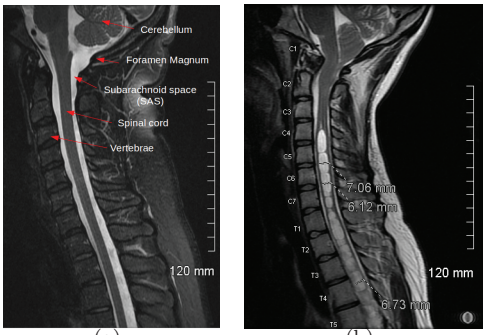

(a) (b)

Figure 4.1: (a) MR image of the cerebellum and spinal cord in a healthy individual. In all pictures white and grey regions indicate fluid and tissue, respectively. (b) Patient with both Chiari I malformation and syringomyelia. The Chiari malformation can clearly be seen by noting how thight the SAS around C1 is. Syringomyelia is identified as the white cavities of CSF within the grey spinal cord from C4 to T4. Notice that the SAS is tight all the way from C1 to T4 in the Chiari patient.

patients and controls and found that Chiari patients have a smaller posterior fossa. A more recent study found that 6 months after a decompression surgery the cerebellar tonsils had close to normal shape [40].

4.2 Syringomyelia

Syringomyelia is a neurological condition characterized by fluid filled cavities (syrinxes) within the spinal cord tissue that may grow over time. Syringomyelia often develops secondary to a Chiari malformation (Figure 1.1). In other cases syrinxes develops after a trauma, after a hemorrhage, in association with a tumor, or in patients with arachnoiditis (inflammation of the arachnoid mater) [49]. Finally, in some cases the cause is unknown and these are categorized as idiopathic. The syrinxes compress tissue, lead to ischemia and cause neurological symptoms. Dependent on the location and size of the syrinx patients experience a variety of symptoms including progressive muscle weakness, chronic severe pain, headache, loss of bladder control and loss of ability to feel hot and cold sensations. In Chiari patients, syrinxes usually form in the cervical spinal cord, otherwise it forms in the vicinity of the damaged region of the spinal

cord. In this thesis the main focus is on the relation between Chiari I and syringomyelia.

In Chiari patients the syrinx may resolve at least partially after decompression surgery. Additional treatments are enlargement of the dura mater and drainage or shunting of the syrinx. Even though the treatments usually stop further detoriation, regeneration of damaged nerve tissue is limited. Therefore it is important to treat patients at an early stage.

5 Literature review

The poor prognosis for untreated syringomyelia has motivated many neurosurgeons, neuroradiologies, engineers, and scientists to study the pathogenesis of the disease. However, despite many proposed theories, the mechanism behind syringomyelia remains unknown. Here we will not try to review all these theories, but rather give a brief introduction to some aspects. For complete reviews of the literature we refer to Klekamp [47], Levine [49], Shaffer et al. [72] and Elliott et al. [25].

5.1 Overview of theories

A common feature of more recent theories is that an abnormal pressure environment results in syrinx formation. Existing theories presume either decreased or increased CSF pressures.

Hyphotetically diminished CSF pressure results in distention and fluid accumulation in the cord. Both the theory by Gardner [29] and the one by Williams [79] are based on transient reduction of the CSF pressure in the spinal SAS. These theories require communication between the fourth ventricle and central canal. Post mortem studies show that in almost all individuals, this passage is occluded and therefore these theories have been rejected. However, more recent theories [31, 32, 47, 49] assume that the CSF pressure is reduced, but they suggest a different origin of the fluid filling the cyst. Transient reduction in CSF pressures results in stress on the spinal cord and, according to these theories, increased fluid flux from the intravascular to the extravascular space and/or decreased absorption of interstitial fluid. The accumulation of fluid results in the development of a syrinx.

Other theories assume increased pressure in the spinal fluid. Increased pressures in the subarachnoid space can arise from a piston action of the cerebellar tonsils, or from coughing, or from the Valsalva maneuver. Hypothetically, ele-

vated pressure in the SAS forces CSF into the spinal cord along the perivascular spaces displacing the tissue in the spinal cord and, eventually, forming a syrinx [7, 39, 66]. The pressure increase may have a short duration or may have a phase shift with respect to the arterial pressure wave within the cord [14]. The theories implicating elevated CSF pressures suggest mechanisms for the accumulation of fluid in the cord. However, these theories do not explain the elevated pressures in the syrinx or expansion of the syrinx in face of larger pressures external to it [32]. To explain this, a valve mechanism based on phase shifts between the arterial and CSF pressure waves has been proposed [14].

In Chiari patients the syrinx is usually situated in the cervical region, but away from the obstructed foramen magnum. To explain these distant syrinxes, Williams [81] proposed the so called slosh effect. Increased pulse pressure in the SAS is transmitted to the fluid in the syrinx generating waves in the walls. The syrinx grows by compressing the upper part of the syrinx which leads to a distension (displacement) of the lower part. This 'slosh' theory has persisted for more than 30 years after it was proposed.

5.2 Velocity measurements

Phase contrast MR is used to quantify CSF flow and velocity. Typically, the acquisition is done at the sagittal mid-line or transversely at the foramen magnum, but recently also volume studies have been published [16, 17]. In healthy subjects the flow is found to be relatively non-uniform in the transverse plane and found to increase from C1 to C4 due to decreased cross-sectional area [74]. In Chiari patients the CSF flow pattern is more complex, has higher local peak velocities, flow jets, and synchronous bidirectional flow [5, 13, 26, 32, 45, 67, 68, 74]. Recent 4D PCMR studies by Bunck et al. [16, 17] also revealed vortex formation in Chiari patients and peak velocities of 15.5 ± 11.3 cm/s compared to 4.7 ± 0.7 in controls. Other studies have observed phase differences between the arterial and CSF systole [26] and a change in duration of systole in Chiari patients compared to controls [5, 13, 67].

Flow measurements before and after decompression surgery contain conflicting results. Some studies report increased peak velocities after surgery [5, 13], while others report decreased peak velocities [21] and a normalization of the averall flow patterns [45].

5.3 Pressure

Since fluid motion is dependent on pressure gradients, velocity obtained from PCMR can be used to obtain an estimate of the corresponding pressures [4]. However, more accurate pressure measurements are invasive and the pressure is measured only at one or a few locations. Williams [79–82] did several experiments measuring pressure in vivo and observed that during coughing and Valsalva maneuver a transient pressure gradient from the head to the spinal cord was present. Measurements show equal [39] or elevated syrinx [35, 63] pressures relative to the SAS.

5.4 Tissue displacement and movement of the cord

The brain expands during systole and contracts during diastole, the same deformation pattern applies to the spinal cord tissue and is often measured as compliance (C). Compliance is defined as the ratio of volume (V) change to pressure (P) change

$$C = \frac{\Delta V}{\Delta P},$$

which means that in a system with high compliance an increase in the volume only causes a small change in pressure. Chiari patients often have lower compliance than controls, but this may improve after a decompression surgery [4, 39, 76].

Apart from deforming, the entire spinal cord and cerebellar tonsils moves during the cardiac cycle. According to Cousins and Haughton [20] the motion in the sagittal direction is about 1mm in both patients and healthy subjects. However, much larger movement has been observed during surgery when the dura is opened [39, 66].

Movement in the anterior/posterior direction and from left to right has also been observed [27, 44, 62]. Hofmann et al. [44] found that in syringomyelia patients the cord moved to a larger extent than in other Chiari patients, potentially causing higher levels of stress within the cord. Note that both displacement of the tissue and movement of the spinal cord affects the CSF velocities and vice versa.

5.5 Interaction between CSF, interstitial fluid and the vasculature

Stoodley et al. [77] investigated the flow of CSF in the spinal cord post-trauma

in rats and sheep using tracer and showed that the tracer spread into the tissue, which implies that there is a fluid exchange between the SAS and spinal cord tissue. From MR imaging it has been found that on T2 images the syrinx appears larger than on a T1 weighted image. According to Fischbein et al. [28], Akiyama et al. [3] and Goh et al. [30] this suggests increased amounts of interstitial fluid in these regions, or edema, because T1 images lacks the discrete cavitations and low signal intensity of CSF that is typical of a syrinx. Based on this observation the three aforementioned studies all suggested that syringomyelia starts as an edema or a presyrinx, but they disagree on the origin of the fluid. Fischbein et al. [28] assume that CSF enters the spinal cord through the perivascular spaces, while Akiyama et al. [3] and Goh et al. [30] argue that interstitial fluid accumulates in the tissue or in the central canal forming a cyst. Decompression surgery is efficient in patients with a pre-syrinx since a pre-syrinx is reversible, which implies that treatment at an early stage is important.

The origin of the syrinx fluid may also be explained by disturbance of aquaporins. Aquaporins are proteins that govern water channels in cell membranes, which conduct water molecules selectively. The presence of aquaporins can increase the permeability of the cell membrane by a factor 10 to 100 and the flow through the membrane is controlled by an osmotic gradient. There exist at least 10-15 different aquaporins and in the brain aqp-4 and aqp-9 are the most prevalent. Aquaporins play a crucial role in controlling the water balance in the central nervous system, but their role in syringomyelia is unclear. In recent clinical studies on rats, in which syrinxes are induced experimentally, the aqp4 levels have been measured. One study showed that aqp4 most likely do not play a role in syrinx formation [1], while two other studies suggest that it might [41, 84].

5.6 Mechanical Models

All the aforementioned studies have provided invaluable information, but do not provide a complete picture of the CSF pressures and velocities, nor the tissue displacement. To get better insight to the mechanics of CSF flow and the spinal cord both physical, mathematical, and numerical models are required. Over the last decades the numbers of papers on the topic have grown rapidly and in the following we review existing studies on CSF mechanics. Here we divide the studies into four categories; pressure wave models, fluid structure interaction (FSI) models, computational fluid dynamics (CFD) models, and models including interstitial fluid flow.

To study the pressure wave propagation in the CSF space co-axial tube

models with analytical solutions have been developed [8, 18, 53], where the outer tube represents the dura and the inner tube the spinal cord.

Lockey et al. [53] modeled the spinal cord as a rigid cylinder and the dura as a thin walled tube. The dura was assumed to behave as an isotropic linear elastic medium, where the radial displacement was dependent on the CSF pressure. The CSF was assumed to be an inviscid incompressible fluid such that the CSF pressure was given by the wave equation and the velocity by the Euler equation. The equations were solved using radial coordinates assuming long wavelength. They investigated speed of the pressure waves in the CSF and the associated longitudinal dura wave speed. Finally, they looked at attenuation of the pressure wave in presence of an obstruction which was introduced by increasing the diameter of the spinal cord. The dura wave speed decreased with increasing blockage of the SAS and increased with increasing dura thickness.

While Lockey et al. [53] assumed a rigid spinal cord and an elastic dura, Berkouk et al. [8] and Carpenter et al. [18] modeled the dura as a rigid tube and the spinal cord as a thin elastic tube. Both the CSF and the spinal cord were assumed to behave as an inviscid, incompressible fluid seperated by a thin elastic membrane (pia). The model was reduced to 1D by assuming that the tube area is a function of a pressure difference across the tube wall. Thus, as a pressure pulse travels along the co-axial tubes the pressure difference causes the inner tube to bulge out and the front of the pressure wave to generate an elastic jump. If there is a block in the outer tube they hypothesized that the pressure wave would be reflected, which could lead to damaging pressure gradients across the tube wall/pia and might cause syrinx formation. However, the wave length and amplitudes found in reality makes this hypothesis unlikely Elliott [22].

Cirovic [19] included both an elastic spinal cord and elastic dura. The geometry consisted of an outer tube and an inner co-axial tube. The center of the inner co-axial tube represents the central canal and the space between the outer and inner tube represents the SAS, both filled with CSF which is assumed to be inviscid. The outer tube representing the dura and the inner tube representing the spinal cord have a finite thickness and are modeled as an isotropic linear elastic medium. To be able to derive an analytical solution the problem was reduced to a 1D dispersion equation and from this characteristic equation, four different wave modes where calculated. The lowest speed was assigned to the dura and the highest speed to the spinal cord. The lowest speed was found to be mainly responsible for generating CSF flow. As the thickness of the spinal cord decreased the lowest speed also decreased, suggesting that low pressure wave speed is found in the presence of a cyst.

Bertram et al. [11] developed a 2D axisymmetrical fluid-structure interaction

(FSI) model where they studied the interaction between CSF flow and pressure distribution in the SAS and stress and deformation in the dura and spinal cord. The CSF was modeled as a viscous incompressible fluid governed by the Navier-Stokes equation. The dura and spinal cord was modeled as an isotropic linear elastic material. In particular they looked at the pressure wave traveling along the spinal cord. The model was further developed to include viscoelasticity, to investigate the effect of a syrinx and obstruction of the SAS [9, 10, 12]. Under certain circumstances,e.g., arachnoiditis, they found increased tensile stress, but the magnitudes were too small to cause tearing of the tissue.

Martin et al. [57, 58] studied pressure in an in vitro model of the spinal canal, estimated the wave speed, found a distinct pressure drop at the level of an obstructed SAS, and found evidence for the slosh mechanism proposed by Williams.

CFD models represents another type of models found in the literature. CFD models assume both the dura and spinal cord to be rigid and simulate CSF flow and pressure by solving the Navier-Stokes equations in idealized [43, 50–52, 55, 78] or patient specific geometries of the SAS [34, 60, 69, 70, 73, 83]. These models give a detailed picture of the flow velocities and pressures under both normal and pathologic conditions. Based on CFD studies it has become clear that viscous and inertial forces are important in CSF flow. Moreover, flow resistance [72] and impedance [60, 73] have been suggested as alternative measures for the severity of a flow obstruction.

All studies mentioned so far assumed the pia mater and/or the spinal cord tissue to be impermeable, but as mentioned the SAS and central canal are hydraulically connected [77].

Bilston et al. [14] studied flow in the perivascular spaces using a co-axial tube model. The outer tube representing the pia was assumed to be rigid, while the inner tube representing the artery wall was assumed to conform to linear elasticity. The annular tube was filled with viscid CSF and the flow governed by the Navier-Stokes equations. At one end of the geometry a pulsatile CSF pressure was applied and along the artery wall a periodic traveling wave of deformation was assigned, simulating the arterial pressure pulse. They found that a phase-shift between the SAS pressure pulse and arterial deformation pulse allow a net inflow to the spinal cord tissue through the perivascular spaces [14].

Martin et al. [59] developed a coupled model of the cardiovascular and CSF system, in which they investigated the correlation of spinal cord blood flow and CSF pulsations along the spinal SAS. A 1D cardiovascular tree model was coupled to a 1D tube model of the spinal canal, i.e., lumping the spinal cord and SAS into one compartment. The coupling was done through a transfer function

based on in vivo measurements of CSF and blood flow. The results showed that the phase shift between blood and CSF flow varied along the spinal canal depending on compliance and vascular anatomy. They also estimated flow in perivascular spaces, which increased with decreased compliance especially in the lumbar region with the highest flow rate.

Another approach was taken by Elliott et al. [24], who developed at lumped parameter model representing the spinal cord, SAS, venous bed and arterial pressure. CSF and blood are mechanically coupled through elasticity of the tissue and vasculature. The venous bed acts as a volume storage space and the vascular pressure as an excitation source. The different compartments are coupled through flow conductance and wall compliance and the model concept based on conservation of mass. Compartment models are zero dimensional so we arrive at a system of ordinary differential equations given on the form:

$$\mathbf{C}\frac{\partial \mathbf{p}(t)}{\partial t} + \mathbf{Z}\mathbf{p}(t) = \mathbf{s}(t) \tag{5.1}$$

where the components of $\mathbf{p}$ are the CSF compartment pressures and $\mathbf{C}$ and $\mathbf{Z}$ are coefficient matrices, $\mathbf{C}$ represents the flow conductance and $\mathbf{Z}$ wall compliance assigned to the boundary between the respective compartments. The conductance between the spinal cord and SAS compartments (the pia mater) is varied periodically with a phase lag with respect to the arterial pressure. The results supports Bilston's theory, but only if the venous system have an intrinsic storage capacity.

The same author [23] followed up with a 1D analytical model including the longitudinal wave as well as the flux through the pia and spinal cord tissue. This is achieved by coupling a co-axial tube model, as already described, with Darcy's law and deriving a damped wave equation. They found that the flux across the pia damped the wave by alleviating hoop stress in the pia. The flux across the pia increased for dilated perivascular spaces, flow obstructions and/or thicker pia mater.

To our knowledge only two studies of syringomyelia using porous media or poroelastic theory have appeared in the literature. Elliott [22] simulated wave propagation in a 1D infinite poroelastic medium. He calculated non-dimensional wave speed and attenuation coefficients for the shear and dilatational wave. Note that in a poroelastic medium there are two dilational waves: one fast and one slow. He concluded that physiologic wave frequencies were too low to have an impact on soft tissue. However, Elliott also noted that a 3D poroelastic model is required to simulate syrinx formation, since a solid spinal cord cannot accumulate fluid.

The second study [36] was a 2D model based on porous media theory with and without a syrinx that evaluated stress in the center of the axisymmetrical spinal cord geometry as a function of time. At the wall of the geometry they applied a constant pressure pulse lasting 4 seconds and then returning to zero.

In summary, all the models mentioned above are simplified and highlight various aspects of the complex dynamics in the CNS. That is, all the investigations have their strengths and weaknesses. Assuming both the dura and spinal cord to be rigid we cannot study the effects of abnormal pressures on the spinal cord or wave propagation. To our knowledge, all the models studying CSF wave propagation have been one or two dimensional. The co-axial models assume an inviscid CSF and both the co-axial tube (apart from [23]) and FSI models assume a solid spinal cord and can thus not accumulate fluid to form a syrinx. In the lumped compartment model we lose spatial information and the perivascular model only investigates one perivascular space and needs to be upscaled.

Mechanical models assume that syringomyelia can be explained by mechanical factors. Mechanics are likely to be part of the answer, but none of the existing studies can explain syrinx formation. The answer might be found if we combine mechanical with biological processes.

6 Mathematical and numerical modeling

Throughout this thesis we will look at mechanical factors relating Chiari I malformations to syringomyelia and measures that can help clinicians distinguish patients that will benefit from treatment from those that will not. Pulsatile flow in the CNS is clearly a fluid-structure interaction (FSI) problem. CSF flow is driven by expansion of the arteries in the brain and there is a continuous exchange of fluid between the vasculature and the tissue and between the tissue and the SAS. In this work we have chosen to model the CSF flow in the SAS assuming rigid impermeable walls, while the spinal cord is modelled separately and treated as poroelastic medium. Moreover, we have not considered the vasculature explicitly. By not including FSI and vasculature we simplify the system to a great extent, resulting in tractable models where the mechanisms of interest can be studied in detail.

In the following we will introduce the equations considered in this thesis. First, we introduce and derive the poroelastic equations used and give the weak form. Second, we introduce the Navier-Stokes equations and describe the splitting scheme used in this thesis to solve the equations. For CSF flow the choice

of model is clear therefore the focus is on the solution scheme. In poroelastic modeling the choice of model is dependent on the process of interest and needs justification.

All simulations (apart from in Paper I) were performed using FEniCS [54], a finite element framework for solving partial differential equations in an automatic manner.

6.1 Poro-elastic modeling of the spinal cord

Based on mechanical testing, the spinal cord has been found to be a soft, non-linearly viscoelastic material. The choice of mechanical model is dependent on the process of interest. Syrinx formation is a slow process involving displacement of interstitial fluid. Therefore, we use a porous media approach, where the neurons, glial cells and vasculature make up the solid phase saturated by interstitial fluid. The interstitial space is highly tortuous and the pore sizes are of nanoscale. Nevertheless, it makes up 20% of the total volume of the spinal cord, in comparison to the vasculature which only occupies 3% [64]. Thus, the spinal cord can be treated as a porous medium with a porosity of 0.2. Figure 6.1 shows a schematic representation of the porous medium approach. As mentioned, the elastic properties of the spinal cord are non-linear, but for small displacements the assumption of linear elasticity is plausible.

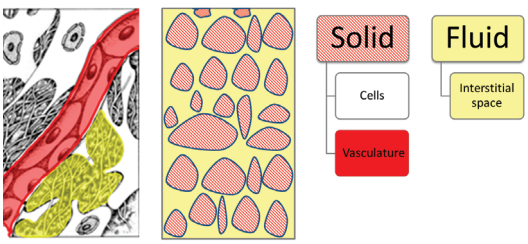

Figure 6.1: Representation of the spinal cord tissue as a porous medium. To the left a schematic drawing of the spinal cord tissue is displayed consisting of cells and capillaries separated by interstitial fluid. The figure to the right displays how the tissue is represented as a porous medium, where the cells and vasculature makes up the solid phase and the interstitial fluid the fluid phase.

In the following we will derive the poroelastic equations from first principles based on Hassanizadeh and Gray [38] and Schanz and Diebels [71].

6.1.1 Momentum balance

To set up a balance of forces in a porous medium, both the fluid and the solid phase have to be considered. To distinguish between the fluid and solid components the subscript f and s are used respectively. For the fluid phase we have the momentum balance equation

$$\int_V \phi\rho_f \frac{D\mathbf{v}_f}{Dt}\mathrm{d}V = \int_V \phi\rho_f \mathbf{g}\mathrm{d}V + \int_S \mathbf{n}\cdot(\phi\mathbf{T}_f)\mathrm{d}S + \int_V \mathbf{F}_{fs}\mathrm{d}V \tag{6.1}$$

and for the solid phase

$$\int_V (1-\phi)\rho_s \frac{D\mathbf{v}_s}{Dt}\mathrm{d}V = \int_V (1-\phi)\rho_s \mathbf{g}\mathrm{d}V - \int_S \mathbf{n}\cdot((1-\phi)\mathbf{T}_s)\,\mathrm{d}S + \int_V \mathbf{F}_{sf}\mathrm{d}V. \tag{6.2}$$

with $\mathbf{v}$ as velocities, ρ partial densities, ϕ porosity, and $\mathbf{T}$ the stress tensors. The operator $\frac{D}{Dt}$ denotes the material time derivative following either a fluid or solid particle (depending on the equation). The gravity force is given by $\mathbf{g}$ term, but will be neglected in the following. The friction force between the fluid and solid phase are represented by $\mathbf{F}_{sf}$ and $\mathbf{F}_{fs}$ and according to Newton's 3rd law these forces cancel each other out. The porosity ϕ enters the integrals since we are to integrate over the fluid or the solid, and the fluid occupies a fraction ϕ of the volume or surface, while the solid occupies the remaining fraction $1-\phi$. From the integral balance equations above we apply Gauss' theorem to the surface integrals and derive the corresponding partial differential equations

$$\phi\rho_f \frac{D\mathbf{v}_f}{Dt} = \phi\rho_f \mathbf{g} + \nabla\cdot(\phi\mathbf{T}_f) + \mathbf{F}_{fs} \tag{6.3}$$

$$(1-\phi)\rho_s \frac{D\mathbf{v}_s}{Dt} = (1-\phi)\rho_s \mathbf{g} - \nabla\cdot((1-\phi)\mathbf{T}_s) + \mathbf{F}_{sf} \tag{6.4}$$

Adding equations (6.4) and (6.3), neglecting acceleration of the fluid and gravity forces result in the momentum balance for the fluid-solid mixture

$$(1-\phi)\rho_s \frac{D\mathbf{v}_s}{Dt} = -\nabla\cdot((1-\phi)\mathbf{T}_s + \phi\mathbf{T}_f)\,. \tag{6.5}$$

For the fluid phase the stress tensor is governed by the hydrostatic pressure and reduces to $\mathbf{T}_f = -p\mathbf{I}$. That is, the extra stress $\boldsymbol{\sigma}_f^E$ due to viscous forces are negligible in the divergence term, but the friction between the fluid and solid

because of viscous effects is substantial. However, this effect must be averaged and is modeled by the exchange terms $\mathbf{F}_{sf}$ and $\mathbf{F}_{fs}$. For the solid phase we need to take the internal stresses $\boldsymbol{\sigma}_s^E$ into account and set $\mathbf{T}_s = \boldsymbol{\sigma}_E - p\mathbf{I}$. Now the total stress tensor is given by

$$\mathbf{T}_T = (1-\phi)\mathbf{T}_s + \phi\mathbf{T}_f = (1-\phi)(\boldsymbol{\sigma}_s^E - p\mathbf{I}) - \phi p\mathbf{I} \approx \boldsymbol{\sigma} - p\mathbf{I}. \tag{6.6}$$

For linear elasticity the displacement vector $\mathbf{u}$ can be related to the strain tensor

$$\boldsymbol{\epsilon} = \frac{1}{2}(\nabla\mathbf{u} + \nabla^T\mathbf{u}). \tag{6.7}$$

Assuming an isotropic, linear elastic medium, it can be shown that the following linear stress-strain relation holds:

$$\boldsymbol{\sigma} = 2\mu\boldsymbol{\epsilon} + \lambda(\mathrm{tr}\boldsymbol{\epsilon})\mathbf{I} \tag{6.8}$$

where μ and λ represent Lamé parameters.

For small deformations,

$$\frac{D\mathbf{v}_s}{Dt} \approx \frac{\partial^2\mathbf{u}}{\partial^2 t}.$$

Substituting (6.8) and (6.7) into (6.5) and rearranging yields

$$(1-\phi)\rho_s\frac{\partial^2\mathbf{u}}{\partial^2 t} = \nabla\cdot\big(\mu(\nabla\mathbf{u} + \nabla^T\mathbf{u}) + \lambda(\nabla\cdot\mathbf{u})\mathbf{I}\big) - \nabla p. \tag{6.9}$$

It is common to neglect the acceleration term on the left-hand side when we do not want to include fast sound waves in the model. From now on we therefore omit this term.

The Lamé parameters are used to characterize the elasticity of a medium and are related to the Poisson ratio ν and Young's modulus E as follows:

$$\lambda = \frac{E\nu}{(1+\nu)(1-2\nu)}, \qquad \mu = \frac{E}{2(1+\nu)} \tag{6.10}$$

High values of μ and λ implies a stiff material.

6.1.2 Volume balance

Assuming the density of the solid and the fluid phase to be constant, the mass balance can be transformed to a volume balance: For the solid phase we have

$$\frac{\partial(1-\phi)}{\partial t} + \nabla\cdot((1-\phi)\cdot\mathbf{v}_s) = 0 \tag{6.11}$$

and for the fluid phase we have

$$\frac{\partial \phi}{\partial t} + \nabla \cdot (\phi \mathbf{v}_f) \pm \Omega_F(\mathbf{x}, t) = 0, \tag{6.12}$$

where Ω_F is a sink/source term for the fluid phase. Adding (6.11) and (6.12) yields

$$\nabla \cdot (\phi \mathbf{v}_f + (1 - \phi)\mathbf{v}_s) \pm \Omega_F(\mathbf{x}, t) = 0. \tag{6.13}$$

In the case of infinitesimal deformation,

$$\mathbf{v}_s = \frac{\partial \mathbf{u}}{\partial t}. \tag{6.14}$$

The fluid velocity $\mathbf{v}_f$ can be derived from the momentum balance of the fluid (6.4), and again by neglecting acceleration of the fluid we obtain

$$-\nabla \cdot (\phi p \mathbf{I}) + \mathbf{F}_{fs} = 0. \tag{6.15}$$

As mentioned, $\mathbf{F}_{sf}$ represents the friction forces between the solid and fluid phases, which is modeled by the linear relation

$$\mathbf{F}_{sf} = p \nabla \phi - \mathbf{R}(\mathbf{v}_f - \mathbf{v}_s), \tag{6.16}$$

where $\mathbf{R}$ is a second order tensor arising from the linearization of $\mathbf{F}_{sf}$. Replacing $\mathbf{F}_{sf}$ in Equation (6.15) yields

$$-\nabla \cdot (\phi p \mathbf{I}) + p \nabla \phi - \mathbf{R}(\mathbf{v}_f - \mathbf{v}_s) = 0 \tag{6.17}$$

$$\mathbf{v}_f = -\phi \mathbf{R}^{-1} \nabla p + \mathbf{v}_s. \tag{6.18}$$

Finally, $\mathbf{R}$ can be related to the conductivity of the porous medium [38]

$$\mathbf{R}^{-1} := \frac{\mathbf{K}}{\mu_w}. \tag{6.19}$$

Substituting (6.14) and (6.18) in (6.13) and rearranging yields the final form of the fluid-solid mixture volume balance

$$\nabla \cdot \left(\frac{\partial \mathbf{u}}{\partial t} - \frac{\mathbf{K}}{\mu_w} \nabla p \right) = \Omega_F(\mathbf{x}, t). \tag{6.20}$$

6.1.3 Weak Formulation

We start by restating the equations in its strong form; for a domain $\Omega \subset \mathbb{R}^d$ find $\mathbf{u}$ and p satisfying

$$\nabla \cdot \left(\frac{\partial \mathbf{u}}{\partial t} - \frac{\mathbf{K}}{\mu_w} \nabla p \right) = \Omega_F(\mathbf{x}, t) \qquad \text{in} \quad \Omega \tag{6.21}$$

$$\nabla \left(\cdot \mu \nabla \mathbf{u} \right) + \nabla \left(\left(\lambda + \mu \right) \nabla \cdot \mathbf{u} \right) - \nabla p = 0 \qquad \text{in} \quad \Omega. \tag{6.22}$$

In (6.22) we used the following relation:

$$\nabla \cdot \nabla^T \mathbf{u} = \nabla \cdot (\nabla \cdot \mathbf{u}) \mathbf{I} = \nabla (\nabla \cdot \mathbf{u}). \tag{6.23}$$

We introduce a mixed variational formulation where the pressure and displacement are approximated simultaneously. First, we multiply (6.21) and (6.22) by test functions q and $\mathbf{w}$ and integrate the divergence terms by parts. This gives us the variational problem: find $\mathbf{u} \in W$ and $p \in Q$ such that

$$\int_\Omega \left[\nabla \cdot \left(\frac{\partial \mathbf{u}}{\partial t} \right) q + \frac{\mathbf{K}}{\mu_w} \nabla p \cdot \nabla q \right] \mathrm{d}\mathbf{x} = \int_\Omega \Omega_F(\mathbf{x}, t) q \mathrm{d}\mathbf{x} + \int_{\Gamma_N} f_n q \mathrm{d}\mathbf{s} \tag{6.24}$$

$$\int_\Omega \left[-\mu \nabla \mathbf{u} : \nabla \mathbf{w} - \left(\lambda + \mu \right) (\nabla \cdot \mathbf{u})(\nabla \cdot \mathbf{w}) + (\nabla \cdot \mathbf{w}) p \right] \mathrm{d}\mathbf{x} = \int_{\Gamma_N} \mathbf{T}_n \cdot \mathbf{w} \mathrm{d}\mathbf{s} \tag{6.25}$$

holds for all $\mathbf{w} \in W$ and $q \in Q$. Here, $\mathbf{T}_n$ represents the normal stress and f_n the normal flux along the Neuman boundary, Γ_N, of the domain Ω.

In the current study we use continuous piecewise linear elements for both pressure and displacement, which saves computational time but are known to cause unphysical pressure oscillations in regions with high pressure gradients. To avoid such pressure oscillations we add the following stabilization term to (6.24) from [2]:

$$\beta \int_\Omega \nabla \left(\frac{\partial p}{\partial t} \right) \cdot \nabla q \, \mathrm{d}\mathbf{x}, \tag{6.26}$$

where $\beta = \frac{h^2}{4(\lambda + 2\mu)}$. To discretize in time, we employ a backward Euler discretization, and after adding the perturbation term, the variational form becomes: find $\mathbf{u} \in \mathbf{W}$ and $p \in Q$ such that

$$\int_\Omega \left[(\nabla \cdot \mathbf{u}) q + \Delta t \frac{\mathbf{K}}{\mu_w} \nabla p \cdot \nabla q + \nabla p \cdot \nabla\, q \right] \mathrm{d}\mathbf{x}$$
$$= \int_\Omega \left[\Delta t \Omega_F(\mathbf{x}, t) q + (\nabla \cdot \mathbf{u}^{k-1}) q + \nabla\, p^{k-1} \cdot \nabla q \right] \mathrm{d}\mathbf{x} + \int_{\Gamma_N} f_n \mathrm{d}\mathbf{s} \quad (6.27)$$

$$\int_\Omega \left[-\mu \nabla \mathbf{u} : \nabla \mathbf{w} - (\lambda + \mu) (\nabla \cdot \mathbf{u})(\nabla \cdot \mathbf{w}) + (\nabla \cdot \mathbf{w}) p \right] \mathrm{d}\mathbf{x} = \int_{\Gamma_N} \mathbf{T}_n \cdot \mathbf{w} \mathrm{d}\mathbf{s} \quad (6.28)$$

holds for all $\mathbf{u} \in \mathbf{W}$ and $p \in Q$.The superscript $k-1$ labels quantities at the previous time step.

6.2 Modeling CSF flow in the SAS

The SAS is, as mentioned, penetrated by spinal nerves, dental ligaments and the trabeculae. The boundaries of the SAS represents the dura mater and the pia mater lining the spinal cord. Both the spinal cord and the dura mater are elastic and the spinal cord is permeable. In this work we neglected fine structures and assumed rigid walls. Under these assumptions, the fluid dynamics can be described by the Navier-Stokes equations. These models are often referred to as computational fluid dynamics (CFD).

6.2.1 Navier-Stokes Equations

To simulate pulsatile CSF flow through the spinal SAS, we applied the Navier-Stokes equations for an incompressible Newtonian fluid

$$\frac{\partial \mathbf{u}}{\partial t} + \mathbf{u} \cdot \nabla \mathbf{u} - \nabla \cdot \boldsymbol{\sigma}(\mathbf{u}, p) = \mathbf{g}, \qquad \text{in } \Omega, \quad (6.29)$$
$$\nabla \cdot \mathbf{u} = 0, \qquad \text{in } \Omega. \quad (6.30)$$

Here, $\boldsymbol{\sigma}$ is the Cauchy stress tensor, which is dependent on the strain tensor $\boldsymbol{\epsilon}$ and for a Newtonian fluid $\boldsymbol{\sigma}$ is given by

$$\boldsymbol{\sigma}(\mathbf{u}, p) = 2\nu \boldsymbol{\epsilon}(\mathbf{u}) - p\mathbf{I}, \quad (6.31)$$
$$\boldsymbol{\epsilon}(\mathbf{u}) = \frac{1}{2} \left(\nabla \mathbf{u} + \nabla^T \mathbf{u} \right). \quad (6.32)$$

The primary variables $\mathbf{u}$ and p describe the unknown CSF velocity and pressure, respectively, $\nu = \frac{\mu}{\rho}$ is the kinematic viscosity, which is dependent on the fluid

density ρ and the dynamic viscosity μ, and $\mathbf{g}$ denotes the gravity. CSF is, as mentioned, a water-like fluid and behaves as a Newtonian fluid with ρ and μ similar to water at body temperature [15]. The gravity term in equation 6.29 can be neglected under the assumption that $\mathbf{g}$ is balanced by the hydrostatic pressure. To calculate the correct physical pressure, static pressure resulting from body forces has to be added to the dynamic pressure calculated.

6.2.2 Incremental Pressure Correction Scheme (IPCS)

To solve the Navier–Stokes equation we applied a semi–implicit incremental pressure correction scheme (IPCS). The first step in this scheme is to compute a tentative velocity, u^*, using the pressure from the previous time step in equation (6.29):

$$\frac{\mathbf{u}^* - \mathbf{u}^{n-1}}{\Delta t} + \left(\tfrac{3}{2}\mathbf{u}^{n-1} - \tfrac{1}{2}\mathbf{u}^{n-2}\right) \cdot \nabla \mathbf{u}^* - \nabla \cdot \boldsymbol{\sigma}\left(\mathbf{u}^{n-\frac{1}{2}}, p^{n-1}\right) = \mathbf{g}, \quad \text{in} \quad \Omega. \tag{6.33}$$

Note that a backward Euler time discretization was used, apart from in the advection term where we used the velocity from the previous time steps, $\mathbf{u}^{n-1}$ and $\mathbf{u}^{n-2}$, which resulted in a semi-implicit scheme in time. The weighting in the advection term should make the scheme more stable [75].

In the next step the velocity is projected into the space of divergence free vector fields. Hence, the continuity equation must be satisfied. This projection results in an equation similar to Darcy's law:

$$\frac{\mathbf{u}^n - \mathbf{u}^*}{\Delta t} + \nabla\left(p^n - p^{n-1}\right) = 0 \tag{6.34}$$

$$\nabla \cdot \mathbf{u}^n = 0 \tag{6.35}$$

To solve these equations we need the corrected pressure, p^n, which can be obtained by taking the divergence of (6.34) and using relation (6.35):

$$\nabla^2 p^n = \nabla^2 p^{n-1} + \frac{\nabla \cdot \mathbf{u}^*}{\Delta t} \tag{6.36}$$

Finally, $\mathbf{u}^n$ can be found by rearranging (6.34),

$$\mathbf{u}^n = \mathbf{u}^* - \Delta t \nabla\left(p^n - p^{n-1}\right) \tag{6.37}$$

Thus, first the problem is discretized in time and an operator splitting is performed. Then, each of the equations (6.33) to (6.37) need to be written in

the weak form and discretized in space by the finite element method. We start with writing Equation (6.33) on weak form: find $\mathbf{u}^* \in \mathbf{V}$ such that

$$\int_\Omega \left(\frac{\mathbf{u}^* - \mathbf{u}^{n-1}}{\Delta t} \ \mathbf{v} + \mathbf{u}^{n-1} \cdot \nabla \mathbf{u}^* \ \mathbf{v} + \boldsymbol{\sigma}(\mathbf{u}^{n-\frac{1}{2}}, p^{n-1}) \right) \ d\mathbf{x} + \int_{\partial\Omega} \left(p^{n-1} \mathbf{n} \mathbf{v} - \nu \mathbf{n} \cdot \left(\nabla \mathbf{u}^{n-\frac{1}{2}} \right)^T \right) \ d\mathbf{s} = \int_\Omega \mathbf{g} \ \mathbf{v} \ d\mathbf{x}. \quad (6.38)$$

Then we do the same for Equation (6.37): find $p^n \in Q$ such that

$$\int_\Omega \nabla p^n \cdot \nabla q \ d\mathbf{x} = \int_\Omega \left(\nabla p^{n-1} \cdot \nabla q - \frac{1}{\Delta t} \left(\nabla \cdot \mathbf{u}^* \right) \ q \right) \ d\mathbf{x}. \quad (6.39)$$

Finally, we compute the velocity at the new time step: find $\mathbf{u}^n \in \mathbf{V}$ such that

$$\int_\Omega \mathbf{u}^n \ \mathbf{v} \ d\mathbf{x} = \int_\Omega \left(\mathbf{u}^* \ \mathbf{v} - \Delta t \left(\nabla p^n - \nabla p^{n-1} \right) \ \mathbf{v} \right) \ d\mathbf{x}. \quad (6.40)$$

This set of equations is implemented in the FEniCS [54] application `cbc.flow`. To speed up the computations we used first order elements for both pressure and velocity.

The Poisson equation resulting from the projection scheme requires an additional boundary condition for the pressure. In this study we used homogenous Neumann boundary condition for the pressure on all boundaries. For the velocity Dirichlet conditions are employed. At the inflow and outflow boundaries time dependendent velocity conditions are enforced, while along the rigid walls a no-slip boundary condition is used.

7 Computationally Expensive Simulations

Subject-specific models have complex geometries, which result in computational meshes consisting of several millions cells. In Paper IV the meshes used had between 1 and 3 million cells and the poroelastic equations were solved for about 700 time steps. The meshes in Paper V had between 8 and 18 million cells and in this study we solved the Navier-Stokes equations for about 20 000 time steps. To solve the Navier-Stokes equations or poro-elastic equations is computationally expensive and requires parallelization for such large meshes. This would not have been possible without having access to a powerful computer

cluster. For Paper IV and V we used approximately 300 000 CPU hours on Abel, the computer cluster at the University of Oslo.

After running the simulation you face the challenge of a large data set and postprocessing requires a lot of memory and becomes a significant part of the work[1].

To speed up the simulations and limit the size of the output there is clearly a need for improved numerical methods, faster algorithms, and efficient strategies for saving only relevant output.

8 Limitations and Future Work

As mentioned, we have modeled the spinal cord and SAS separately and thereby neglected FSI effects. In Paper IV, considering wave propagation through a poroelastic model of the spinal cord, we estimated the CSF pressure wave velocity and prescribed it in the boundary condition applied to the pia mater. In Paper III and V, where we simulated pulsatile CSF flow, we assumed rigid walls and thereby eliminated a dampening effect on pressure gradients, neglected pressure waves and ignored volume changes or compliance. In the future, CSF flow in the SAS should be coupled to the poroelastic model in the SAS.

In Paper III and V we also assumed laminar flow and neglected fine anatomical structures that may explain discrepancies between CFD studies and PCMR. Fine structures should be included in future studies and the assumption of laminar flow needs to be tested, especially, in the case of severe obstructions in the SAS.

For the poro-elastic model most of the material parameters cannot be specified exactly, because the parameters are usually obtained experimentally from animal cadavers. Moreover, the assumption of linear elasticity might be too simplistic and viscoelastic effects should be investigated.

Finally, the subject-specific modeling in this thesis is dependent on MRI data and pressure measurements, which has two major challenges. First, there are uncertainties in the measurements. Anatomical MR data has limited spatial resolution, which influences the accuracy of geometric models. PCMR has in addition limited temporal resolution and for the low velocities found in CSF, the signal to noise ratio is low. Since we use PCMR data as boundary conditons

[1]We tried using an alternative cluster, but since the server was situated in the US the transfer speed was low and it took days or even weeks to download the simulation results. In the end they sent me an external hard disk with approximately 1 TB of data by ordinary mail.

uncertainties in the PCMR data lead to uncertainties in the simulation results. Pressure measurements are, as mentioned, only obtained at one or a few locations and the accuracy is dependent on calibration of the sensors. Second, we need access to large data bases of multimodal data, preferably consisting of anatomical MR images, PCMR data from several planes through the SAS, and pressure measurements.

Optimally, the results in Paper V, where we used velocity boundary conditions based on PCMR data, should be compared with results using subject specific pressure boundary conditions. However, this was not possible since we did not have MRI data and pressure measurements from the same patients. A main goal for future studies is to obtain high quality multimodal data that can be used to validate the computational models.

9 Summary of papers

The papers are listed in chronological order, which reflects the path towards 3D subject-specific models of CSF flow in the SAS (Paper V) and wave propagation in the spinal cord (Paper IV). Paper I laid the foundation for us to treat the spinal cord tissue as a porous medium in Paper II. However, Paper II considers the effect of a static pressure gradient, which is unrealistic given that pressure gradients in the CSF are related to the cardiac cycle or extreme events such as coughing or the Valsalva maneuver. In Paper IV we, therefore, simulated pressure wave propagation through the spinal cord using pressure measurements of the cardiac cycle. In Paper III we used idealized geometries representing the SAS and simulated CSF flow varying as sine function in time. In Paper V we simulated CSF flow under more realistic conditions using subject specific anatomy and flow conditions.

9.1 Paper I

Convection-Enhanced drug Delivery (CED) is a technique where a therapeutic agent is infused under positive pressure directly into the brain tissue. For predicting the final concentration distribution and optimizing infusion rate and catheter placement, numerical models can be of great help. However, despite advances in modeling this process, often the infused agent does not reach the targeted region prescribed in the modeling phase. In this study, patient-specific brain structure and parameters, obtained from Diffusion Tensor Imaging (DTI), were implemented in a numerical model which described the flow and trans-

port in an elastic deformable matrix. To our knowledge this is the first time that information from DTI is used in a numerical model which includes both transport of a therapeutic agent and tissue deformation. Our results showed that preferential flow occurs in the direction of the white matter fiber tracts. The current model assumes linear deformation, corresponding to small porosity changes. But, because large porosity changes occur that may adversely affect drug transport, non-linear deformations should be included in the future.

9.2 Paper II

The purpose of this study was to analyze the role of CSF pressure in the pathogenesis of syringomyelia, with computational models. The spinal cord was modeled as a cylindrical poro-elastic structure with homogenous and isotropic permeability. The permeability was then made heterogeneous and anisotropic to represent the different properties of the central canal, gray and white matter. Fluid with a defined pressure was prescribed in the SAS. Simulations were performed to quantify deformations and fluid movement within the cord.

Pressure gradients in the SAS produce movement of fluid in the spinal cord. Assuming different relative permeability in gray matter, white matter and the central spinal canal, abnormal CSF gradients lead to accumulation of fluid within and adjacent to the spinal cord central canal.

9.3 Paper III

Obstruction of CSF flow, according to some theories, produces a pressure drop in the subarachnoid space in accordance with the Bernoulli theorem, that explains the development of syringomyelia below the obstruction. However, Bernoulli's principle applies to inviscid stationary flow unlike CSF flow. Therefore, we perform a series of computational experiments to investigate the relationship between pressure drop, flow velocities, and obstructions under physiologic conditions.

We created geometric models with dimensions approximating the spinal subarachnoid space with varying degrees of obstruction. Pressures and velocities for constant and oscillatory flow of a viscid fluid were calculated with the Navier-Stokes equations.

The results demonstrated that inertia and viscosity which are not factored into the Bernoulli equation affect CSF flow. Obstruction of CSF flow in the cervical spinal canal increases pressure gradients and velocities and decreases the phase lag between pressure and velocity.

9.4 Paper IV

In this paper we modeled the spinal cord tissue as a poro-elastic medium and simulated the propagation of pressure waves through an anatomically realistic 3D geometry, with boundary conditions based on in vivo CSF pressure measurements.

The results showed that an open segment of the central canal and a stiff and thick pia mater, both typical for arachnoiditis patients, increase the radial pressure gradients and enhance interstitial fluid flow in the central canal. Together with an obstruction of the CSF space these factors may theoretically lead to syrinx formation.

9.5 Paper V

In the last paper included in this study, we used computational fluid dynamics (CFD) to simulate CSF flow and pressure in the cervical SAS, cranial SAS, and 4th ventricle in two Chiari patients and one control under subject-specific anatomy and flow conditions.

By incorporating a larger portion of subject-specific anatomy, the study aimed at bridging the gap formely seen between CFD models and 4D PCMR measurements. This study reproduced flow jets and vortices seen in 4D PCMR. However, our simulations did not explain preferential CSF flow in the posterior cervical SAS.

The obstruction at the level of FM caused a phase shift of the pressure relative to the velocity in one patient. Peak systolic velocities and flow resistance distinguished the Chiari patients from the patient with normal flow conditions, while peak pressure drop distinguished the patient with the most severe obstruction from the patient with a moderate obstruction. A conclusion is that resistance and peak velocities are useful measures to identify an obstruction caused by the cerebellar tonsil herniation, while increased pressure drops across FM indicate the severity of the obstruction.

References

[1] K. Aghayev, E. Bal, T. Rahimli, M. Mut, S. Balci, F. Vrionis, and N. Akalan. Expression of water channel aquaporin-4 during experimental syringomyelia: laboratory investigation. *Journal of Neurosurgery: Spine*, 15(4):428–432, 2011.

[2] G. Aguilar, F. Gaspar, F. Lisbona, and C. Rodrigo. Numerical stabilization of Biot's consolidation model by a perturbation on the flow equation. *International Journal for Numerical Methods in Engineering*, 75(11):1282–1300, 2008. ISSN 00295981. doi: 10.1002/nme.2295.

[3] Y. Akiyama, I. Koyanagi, K. Yoshifuji, T. Murakami, T. Baba, Y. Minamida, T. Nonaka, and K. Houkin. Interstitial spinal-cord oedema in syringomyelia associated with Chiari type 1 malformations. *Journal of Neurology, Neurosurgery and Psychiatry*, 79:1153–1158, 2007.

[4] N. Alperin, M. Mazda, T. Lichtor, and S. H. Lee. From cerebrospinal fluid pulsation to noninvasive intracranial compliance and pressure measured by MRI flow studies. *Current Medical Imaging Reviews*, 2:117–129, 2006.

[5] R. A. Armonda, C. M. Citrin, T. Foley, and R. G. Ellenbogen. Quantitative cine-mode magnetic resonance of Chiari I malformation: An analysis of cerebrospinal fluid dynamics. *Neurosurgery*, 35(2):214–224, 1994.

[6] O. Balédent. *Adult Hydrocephalus*, chapter Imaging of the cerebrospinal fluid circulation, pages 121–138. Cambridge university press, 2014.

[7] M. J. Ball and A. D. Dayan. Pathogenesis of syringomyelia. *The Lancet*, pages 799–801, 1972.

[8] K. Berkouk, P. W. Carpenter, and A. D. Lucey. Pressure wave propagation in fluid-filled co-axial elastic tubes part 1: Basic theory. *Journal of Biomechanical Engineering*, 125(6):852, 2003. ISSN 01480731. doi: 10.1115/1.1634280.

[9] C. D. Bertram. A numerical investigation of waves propagating in the spinal cord and subarachnoid space in the presence of a syrinx. *Journal of Fluids and Structures*, 25(7):1189–1205, 2009. ISSN 08899746. doi: 10.1016/j.jfluidstructs.2009.06.008.

[10] C. D. Bertram. Evaluation by fluid/structure-interaction spinal-cord simulation of the effects of subarachnoid-space stenosis on an adjacent syrinx. *Journal of Biomechanical Engineering*, 132(6), 2010. ISSN 1528-8951. doi: 10.1115/1.4001165.

[11] C. D. Bertram, A. R. Brodbelt, and M. A. Stoodley. The origins of syringomyelia: Numerical models of fluid/structure interactions in the spinal cord. *Journal of Biomechanical Engineering*, 127(7):1099, 2005. ISSN 01480731. doi: 10.1115/1.2073607.

[12] C. D. Bertram, L. E. Bilston, and M. A. Stoodley. Tensile radial stress in the spinal cord related to arachnoiditis or tethering: a numerical model. *Medical & Biological Engineering & Computing*, 46(7):701–7, 2008. ISSN 1741-0444. doi: 10.1007/s11517-008-0332-0.

[13] R. A. Bhadelia, A. R. Bogdan, S. M. Wolpert, S. Lev, B. A. Appignani, and C. B. Heilman. Cerebrospinal fluid flow waveforms: Analysis in patients with Chiari I malformation by means of gated phase-contrast MR imaging velocity measurements. *Radiology*, 196:195–202, 1995.

[14] L. E. Bilston, M. A. Stoodley, and D. F. Fletcher. The influence of the relative timing of arterial and subarachnoid space pulse waves on spinal perivascular cerebrospinal fluid flow as a possible factor in syrinx development. *Journal of neurosurgery*, 112(4):808–13, 2010. ISSN 1933-0693. doi: 10.3171/2009.5.JNS08945.

[15] I. G. Bloomfield, I. H. Johnston, and L. E. Bilston. Effects of proteins, blood cells and glucose on the viscosity of cerebrospinal fluid. *Pediatr Nerosurg*, 28:246–251, 1998.

[16] A. C. Bunck, J.-R. Kröger, A. Jüttner, A. Brentrup, B. Fiedler, F. Schaarschmidt, G. R. Crelier, W. Schwindt, W. Heindel, T. Niederstadt, and D. Maintz. Magnetic resonance 4d flow characteristics of cerebrospinal fluid at the craniocervical junction and the cervical spinal canal. *European radiology*, 21(8):1788–1796, 2011.

[17] A. C. Bunck, J. R. Kroeger, A. Juettner, A. Brentrup, B. Fiedler, G. R. Crelier, B. Martin, W. Heindel, D. Maintz, W. Schwindt, and T. Niederstadt. Magnetic resonance 4D flow analysis of cerebrospinal fluid dynamics in Chiari I malformation with and without syringomyelia. *European radiology*, 22(9):1860–70, 2012. ISSN 1432-1084. doi: 10.1007/s00330-012-2457-7.

[18] P. W. Carpenter, K. Berkouk, and A. D. Lucey. Pressure wave propagation in fluid-filled co-axial elastic tubes part 2: Mechanisms for the pathogenesis of syringomyelia. *Journal of Biomechanical Engineering*, 125(6):857, 2003. ISSN 01480731. doi: 10.1115/1.1634281.

[19] S. Cirovic. A coaxial tube model of the cerebrospinal fluid pulse propagation in the spinal column. *Journal of Biomechanical Engineering*, 131(2), 2009. ISSN 0148-0731. doi: 10.1115/1.3005159.

[20] J. Cousins and V. Haughton. Motion of the cerebellar tonsils in the foramen magnum during the cardiac cycle. *American Journal of Neuroradiology*, 30 (8):1587–1588, 2009.

[21] M. T. Dolar, V. M. Haughton, B. J. Iskandar, and M. Quigley. Effect of craniocervical decompression on peak csf velocities in symptomatic patients with Chiari I malformation. *American journal of neuroradiology*, 25(1): 142–145, 2004.

[22] N. S. J. Elliott. *Mathematical modelling and analysis of cerebrospinal mechanics: an investigation into the parthogenesis of syringomyelia*. PhD thesis, University of Warwick, 2009.

[23] N. S. J. Elliott. Syrinx fluid transport: modeling pressure-wave-induced flux across the spinal pial membrane. *Journal of Biomechanical Engineering*, 134(3), 2012. ISSN 1528-8951. doi: 10.1115/1.4005849.

[24] N. S. J. Elliott, D. A. Lockerby, and A. R. Brodbelt. A lumped-parameter model of the cerebrospinal system for investigating arterial-driven flow in posttraumatic syringomyelia. *Medical engineering & physics*, 33(7):874–82, 2011. ISSN 1873-4030. doi: 10.1016/j.medengphy.2010.07.009.

[25] N. S. J. Elliott, C. D. Bertram, B. A. Martin, and A. R. Brodbelt. Syringomyelia: A review of the biomechanics. *Journal of Fluids and Structures*, 40(0):1 – 24, 2013. ISSN 0889-9746. doi: http://dx.doi.org/10.1016/j.jfluidstructs.2013.01.010.

[26] D. Enzmann and N. J. Pelc. Normal flow patterns of intracranial and spinal cerebrospinal fluid defined with phase-contrast cine MR imaging. *Radiology*, 178:467–474, 1991.

[27] C. Figley and P. Stroman. Investigation of human cervical and upper thoracic spinal cord motion: implications for imaging spinal cord structure and function. *Magnetic Resonance in Medicine*, 58(1):185–189, 2007.

[28] N. J. Fischbein, W. P. Dillon, C. Cobbs, and P. R. Weinstein. The "presyrinx" state: A reversible myelopathic condition that may precede syringomyelia. *American Journal of Neuroradiology*, 20:7–20, 1999.

[29] W. J. Gardner. Hydrodynamic mechanism of syringomyelia: its relationship to myelocele. *Journal of Neurology, Neurosurgery and Psychiatry*, 28: 247–259, 1965.

[30] S. Goh, C. L. Bottrell, A. H. Aiken, W. P. Dillon, and Y. W. Wu. Presyrinx in children with Chiari malformations. *Neurology*, 71:351–376, 2008.

[31] D. Greitz. Unravelling the riddle of syringomyelia. *Neurosurgical Review*, 29:164–251, 2006.

[32] D. Greitz, K. Ericson, and O. Flodmark. Pathogenesis and mechanics of spinal cord cysts. *International Journal of Neuroradiology*, 5(2):61–78, 1999.

[33] D. Greiz, J. Hannerz, T. Rahn, H. Bolander, and A. Ericsson. MR imaging of cerebrospinal fluid dynamics in health and disease. *Acta Radiologica*, 35: 204–211, 1994.

[34] S. Gupta, M. Soellinger, P. Boesiger, D. Poulikakos, and V. Kortcuoglu. Three-dimensional computational modeling of subject-specific cerebrospinal fluid flow in the subarachnoid space. *Journal of Biomedical Engineering*, 131, 2009.

[35] P. Hall, M. Turner, S. Aichinger, P. Bendick, and R. Campbell. Experimental syringomyelia: the relationship between intraventricular and intrasyrinx pressure. *Journal of Neurosurgery*, 52(6):812–817, 1980.

[36] P. J. Harris and C. Hardwidge. Integral methods in science and engineering, volume 2. 2:193–201, 2010. doi: 10.1007/978-0-8176-4897-8.

[37] R. H. Hashemi, W. G. Bradley, and C. J. Lisanti. *MRI: the basics*. Lippincott Williams & Wilkins, 2012.

[38] S. M. Hassanizadeh and W. G. Gray. General conservation equations for multi-phase systems: 3. constitutive theory of porous media flow. *Advances in Water Resources*, 3:25–40, 1980.

[39] J. D. Heiss, N. Patronas, H. L. DeVroom, T. Shawker, R. Ennis, W. Kammerer, A. Eidsath, T. Talbot, J. Morris, E. Eskioglu, and E. H. Oldfield. Elucidating the pathophysiology of syringomyelia. *Journal of Neurosurgery*, 91:553–562, 1999.

[40] J. D. Heiss, G. Suffredini, K. D. Bakhtian, M. Sarntinoranont, and E. H. Oldfield. Normalization of hindbrain morphology after decompression of Chiari malformation type I: Clinical article. *Journal of neurosurgery*, 117 (5):942, 2012.

[41] S. J. Hemley, L. E. Bilston, S. Cheng, J. N. Chan, and M. A. Stoodley. Aquaporin-4 expression in post-traumatic syringomyelia. *Journal of neurotrauma*, 30(16):1457–1467, 2013.

[42] M. C. Henry-Feugeas, I. Idy-Peretti, O. Baledent, A. Poncelet-Didon, G. Zannoli, J. Bittoun, and E. Schouman-Claeys. Origin of subarachnoid cerebrospinal fluid pulsations: a phase-contrast MR analysis. *Magnetic resonance imaging*, 18(4):387–95, 2000. ISSN 0730-725X. URL `http://www.ncbi.nlm.nih.gov/pubmed/10788715`.

[43] S. Hentschel, K. A. Mardal, A. E. Løvgren, S. O. Linge, and V. Haughton. Characterization of cyclic CSF flow in the foramen magnum and upper cervical spinal canal with MR flow imaging and computational fluid dynamics. *American Journal of Neuroradiology*, 31:997–1002, 2010.

[44] E. Hofmann, M. Warmuth-Metz, M. Bendszus, and L. Solymosi. Phase-contrast MR imaging of the cervical csf and spinal cord: Volumetric motion analysis in patients with Chiari I malformation. *AJNR*, 21:151–158, 2000.

[45] B. J. Iskandar, M. Quigley, and V. Haughton. Foramen magnum cerebrospinal fluid flow characteristics in children with Chiari I malformation before and after decompression. *Journal of Neurosurgery*, 60:707–711, 2004.

[46] C. Johansen, J. Duncan, P. Klinge, T. Brinker, E. Stopa, and G. Silverberg. Multiplicity of cerebrospinal fluid functions: New challenges in health and disease. *Cerebrospinal Fluid Research*, 5(10), 2008.

[47] J. Klekamp. The pathophysiology of syringomyelia -historical overview and current concepts. *Acta Neurochirurgica*, 144:649–664, 2002.

[48] R. Labuda. *Conquer Chiari: A patient's Guide to the Chiari Malformation*. C&S Patient Education Foundation, 2008.

[49] D. N. Levine. The pathogenesis of syringomyelia associated with lesions at the foramen magnum: a critical review of existing theories and proposal of a new hypothesis. *Journal of neurological sciences*, 220:3–21, 2004.

[50] S. O. Linge, V. Haughton, A. E. Løvgren, K. A. Mardal, and H. P. Langtangen. CSF flow dynamics at the craniovertebral junction studied with an idealized model of the subarachnoid space and computational flow analysis. *American Journal of Neuroradiology*, 31:185–192, 2010.

[51] S. O. Linge, V. Haughton, A. E. Løvgren, K. A. Mardal, A. Helgeland, and H. P. Langtangen. Effect of tonsillar herniation on cyclic CSF flow studied with computational flow analysis. *AJNR. American journal of neuroradiology*, 32(8):1474–81, Sept. 2011. ISSN 1936-959X. doi: 10.3174/ajnr.A2496.

[52] S. O. Linge, K.-A. Mardal, V. Haughton, and A. Helgeland. Simulating csf flow dynamics in the normal and the Chiari I subarachnoid space during rest and exertion. *American Journal of Neuroradiology*, 34(1):41–45, 2013.

[53] P. Lockey, G. Poots, and B. Williams. Theoretical aspects of the attenuation of pressure pulses within cerebrospinal-fluid pathways. *Medical & Biological Engineering*, 13(6):861–9, Nov. 1975. ISSN 0025-696X.

[54] A. Logg, K. A. Mardal, and G. Wells, editors. *Automated Solution of Differential Equations by the Finite Element Method*, volume 84 of *Lecture Notes in Computational Science and Engineering*. Springer, 2012. ISBN 978-3-642-23098-1. doi: 10.1007/978-3-642-23099-8.

[55] F. Loth, M. A. Yardimci, and N. Alperin. Hydrodynamic modeling of cerebrospinal fluid motion within the spinal cavity. *ASME J. Biomech. Engrg.*, 123:71–73, 2001. doi: 10.1115/1.2801670.

[56] M. Marin-Padilla and T. M. Marin-Padilla. Morphogenesis of experimentally induced arnold-Chiari malformation. *Journal of the neurological sciences*, 50(1):29–55, 1981.

[57] B. A. Martin, W. Kalata, F. Loth, T. J. Royston, and J. N. Oshinski. Syringomyelia hydrodynamics: An in vitro study based on in vivo measurements. *Journal of Biomechanical Engineering*, 127:1110–1120, 2005.

[58] B. A. Martin, R. Labuda, T. J. Royston, J. N. Oshinski, B. Iskandar, and F. Loth. Spinal subarachnoid space pressure measurements in an in vitro spinal stenosis model: implications on syringomyelia theories. *Journal of Biomechanical Engineering*, 132(11):1–11, 2010. ISSN 1528-8951. doi: 10.1115/1.4000089.

[59] B. A. Martin, P. Reymond, J. Novy, O. Balédent, and N. Stergiopulos. A coupled hydrodynamic model of the cardiovascular and cerebrospinal fluid system. *American Journal of Physiology-Heart and Circulatory Physiology*, 302(7):H1492–H1509, 2012.

[60] B. A. Martin, W. Kalata, N. Shaffer, P. Fischer, M. Luciano, and F. Loth. Hydrodynamic and longitudinal impedance analysis of cerebrospinal fluid dynamics at the craniovertebral junction in type I Chiari malformation. *PloS one*, 8(10):e75335, 2013.

[61] J. Martin. *Neuroanatomy: Text and Atlas*. McGraw-Hill Companies, Inc., ISBN 0-07-138183, 3rd edition edition, 2003.

[62] D. J. Mikulis, M. L. Wood, O. Zerdoner, and B. P. Poncelet. Oscillatory motion of the normal cervical spinal cord. *Radiology*, 192(1):117–121, 1994.

[63] T. H. Milhorat, A. L. Capocelli, R. M. Kotzen, P. Bolognese, I. M. Heger, and J. E. Cottrell. Intramedullary pressure in syringomyelia: clinical and pathophysiological correlates of syrinx distension. *Neurosurgery*, 41(5): 1102–1110, 1997.

[64] C. Nicholson. Diffusion and related transport mechanisms in brain tissue. *Reports on Progress in Physics*, 64(7):815–884, July 2001. ISSN 0034-4885. doi: 10.1088/0034-4885/64/7/202.

[65] D. Norris. Diffusion mri. Technical report, Radboud University Nijmegen,, 2008.

[66] E. H. Oldfield, K. Muraszko, T. H. Shawker, and N. J. Patronas. Pathophysiology of syringomyelia associated with Chiari I malformation of the cerebellar tonsils. *Journal of Neurosurgery*, 80:3–15, 1994.

[67] G. Pinna, F. Alessandrini, A. Alfieri, M. Rossi, and A. Bricolo. Cerebrospinal fluid flow dynamics study in Chiari I malformation: implications for syrinx formation. *Neurosurgical Focus*, 8, 2000.

[68] M. F. Quigley, B. J. Iskandar, M. A. Quigley, M. N. Nicosia, and V. Haughton. Cerebrospinal fluid flow in foramen magnum: Temporal and spatial patterns at MR imaging in volunteers and in patients with Chiari I malformation. *Radiology*, 232:229–232, 2004.

[69] A. Roldan, O. Wieben, V. Haughton, T. Osswald, and N. Chesler. Characterization of csf hydrodynamics in the presence and absence of tonsillar ectopia by means of computational flow analysis. *American Journal of Neuroradiology*, 30:941–946, 2009.

[70] G. Rutkowska, V. Haughton, S. Linge, and K. A. Mardal. Patient-specific 3D simulation of cyclic CSF flow at the craniocervical region. *AJNR. American Journal of Neuroradiology*, 33(9):1756–62, 2012. ISSN 1936-959X. doi: 10.3174/ajnr.A3047.

[71] M. Schanz and S. Diebels. A comparative study of Biots theory and the linear theory of porous media for wave propagation problems. *Acta Mechanica*, 161:213–235, 2003. doi: 10.1007/s00707-002-0999-5.

[72] N. Shaffer, B. Martin, and F. Loth. Cerebrospinal fluid hydrodynamics in type I Chiari malformation. *Neurological research*, 33(3):247–60, 2011. ISSN 1743-1328. doi: 10.1179/016164111X12962202723805.

[73] N. Shaffer, B. A. Martin, B. Rocque, C. Madura, O. Wieben, B. Iskandar, S. Dombrowski, M. Luciano, J. N. Oshinski, and F. Loth. Cerebrospinal fluid flow impedance is elevated in type I Chiari malformation. *Journal of Biomechanical Engineering*, Accepted Manuscript, 2013. doi: doi:10.1115/1.4026316.

[74] S. Shah, V. Haughton, and A. M. del Río. CSF flow through the upper cervical spinal canal in Chiari I malformation. *American Journal of Neuroradiology*, 32(6):1149–1153, 2011.

[75] J. C. Simo and F. Armero. Unconditional stability and long-term behavior of transient algorithms for the incompressible navier-stokes and euler equations. *Computer Methods in Applied Mechanics and Engineering*, 111: 111–154, 1994.

[76] A. Sivaramakrishnan, N. Alperin, S. Surapaneni, and T. Lichtor. Evaluating the effect of decompression surgery on cerebrospinal fluid flow and intracranial compliance in patients with chiari malformation with magnetic resonance imaging flow studies. *Neurosurgery*, 55(6):1344–1351, 2004.

[77] M. A. Stoodley, N. R. Jones, L. Yang, and C. J. Brown. Mechanisms underlying the formation and enlargement of noncommunicating syringomyelia: experimental studies. *Neurosurg Focus*, 8(3), 2000.

[78] K. H. Støverud, H. P. Langtangen, V. Haughton, and K. A. Mardal. CSF pressure and velocity in obstructions of the subarachnoid spaces. *NRJ Digital*, 3(5):163–171, 2013.

[79] B. Williams. The distending force in the production of "communicating syringomyelia". *The Lancet*, pages 189–193, 1969.

[80] B. Williams. Cerebrospinal fluid pressure changes in response to coughing. *Brain*, 99:331–346, 1976.

[81] B. Williams. On the pathogenesis of syringomyelia: a review. *Journal of the Royal Society of Medicine*, 73:798–806, 1980.

[82] B. Williams. Simultaneous cerebral and spinal fluid pressure recordings. 2. cerebrospinal dissociation with lesions at the foramen magnum. *Acta Neurochirurgica*, 59:123–142, 1981.

[83] T. I. Yiallourou, J. R. Kröger, N. Stergiopulos, D. Maintz, B. Martin, and A. C. Bunck. Comparison of 4d phase-contrast MRI flow measurements to computational fluid dynamics simulations of cerebrospinal fluid motion in the cervical spine. *PloS one*, 7(12):e52284, 2012. ISSN 1932-6203. doi: 10.1371/journal.pone.0052284.

[84] Y. Zhang, Y. P. Zhang, L. B. Shields, Y. Zheng, X.-M. Xu, S. R. Whittemore, and C. B. Shields. Cervical central canal occlusion induces noncommunicating syringomyelia. *Neurosurgery*, 71(1):126–137, 2012.

Paper I

Modeling Concentration Distribution and Deformation during Convection-Enhanced Drug Delivery into Brain Tissue

Modeling Concentration Distribution and Deformation during Convection-Enhanced Drug Delivery into Brain Tissue

Karen H. Støverud, Melanie Darcis, Rainer Helmig, and S. Majid Hassanizadeh

Abstract

Convection-Enhanced drug Delivery (CED) is a technique where a therapeutic agent is infused under positive pressure directly into the brain tissue. For predicting the final concentration distribution and optimizing infusion rate and catheter placement, numerical models can be of great help. However, despite advances in modeling this process, often the infused agent does not reach the targeted region prescribed in the modeling phase. In this study, patient-specific brain structure and parameters, obtained from Diffusion Tensor Imaging (DTI), are implemented in a numerical model which describes the flow and transport in an elastic deformable matrix. To our knowledge this is the first time that information from DTI is used in a numerical model which includes both transport of a therapeutic agent and tissue deformation. Fractional anisotropy (FA) is used to distinguish between grey and white matter and tortuosity to differentiate between inside and outside the brain tissue. One voxel in the DT-image is represented by one element of the numerical grid. The DT-images were in addition used to determine the orientation of the white matter fiber tracts and calibrate permeability and diffusion coefficients found in the literature. Values chosen for the porosity and Lamé parameters are also based on those found in the literature. Given realistic literature values, the calibration of the permeability and diffusion tensors are shown to be successful. Our result show that preferential flow occur in direction of the white matter fiber tracts. The current model assumes linear deformation, corresponding to small porosity changes. But, because large porosity changes occur that may adversely affect drug transport, non-linear deformations should be included in the future.

1 Introduction

1.1 Motivation

Parkinson, Alzheimer, epilepsy and malignant brain tumors are all diseases affecting the Central Nervous System (CNS). In most cases, these diseases have severe consequences for the patients and the need for effective treatment is urgent. Although there often exist agents capable of curing these diseases, most therapeutic agents have proven inefficient when given orally or intravascularly. This is mainly because of two different effects. First, when one injects a therapeutic agent intravascularly it gets diluted. Thus, one needs a high dose to get the required concentration in the targeted region. But, the dose is limited by the drug concentration that the body as a whole can stand without severe consequences. Second, the blood-brain barrier (BBB) prevents many macromolecules from entering the interstitial space, which means that the drugs never reach the targeted region [20].

Thus, after finding an effective therapeutic agent, the challenge is to get the agent in the right concentration to the targeted region. To overcome the problems associated with the BBB and systemic toxicity, therapeutic agents can be introduced directly into the brain tissue. This can be done by continuously infusing the agent into the brain tissue via catheters, such that a pressure gradient arises. This technique is called Convection-Enhanced drug Delivery (CED) since the spreading is dependent on the infusion pressure and not diffusion only [36]. The pressure gradient induces flow and results in a higher concentration of the drug farther away than in the case of only diffusion-driven delivery [36, 43]

CED is still on an experimental level and many questions are left open. In particular, it is difficult to predict spatial distribution and local concentration variations [20, 43]. One reason is that the distribution of the agent is heavily dependent on factors such as heterogeneities in the brain tissue and local differences in interstitial pressure due to edema.

Several models describing CED have already been developed and can be divided into two main categories, based on whether the CNS is described as a rigid or an elastic porous medium.

Rigid Models: CED was first proposed in the beginning of the 1990's and one of the first mathematical models was developed by Morrison et al. [36]. This model describes the transport of macromolecules, assuming isotropic and homogeneous brain tissue for the case of high-flow and low-flow infusion. In the

latter case, they only considered diffusion. The model was based on a model by Baxter and Jain [6] applied for low-flow infusion. Both of these models were based on analytical solutions. Later, numerical solutions were obtained for more realistic cases. For example, Raghavan et al. [43], Linninger et al. [33], and Linninger et al. [32] all modeled CED into a human brain, while Kim et al. [28], Sarntinoranont et al. [44, 45] and Kim et al. [29] modeled CED into the spinal cord and corpus callosum of a rat. These models all used a rigid geometry based on MR-images and both anisotropy and heterogeneities were taken into account.

Elastic Models: The assumption of rigidity is actually not applicable to brain tissue. So, some models use the poro-elastic theory developed by Biot [8] to describe fluid transport in the interstitial space. Several models treating the brain as an elastic porous medium can be found in the literature. Basser [2], Netti et al. [38], Chen et al. [12] and Smith and Humphrey [48] all used a poro-elastic consolidation model and derived analytical solutions for the pressure field and velocity distribution during infusion into the center of a spherical tumor. Netti et al. [37], Kalyanasundaram et al. [26], Gillies et al. [19] and Chen and Sarntinoranont [11] used a similar poro-elastic consolidation model, but instead of deriving analytical solutions, the equations were solved numerically.

The mechanical properties of the brain and spinal cord are known to be non-linear and strain-rate dependent [13, 35]. To account for this, Smith and Garcia [49] and Smith and Garcia [47] recently developed a hyperelastic model. They considered two different cases: a constant pressure infusion [18] and a constant infusion rate [49]. Later, they included transport of a dissolved therapeutic agent in the model [47]. This hyperelastic model assumes a homogeneous and isotropic spherical geometry. Hyperelastic and viscoelastic models with realistic geometries have been developed to study e.g. the pathogenesis of hydrocephalus [16, 50], but to our knowledge none of these models describe mass transport or include heterogeneities and anisotropy of the brain tissue.

In order to find a compromise between describing the complex structure of the brain tissue and taking into account the relevant physical processes, this study shows a workflow from MRI measurements to a computational model with realistic parameters.

1.2 Outline

The aim of this study is to combine patient-specific parameters and brain structure with a poro-elastic model. Information about the structures of the tissue is

obtained from DTI and the effect of heterogeneities and anisotropy on the final concentration distribution. To our knowledge this is the first numerical model using information from DTI which includes both transport of a therapeutic agent and tissue deformation.

In Sec. 3 CED-induced flow and transport processes are described. Then, the mathematical model is presented. In Sec. 4, the determination of effective model parameters on the basis of a MRI-data set is described. Parameters that cannot be obtained from MRI are taken from the literature. Next simulations are done for the isotropic and homogeneous case and a comparison between rigid and poro-elastic models is conducted. Finally, the patient-specific parameters and brain structure are implemented and the effect of the location of the infusion is investigated. The paper is closed with a summary and a conclusion.

2 The Brain Tissue

Together with the spinal cord, the brain makes up the central nervous system (CNS). Although this is an extremely complicated system, the tissue mainly consists of two cell types; neurons and glial cells.

One can distinguish two different types of brain tissues, namely, white matter and grey matter. Grey matter has a high density of tightly packed neuron cell bodies, whereas white matter mainly consists of long axons that form fiber tracts. The outer part of the brain tissue consists of grey matter, while the inner parts mainly consist of white matter. Furthermore, the brain is covered by meningeal layers, which separates the brain tissue from the Cerebrospinal Fluid (CSF). CSF fills up both the empty space between the brain and the skull, and the cavities within the brain, called the ventricles.

The fluid-filled spaces inbetween the cells in the tissue are referred to as the interstitial space. The brain tissue is also penetrated by numerous blood vessels, called the vasculature. The vasculature may act as sink for the therapeutic agent. However, that is neglected in the present study, and only spreading of the therapeutic agent in the interstitial space is considered. The effect of vascular uptake have been studied by, e.g., [48] and [1].

The therapeutic agent can also undergo degradation and adsorption to the cells. These processes will obviously hinder the spreading of the drug. Morrison et al. [36] included linear metabolism and adsorption. These processes were also included, among others, by Linninger et al. [33], but are not considered in the current study, as we focus on the effects deformations, heterogeneities and anisotropy have on the concentration distribution.

3 Model

3.1 Conceptual Model

A porous medium can be defined as a solid or a structure with interconnected voids, through which fluids can flow. Although the human body is a highly sophisticated system, the porous medium assumptions can be used to describe relevant features and processes in the interstitial space accurately [39]. Thus, one may consider the brain as a heterogeneous porous medium where the neurons and glial cells make up the solid phase filled by the interstitial fluid [19]. The interstitial space is highly tortuous and the pore sizes are of nanoscale. Nevertheless, it makes up 20% of the total volume of the brain [39]. Blood vessels, ventricle walls, and meningeal layers all contribute to the brain's heterogeneous structure. Moreover, different properties of the grey and white matter lead to both heterogeneity and anisotropy. Grey matter has a low permeability, but is relatively homogeneous and isotropic. On the other hand, white matter has a higher permeability, but is anisotropic. This anisotropy arises from the fibers formed by the axons in the white matter. Heterogeneities and anisotropy are important factors for transport processes in the tissue, and should be taken into account.

3.2 Mathematical Model

In this study, a poro-elastic model with patient-specific parameters and brain structure obtained from MRI is developed. The model is based on a 1D model developed by Gillies et al. [19] and is here extended to 3D. Only the interstitial space and CED-induced transport processes are considered. For the mathematical model, the following assumptions were made:

- The therapeutic agent is completely soluble in the interstitial fluid.
- The fluid phase and the solid matter are both regarded as incompressible.
- The solid matrix is assumed to behave as an isotropic linear elastic material (small deformations)
- Changes in density and viscosity of the fluid phase as a result of dissolution of the therapeutic agent are neglected.
- The temperature is assumed to be constant.

- Chemical reactions, absorption and adsorption of infused agents are neglected.
- Gravity force is neglected

Thus, an equation for isothermal single-phase flow within an elastic matrix is solved for the fluid phase. To develop the flow equations, the solid matrix is taken into account as a second phase. The primary variables are the pressure (p) and the displacement ($\mathbf{u}$), and, in the transport equation, the molar concentration of therapeutic agent (c).

3.2.1 Flow Equations

Both fluid and solid phases are materially incompressible. However, the solid matrix is assumed to be deformable; that is, the void space can change as a result of change in fluid pressure. Assuming the density of the solid and the liquid phase to be constant the mass balance can be transformed to a volume balance (see e.g. Helmig [23]):

Solid phase:

$$\frac{\partial(1-\phi)}{\partial t} + \nabla \cdot ((1-\phi) \cdot \mathbf{v}_s) = 0 \tag{3.1}$$

Fluid phase:

$$\frac{\partial \phi}{\partial t} + \nabla \cdot (\phi \mathbf{v}_l) \pm \Omega_F(\mathbf{x}, t) = 0 \tag{3.2}$$

Here $\mathbf{v}_s$ and $\mathbf{v}_l$ represent the velocities of the solid and fluid phases, respectively. ϕ is porosity and $\Omega_F(\mathbf{x}, t)$ denotes source/sink terms of the fluid phase. Adding equation 3.1 and 3.2 yields:

$$\nabla \cdot (\phi \mathbf{v}_l + (1-\phi)\mathbf{v}_s) \pm \Omega_F(\mathbf{x}, t) = 0 \tag{3.3}$$

In the case of infinitesimal deformation, the velocity of the solid phase ($\mathbf{v}_s$) can be represented by the partial time derivative of the displacement vector ($\mathbf{u}$):

$$\mathbf{v}_s = \frac{D\mathbf{u}}{Dt} = \frac{\partial \mathbf{u}}{\partial t} \tag{3.4}$$

where $\frac{D}{Dt}$ denotes the material time derivative with respect to the solid phase velocity, which is approximated by the partial time derivative.

To describe the fluid flow in porous media on the continuum scale, generally the Darcy equation is applied. The Darcy equation represents a simplified momentum balance of the fluid phase [22]. It is valid in the case of creeping flow (Reynolds number < 1) which can be assumed for brain tissue because of the small pores and flow velocities. Moreover, Reynolds number < 1 implies that inertial forces can be assumed negligible [23]. For the poro-elastic case, there is an additional transport component since the displacement of the solid matrix contributes to movement of fluid within its pores. Thus, the transport velocity is:

$$\mathbf{v}_l = -\frac{\mathbf{K}}{\phi\mu_w}\left(\nabla p - \rho_l \mathbf{g}\right) + \frac{\partial \mathbf{u}}{\partial t} \tag{3.5}$$

Here $\mathbf{K}$ represents the intrinsic permeability tensor, ρ_l is the fluid mass density, and μ_w is the viscosity of water which is assumed equal to the viscosity of interstitial fluid (ISF). Since the fluid source is applied as a point source, the pressure gradient is steep and more important than gravity. Thus, gravity is assumed to be negligible. Substituting equation (3.5) in equation (3.3) and rearranging yields the final form of the fluid-solid mixture volume balance:

$$\nabla \cdot \left(\frac{\partial \mathbf{u}}{\partial t} - \frac{\mathbf{K}}{\mu_w}\nabla p\right) = \Omega_F(\mathbf{x}, t) \tag{3.6}$$

To set up a balance of forces in a porous medium, both the fluid and the solid phase have to be considered. As already mentioned, inertial forces and gravity are neglected. Thus, the only remaining forces are caused by the fluid pressure and by the stresses in the solid matrix.

$$\nabla\left(\sigma - p\mathbf{I}\right) = 0 \tag{3.7}$$

Further, the displacement vector ($\mathbf{u}$) can be related to the deformation or strain tensor field:

$$\mathbf{e} = \frac{1}{2}(\nabla \mathbf{u} + \nabla^T \mathbf{u}) \tag{3.8}$$

Assuming an isotropic, linear elastic medium, it can be shown that the following linear stress-strain relation holds [22] :

$$\sigma = 2\mu\mathbf{e} + \lambda(tr\mathbf{e})\mathbf{I} \tag{3.9}$$

where μ and λ represent Lamé parameters. Substituting (3.9) and (3.8) into (3.7) and rearranging yields:

$$\nabla \cdot \big(\mu(\nabla \mathbf{u} + \nabla^T \mathbf{u}) + \lambda(\nabla \cdot \mathbf{u})\mathbf{I}\big) - \nabla p = 0 \tag{3.10}$$

Note that $\mathbf{u}$ and p are time-dependent due to Eq. 3.6. The Lamé parameters are used to characterize the elasticity of a medium and are related to the Poisson ratio (ν) and Young's modulus (E) as follows:

$$\lambda = \frac{E\nu}{(1+\nu)(1-2\nu)}, \qquad \mu = \frac{E}{2(1+\nu)} \tag{3.11}$$

For small values of μ and λ, deformation may occur even at low infusion pressure. While high values imply that the medium can be regarded as rigid.

3.2.2 Transport equation

The transport equation can be derived from the mass balance of the infused therapeutic agent and results in the following equation:

$$\frac{\partial(c\phi)}{\partial t} + \nabla \cdot (\phi \mathbf{v}_l c - \mathbf{D}_{pm} \nabla c) = \Omega_T(\mathbf{x}, t) \tag{3.12}$$

where $c\,[mol/L^3]$ represents the concentration of the therapeutic agent and $\mathbf{D}_{pm}$ is the effective diffusion tensor of the porous medium which in general is smaller than the diffusion coefficient of the agent in free water. $\Omega_T(\mathbf{x}, t)\,[mol/sL^3]$ is a source/sink term for the therapeutic agent.

3.3 Effective Parameters

In an elastic medium, the structure of the solid phase is time dependent. This should be taken into account in the model by relating medium properties to deformation.

3.3.1 Porosity

Even though both fluid and solid phases are regarded as incompressible, their volume fractions can change due to local displacement. For small deformations the following relation between $\nabla \cdot \mathbf{u}$ and the porosity (ϕ) have been used [38]:

$$\phi = \frac{\phi_0 + \nabla \cdot \mathbf{u}}{1 + \nabla \cdot \mathbf{u}} \tag{3.13}$$

This equation is employed in most poro-elastic models that include porosity changes [11, 12, 19]. However, an expression for the effective porosity can also be derived from the volume balance of the solid phase (Eq. 3.1) employing the

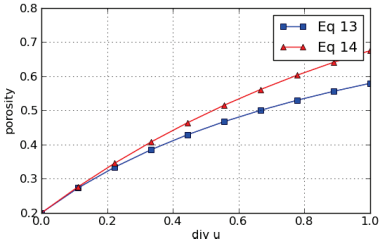

Figure 3.1: The porosity is plotted versus displacement for an initial porosity of 0.2. For small deformations it can be seen that the different formulas do not make a difference, while for increasing divergence Eq. 3.14 results in lower porosity changes than the equation found in the literature.

approximation given in Eq. 3.4 for small deformation and the initial conditions $\phi = \phi_0$ and $\nabla \cdot \mathbf{u} = 0$. The result is:

$$\phi = 1 - (1 - \phi_0)e^{-\nabla \cdot \mathbf{u}} \tag{3.14}$$

In Figure 3.1, porosity is plotted against the divergence of displacement for equations (3.13) and (3.14). As long as the divergence of displacement ($\nabla \cdot \mathbf{u}$) is small the two formulas yield similar results. Small $\nabla \cdot \mathbf{u}$ is a result of gentle pressure gradients or high values of the Lamé parameters. When the divergence is large, the difference between equation (3.13) and (3.14) increases. However, in the range were the linear elasticity theory holds, the two relations yield similar results and in the current study equation (3.14) has been used.

3.3.2 Permeability

Zhang et al. [53] showed that, during intra-tumoral infusion, an increase of the infusion pressure leads to significant changes in the permeability of the tissue. This is related to the deformation, which causes changes in size and connectivity between pores in the tissue. Tissue expansion may increase the conductivity and, thus, the permeability of the tissue in the vicinity of the injection point, whereas compression farther away closes the paths and may reduce permeability of the tissue [34]. Lai and Mow [31] proposed the following exponential relationship between the deformation and permeability:

$$\mathbf{K} = \mathbf{K}_0 e^{\beta \nabla \cdot \mathbf{u}} \tag{3.15}$$

Table 3.1: Governing equations and boundary conditions

Volume balance	$\nabla \cdot \left(\frac{\partial \mathbf{u}}{\partial t} - \frac{\mathbf{K}}{\mu_w} \cdot \nabla p \right) = \Omega_F(\mathbf{x}, t)$
Displacement	$\nabla \cdot \left(\mu(\nabla \mathbf{u} + \nabla^T \mathbf{u}) + \lambda(\nabla \cdot \mathbf{u})\mathbf{I} - p\mathbf{I} \right) = 0$
Transport equation	$\frac{\partial (c\phi)}{\partial t} + \nabla \cdot \left(\left[c \left(-\frac{\mathbf{K}}{\mu_w} \cdot \nabla p + \phi \frac{\partial \mathbf{u}}{\partial t} \right) - \mathbf{D}_{pm} \nabla c \right] \right) = \Omega_T(\mathbf{x}, t)$
Porosity	$\phi = 1 - (1 - \phi_0) e^{-\nabla \cdot \mathbf{u}}$
Permeability	$\mathbf{K} = \mathbf{K}_0 e^{\beta \nabla \cdot \mathbf{u}}$
Diffusion	$\mathbf{J} = -\mathbf{D}_{pm} \nabla c$
Boundary conditions	$\mathbf{u} = 0$ cm on $\partial\Omega$
	p = 400 Pa on $\partial\Omega$
	c = 0 on $\partial\Omega$

Here $\mathbf{K}_0$ is the initial permeability tensor and β is a material constant. McGuire et al. [34] fitted this parameter to results obtained from an experiment performed on both rodent and human tumor models. A sensitivity analysis was carried out and β was found to vary between 0 and 5. Equation 3.15 was later employed in a poro-elastic model by Chen and Sarntinoranont [11].

3.3.3 Diffusion

The last part of the second term in equation 3.12 represents diffusive flux. Diffusive flux is molecular transport caused by concentration gradients and can be described by Fick's 1st law [39]:

$$\mathbf{J} = -\mathbf{D}_{pm} \nabla c \quad \text{where} \quad \mathbf{D}_{pm} = \phi \tau \mathbf{D}^* \tag{3.16}$$

$\mathbf{D}_{pm}$ is the effective diffusion tensor in a porous medium. $\mathbf{D}_{pm}$ is lower than the anisotropic aqueous diffusion tensor $\mathbf{D}^*$ obtained from diffusion tensor imaging, since the diffusion of therapeutic agent is limited to the porespace and since the connections between pores do not form straight channels. This is represented in Eq. 3.16 by the porosity (ϕ) and the tortuosity (τ). ϕ is time-dependent as given in Eq. 3.14, while τ is kept constant, a reasonable assumption for a convection dominated problem, since the diffusion is of less importance.The method of determination of the diffusion tensor ($\mathbf{D}^*$) and τ are explained in Sec. 4.2 and Sec.4.2.3, respectively.

3.4 Numerical Implementation

The full set of governing equations are presented in Table 3.1. The equations are discretized and then implemented in a fully coupled flow and transport model based on a first-order Euler time discretization in combination with a BOX-discretization in space [23]. The BOX-discretization is a vertex-centered finite volume scheme, which is constructed on a finite element mesh. It allows the application of unstructured grids by evaluating the gradients using finite element shape functions. The scheme is locally and, thus, globally mass conservative, since the BOX-discretization is based on finite volumes. The discretized equations were then implemented in the $DuMu^x$ framework [17].

4 Determination of Parameters

To apply the model described above to realistic cases, information about the properties of the tissue is needed. Since every human is unique, patient-specific parameters must be found *in vivo*. In this paper, information from Magnetic Resonance Imaging (MRI) of a patient is interpreted to determine effective model parameters. From Diffusion Tensor Imaging (DTI), we use the self-diffusion tensor of water in brain tissue ($\mathbf{D}_{s-d}$) to characterize the degree of heterogeneity and anisotropy. Furthermore, information from the DTI data are used to delineate geometrical boundaries. For an overview of diffusion-weighted MRI, we refer to Hagmann et al. [21].

4.1 Parameters from literature

In the future, all patient-specific parameters should be obtained non-invasively. Currently, literature values are needed for initial porosity (ϕ_0), the Lamé parameters (μ and λ), and for the calibration of K and D described below. Bender and Klose [7] proposed a method for determining porosity from MRI that showed promising results. For the elasticity parameters, more research is still needed, but we believe that elastography will be a useful tool in the future (see e.g. Klatt et al. [30] or Cheng et al. [14]). However, in the scope of this study, the parameters are based on average values found in the literature (see Smith and Humphrey [48] for a review). In general these values have been measured using animal models, and are not human brain data.

4.2 Diffusion Tensor Imaging (DTI)

In this study, Diffusion Tensor Images (DTI) are obtained from a patient at OVGU-Magdeburg University Hospital, Germany. Each 3D image represents one of the components of the self-diffusion tensor of water in the brain tissue ($\mathbf{D}_{s-d}$) and consists of $128 \cdot 128 \cdot 65$ voxels with a resolution of 2 mm. All calculations performed in the following are based on this data–set.

Basser et al. [5] showed how $\mathbf{D}_{s-d}$ in human tissues can be estimated from spin-echo experiments using multiple regressions. Later, Basser et al. [4] also verified how this technique can be used to determine the orientation of white matter fiber tracts; the eigenvector corresponding to the largest eigenvalue of $\mathbf{D}_{s-d}$ defines the tissue's fiber tracts axis ($z - axis$), while the two remaining perpendicular eigenvectors define the $x-$ and $y - axis$. Then, after preprocessing the raw data, $\mathbf{D}_{s-d}$ can be represented voxel wise as a positive definite symmetric tensor.

A general macroscale transport tensor, e.g. electrical conductivity or diffusion tensor, can be related to the microstructures of the medium through its statistical moments [10, 46]. Tuch et al. [51] demonstrated how this principle can be used to link $\mathbf{D}_{s-d}$ to the electrical conductivity of biological tissue. Further, they proposed that the same principle can be used to estimate the diffusion of macromolecules ($\mathbf{D}^*$) within the tissue and the permeability ($\mathbf{K}_0$) of the tissue.

The mathematical model used in this study assumes anisotropic permeability and diffusion tensors, whereas the elastic properties are assumed to be isotropic. Even though the fiber structure of the white matter suggests anisotropic elastic properties, this issue is still under debate [14]. Odgaard et al. [41] and Odgaard [40] showed that mechanical anisotropy directions are aligned with the directions of the fiber structure in cancellous bone. More recently, Cowin and Cardoso [15] developed a poro-elastic model that takes anisotropic elasticity into account, with application to cancellous bone. However, it is still an open question whether the elastic properties of brain tissue align with the fiber tracts [14]. Therefore, we have chosen to model the brain tissue as an isotropic elastic material.

Sarntinoranont et al. [45] calculated $\mathbf{K}$ and $\mathbf{D^*}$ tensors for the spinal cord of a rat and Linninger et al. [32] obtained the same parameters for a human brain. The main assumption behind this principle is, as Basser et al. [5] and Tuch et al. [51] proposed, that $\mathbf{D}_{s-d}$, $\mathbf{K}$ and $\mathbf{D^*}$ share the same set of eigenvectors. In the paper by Sarntinoranont et al. [45], the eigenvalues in the white matter regions are assumed to be equal in x- and y- direction, while a significantly higher value is assumed in the z-direction. This is a reasonable assumption for the spinal cord,

where the orientation of most of the fiber tracts is in the z-direction. In the brain tissue, the orientation of the fiber tracts is heavily dependent on the location. But the eigenvalues can be calibrated to the eigenvalues of the self-diffusion tensor following a three-step calibration procedure proposed by Linninger et al. [32]. Below we describe the calibration of the initial permeability field ($\mathbf{K}_0$); exactly the same principle is used to obtain $\mathbf{D^*}$.

4.2.1 Initial Permeability, $\mathbf{K}_0$

In the first step, the diffusion tensor ($\mathbf{D}_{s-d}$), obtained from DTI, is decomposed into eigenvectors (ξ) and eigenvalues (λ_{i_w}) for each voxel:

$$\mathbf{D}_{s-d} = \xi \cdot \mathbf{\Lambda} \cdot \xi^{\mathbf{T}} \quad \text{where} \quad \mathbf{\Lambda} = \begin{bmatrix} \lambda_{1_w} & 0 & 0 \\ 0 & \lambda_{2_w} & 0 \\ 0 & 0 & \lambda_{3_w} \end{bmatrix}. \tag{4.1}$$

In the second step, the mean of the eigenvalues ($\bar{\lambda}_w$) is found and then the eigenvalues are scaled by $\bar{\lambda}_w$. The result is multiplied by a typical value of the permeability (K) obtained from the literature, in order to obtain eigenvalues of the initial permeability field:

$$\bar{\lambda}_w = \frac{1}{3}\Sigma_{i=1}^{3}\lambda_{i_w} \quad \text{and} \quad \lambda_{i_K} = K\left(\frac{\lambda_{i_w}}{\bar{\lambda}_w}\right) \tag{4.2}$$

Finally, in step 3 the initial permeability tensor ($\mathbf{K}_0$) is calculated:

$$\mathbf{K}_0 = \xi \cdot \mathbf{\Lambda_K} \cdot \xi^{T} \quad \text{where} \quad \mathbf{\Lambda_K} = \begin{bmatrix} \lambda_{1_K} & 0 & 0 \\ 0 & \lambda_{2_K} & 0 \\ 0 & 0 & \lambda_{3_K} \end{bmatrix}. \tag{4.3}$$

As mentioned above, the initial permeability tensor is assumed to have the same eigenvectors as the diffusion tensor. In Figure 4.1, results of the calibration for $\mathbf{K}_0/K$ are presented to show the anisotropy of the brain tissue.

The method proposed by Linninger et al. [32] requires a reference value for the permeability (K). Based on pressure fields measured during CED in clinical trials [9, 42], an average permeability value of $K = 1.82 \cdot 10^{-15}\ m^2$ was calculated by Smith and Humphrey [48]. In this study $K = 1.82 \cdot 10^{-15}\ m^2$ is applied unless otherwise is stated. However, a wide range of permeability values can be found in the literature; see e.g. Basser [2], Kaczmarek et al. [25]. Moreover, the permeability in white matter is often assumed to be significantly higher than in grey matter (see Sec. 5).

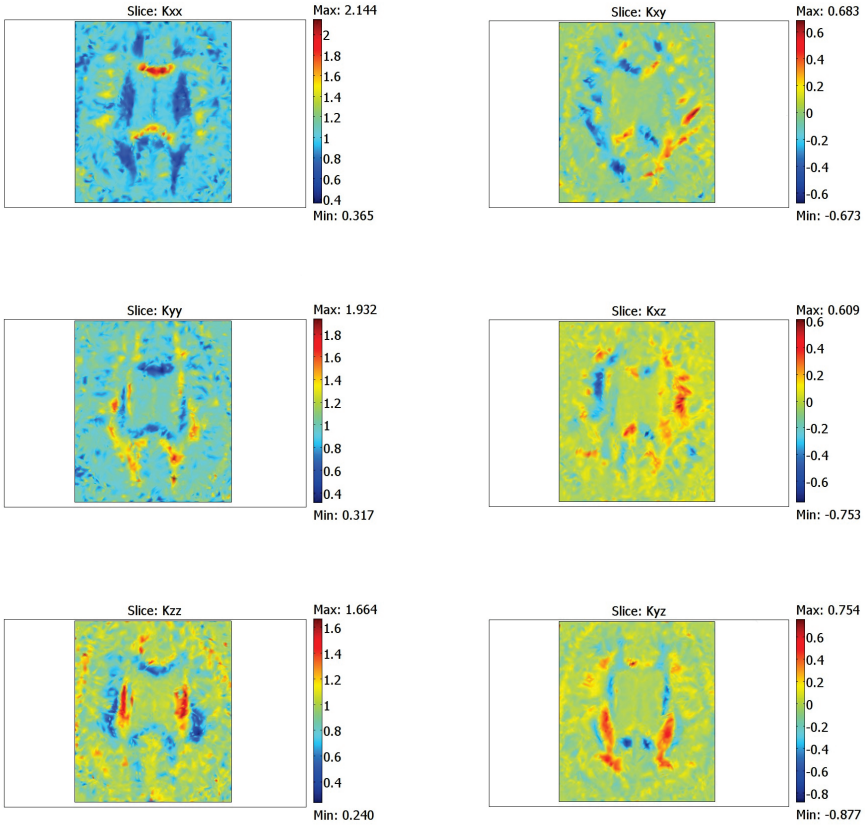

Figure 4.1: A cross-section of the six components of the DTI-dataset after performing the calibration proposed by Linninger et al. [32]. Note that the plots represents $\mathbf{K}_0/K$ and, thus, the anisotropic features of the tissue. The left column shows the components of the main diagonal of the normalized tensor, while the right represents the off-diagonals of the symmetric tensor. In the most anisotropic regions $K_{xx} \approx 7K_{yy}$

4.2.2 Diffusion Tensor, $\mathbf{D}^*$

The diffusion tensor ($\mathbf{D}^*$) is obtained in the same manner as the effectiv permeability ($\mathbf{K}_0$). The only difference is that now the calibration of the eigenvalues is given as:

$$\lambda_{i_D} = D\left(\frac{\lambda_{i_w}}{\overline{\lambda}_w}\right) \tag{4.4}$$

Note that D is the free diffusion coefficient of the contrast agent Gd-DTPA in water, which is equal to $D = 3.8 \cdot 10^{-10} m^2/s$ [27]. Finally, $\mathbf{D}^*$ becomes:

$$\mathbf{D}^* = \xi \cdot \mathbf{\Lambda_D} \cdot \xi^T \quad \text{where} \quad \mathbf{\Lambda_D} = \begin{bmatrix} \lambda_{1_D} & 0 & 0 \\ 0 & \lambda_{2_D} & 0 \\ 0 & 0 & \lambda_{3_D} \end{bmatrix}. \tag{4.5}$$

4.2.3 Tortuosity (τ)

The calibration of $\mathbf{D}^*$ takes the anisotropy into account, but not the tortuosity (τ). τ is calculated from DTI-data defining tortuosity as the square root of effective diffusion measured in DTI [52] divided by the free self-diffusion coefficient of water (D_w). D_w is here taken to be $3.22 \cdot 10^{-9}\ m^2/s$ which holds for water at 40 ℃ [24]. The tortuosity is kept constant and its value is based on the trace of $\mathbf{D}_{s-d}$ in the DTI-data;

$$\tau = \sqrt{\frac{\frac{1}{3}\left(D_{xx} + D_{yy} + D_{zz}\right)}{D_w}} \tag{4.6}$$

The diffusion of water in the tissue cannot exclusively be assigned to the extracellular space. Since water can diffuse through the cells, the diffusion tensor obtained from DTI overestimates the tortuosity of the medium [52].

4.3 Geometry

From MRI, the anatomy of the brain can be reconstructed. Obviously, this is important since different brain structures have different transport properties. This reconstruction should delineate white matter and grey matter regions, ventricles and meningeal layers. All these structures play an important role when modeling the flow and transport processes in the brain. Reconstruction can be done applying algorithms such as noise filtering, contrast enhancement, and edge detection to MR-images. From this, a domain corresponding to the shape

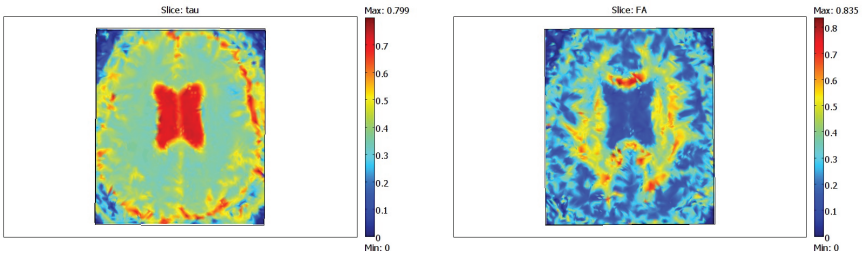

Figure 4.2: (left) Cross-section of the tortuosity calculated using Eq 4.6. (right) Fractional Anisotropy (FA) calculated using Eq 4.7

of the brain is created. These are rather time consuming methods. Therefore, in this study a voxel-based approach was used. This was also done in a study by Kim et al. [28] and Kim et al. [29]. In this approach, a dimensionless index, called Fractional Anisotropy (FA), is used to distinguish between white and grey matter. FA is calculated based on the eigenvalues obtained from DT-images:

$$FA = \sqrt{\frac{3}{2} \cdot \frac{\left(\lambda_{1_w} - \bar{\lambda}\right)^2 + \left(\lambda_{2_w} - \bar{\lambda}\right)^2 + \left(\lambda_{3_w} - \bar{\lambda}\right)^2}{\lambda_{1_w}^2 + \lambda_{2_w}^2 + \lambda_{3_w}^2}} \tag{4.7}$$

where $\bar{\lambda}$ is the mean of the eigenvalues defined in Eq. 4.2. This index was proposed by Basser and Pierpaoli [3] and is a measure of the fraction of $\mathbf{D}_{s-d}$ which can be assigned to anisotropic diffusion. For an isotropic medium, FA is 0, while for an axisymmetric anisotropic medium FA = 1. Since brain tissue is neither axisymmetric nor isotropic, the FA values lie somewhere between 0 and 1. In this study, voxels with FA > 0.4 are defined as white matter (Table 4.1). This is done based on the FA values shown in Figure 4.2. Distinguishing between grey matter and white matter is important since the infused agents spread over larger volumes in white than in grey matter. For low-resolution MR-images, the probability that the signal from one voxel only represents one tissue type is pretty low. This leads to another uncertainty in this parameter. But, in the future, higher resolution images will solve this problem.

To delineate ventricles, meningeal layers, and bones from the parenchyma, the tortuosity field (see Sect. 4.2.2) is used. The threshold values applied are

Table 4.1: Based on threshold values, it is distinguished between different regions and tissue types in the brain.

	FA	τ
Grey matter	0-0.4	0.24-0.54
White matter	>0.4	0.24-0.54
Ventricle/meninges	-	<0.24 or >0.54

given in Table 4.1. This approach works well for the ventricles, but again the resolution is too low to successfully delineate the meningeal layers.

5 Results and Discussion

5.1 Simulations for the Homogenous and Isotropic Case

To test the capability of the model, 3D simulations were performed on a homogenous and isotropic domain. Dirichlet boundary conditions were imposed, i.e., displacement ($\mathbf{u}$) and concentration (c) were set to zero and pressure (p) to 400 Pa at the outer boundaries. The modeled domain was $4 \cdot 4 \cdot 4$ cm^3 and the gridspacing was 2 mm using a regular cubic grid. The simulations were performed for 2 hours with an initial timestep size of 5 seconds. A source term representing a constant infusion rate of 0.3 ml/hr (5 μl/min) was assigned to one node in the center of the domain. This fills up one finite volume box, which can be interpreted as a catheter with a diameter equal to the grid spacing. Similar infusion rates were used in the models by Linninger et al. [33] (4 μl/min) and Smith and Garcia [47] (6 μl/min). The concentration of the therapeutic agent in the infused fluid was set to 10^{-7} mole of Gd-DTPA per mole water. The pressure was time dependent (see Eq. 3.6), but after approximately 1 hr it reached steady state. Due to mixing of the infused fluid and the ISF it took a few minutes before the concentration in the interstitial space equaled the concentration in the infused fluid.

The current model was compared to the linear elastic model by Chen and Sarntinoranont [11] and the hyperelastic model by Smith and Garcia [47], with the same parameter values as they used in their studies. The current model yields similar results for pressure and deformation as the model by Chen and Sarntinoranont [11], but due to different boundary conditions (assignment of source), the concentration distribution is different. Compared to the model by

Table 5.1: Literature values used in the simulations [11, 27, 34, 39, 48]

Parameter	**S**ymbol	**V**alue	**U**nit
Permeability	K_0	$1.82 \cdot 10^{-15}$	$[m^2]$
Viscosity of water	μ_w	$9.11 \cdot 10^{-4}$	[Pa s]
Molar density of water	ρ_{mol}	55500	$[mol/m^3]$
Diffusion coefficient Gd-DTPA	D	$3.8 \cdot 10^{-10}$	$[m^2/s]$
Porosity	ϕ_0	0.2	[-]
Tortuosity	τ	0.4	[-]
Young's Modulus	E	5000	[Pa]
Poisson ratio	ν	0.4	[-]
Material constant	β	2	[-]

Smith and Garcia [47] the concentration distribution in the interstitial space is similar, but the displacement and pressures are different, since they used a non-linear elastic model.

In the following, a grid convergence test is presented. Then, the initial permeability, Young's modulus and Poisson ratio are varied, this can give an indication of sensitivity in our results to the range of realistic parameter values (Sec.5.1.2). Finally, the poro-elastic model used in this study is compared to the rigid assumption case, to see whether including elasticity yields significantly different results (Sec.5.1.3).

5.1.1 Grid convergence

To check whether the mesh is sufficiently refined a grid convergence test was performed with three different gridspacings; 2 mm, $\frac{2}{3}$ mm and $\frac{2}{9}$mm. The parameters given in Table 5.1 were used and the source term was assigned to a volume of 8 mm^3 for all cases. The results can be seen in Figure 5.1. Since the source term was distributed over more nodes when the mesh was refined, a significantly lower peak pressure in the middle can be seen. However, the peak pressure values converged with increasing grid resolution, as can be seen in Fig. 5.1. With respect to the displacement, the maximum values are highest for the lowest resolution. For the two cases with the finer meshes, the displacement becomes more distributed and converges to the same result. Nevertheless, the concentration distribution, which was of major interest in this study, was similar

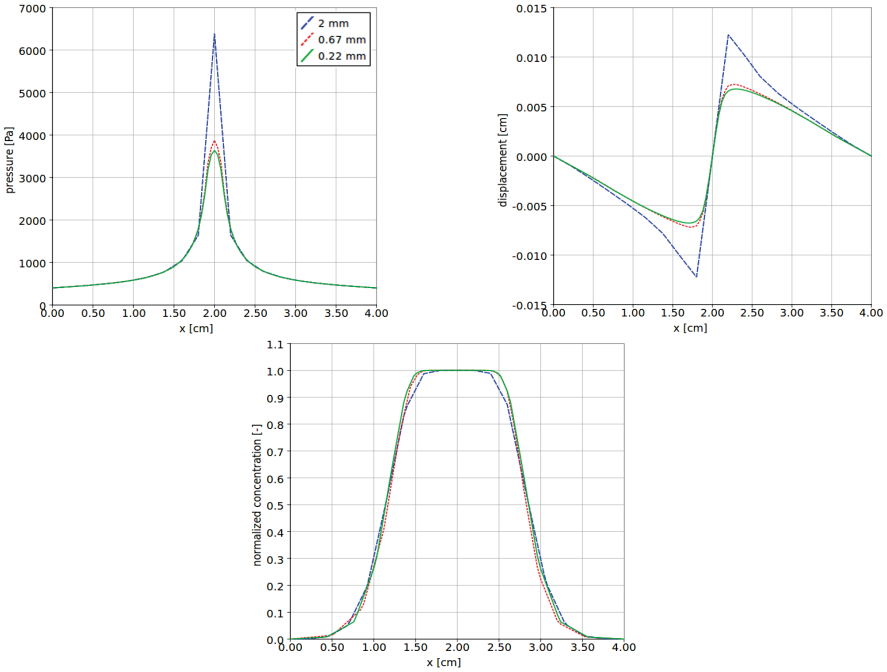

Figure 5.1: Results from the grid convergence simulations.

for all cases.In all of the following simulations the gridspacing was 2mm and one should have this in mind interpreting the results.

5.1.2 Choice of K-values and elastic properties

Even though permeability values for brain tissue can be found in the literature, there is still a large uncertainty in this parameter. In clinical trials, significantly less spreading of the infused agent has been observed in grey matter than in white matter [9, 42]. To take this into account, Kaczmarek et al. [25] assumed the permeability of white matter to be 100 times larger than that of grey matter. Based on this, both Linninger et al. [32] and Sarntinoranont et al. [44, 45] used $K_{wm} = 100K_{gm}$ in their studies.

We performed simulations for three different K-values, $K = 1.82 \cdot 10^{-15}m^2$, $1.3 \cdot 10^{-16}m^2$ and $1.3 \cdot 10^{-14}m^2$ and the effects on the pressure field, the porosity

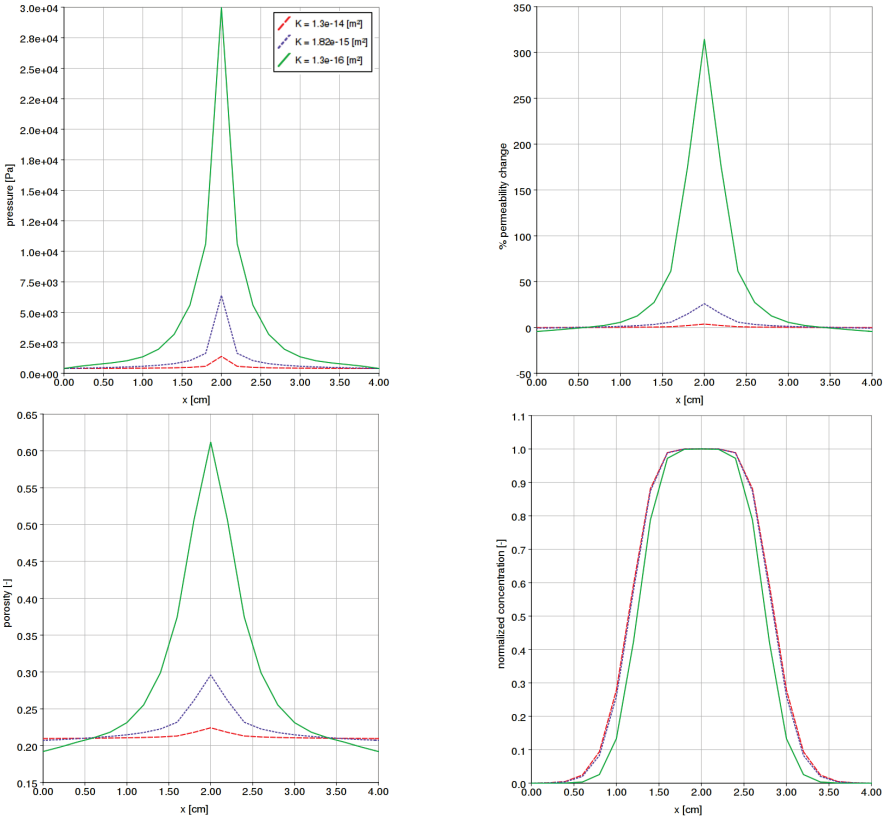

Figure 5.2: Results from simulations with different K-values.

field and the concentration distribution was investigated. Note that according to Eq. 3.6 the permeability was divided by the viscosity. The results can be seen in Figure 5.2 where the three different permeability values are compared. The time to steady state is significantly larger for low permeability values than for high values, since low permeability leads to steeper pressure gradient, higher deformation and a longer consolidation period. However, after 2 hours, steady state is reached even for the low permeability case.

As already mentioned, the value found by Smith and Humphrey [48] was used as the reference value for the permeability. This value is based on measured pressure increases, relative to the intracranial pressure, during CED into white matter of a cat brain [9] and into grey matter of a rat brain [42]. In the study by Bobo et al. [9], the observed pressure increase is approximately 2.4 kPa for an infusion rate of 0.07 ml/h. Employing permeability values of $1.82 \cdot 10^{-15} m^2$, yields maximum pressures that agree with this; an infusion rate of 0.1 ml/hr resulted in a pressure increase of 2.6 kPa (results not shown). The two other permeability values employed, $1.3 \cdot 10^{-16} m^2$ and $1.3 \cdot 10^{-14} m^2$, are also within the range of the values employed in other numerical models (see Sec.4.2). However, the lowest permeability value lead to a pressure increase of about 30 kPa in the infusion center. On the other hand, the highest permeability causes a pressure increase of only about 1 kPa. Therefore, with the current Young's moduli values the permeability value calculated by Smith and Humphrey [48] seems most realistic. However, since the brain tissue is heterogeneous, we can expect similar pressure increases in regions with low permeability if the low permeability zone is small. Similarly, high pressure increases can occur in high permeability regions if the surroundings have a significantly lower permeability. Thus, a homogeneous and isotropic model domain is inadequate to describe the pressure fields observed in clinical trials.

In this study, linear elasticity is assumed and elastic parameters based on Smith and Humphrey [48] and Chen and Sarntinoranont [11] are used. However, in recent nonlinear elastic models [16, 47, 49] significantly lower Young's moduli (E) based on a study by Miller and Chinzei [35] have been used. To see how this affects the results, simulations were conducted with E = 421 [35] and $\nu = 0.35$. In Figure 5.3 the results from using both set of parameters are compared. The pressure values are significantly lower using the values from Miller and Chinzei [35] than the ones from Smith and Humphrey [48]. This is because the displacement are larger, which according to Eq. 3.14 and 3.15 leads to increased porosity and permeability changes, respectively. Note that E = 421 Pa results in such large porosity changes that the choice of relation between displacement and porosity becomes more important (see Eq. 3.14). Finally, the drug spreads

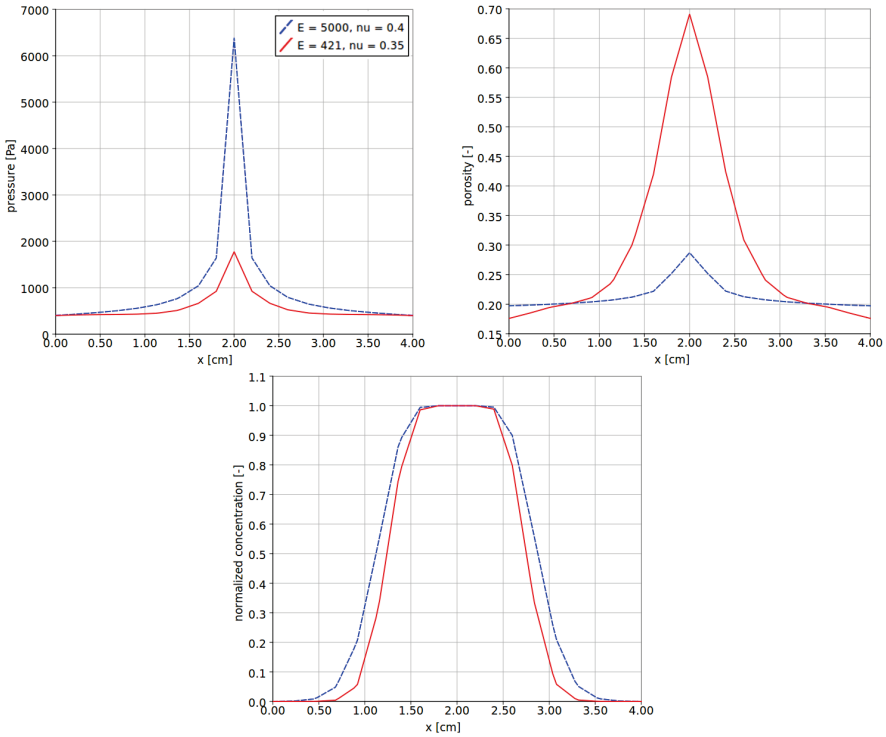

Figure 5.3: Comparison of the Young's modulus (E) and Poisson ratio (ν) used in this study and the values from Miller and Chinzei [35]

to a smaller extent due to larger storage as a result of the increased porosity. Additionally, the porosity and permeability decreases farther away from the infusion site and hinders flow.

5.1.3 Rigid vs Elastic model

As discussed in Sec. 1.1, often the assumption has been employed that in models describing flow and transport during CED, brain tissue deformation is negligible. To test this assumption, the from the elastic model were compared to the result from a rigid model using the same parameters, grid spacing, and domain size,

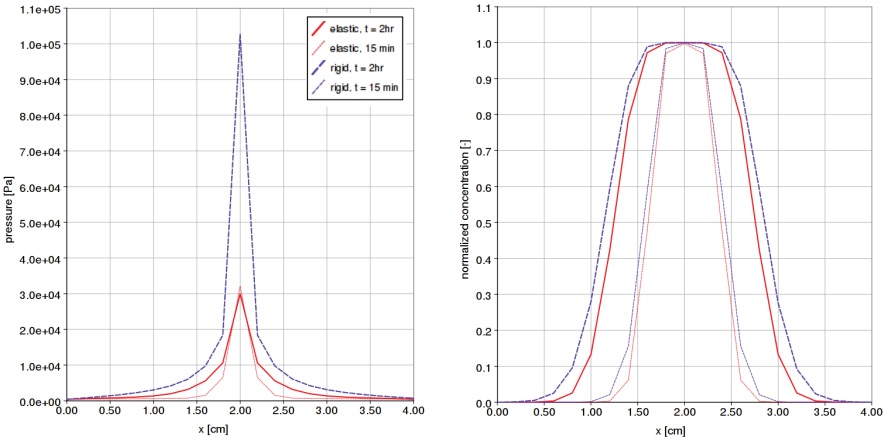

Figure 5.4: Comparison of pressure and concentration distribution for a rigid and an elastic model. In the elastic model lower pressure increases and less spreading of the therapeutic agent are observed.

as in the previous section. Again, the simulations were performed for two hours and the results can be seen in Figure 5.4. Comparing the results of the rigid and the elastic model for $K = 1.82 \cdot 10^{-15} m^2$ a difference in pressures is observed; this is due to changes in the permeability. However, with a Young's modulus of 5000 Pa, there is no significant difference between the resulting concentration distributions. Only for the lowest permeability value, K $= 1.3 \cdot 10^{-16} m^2$, a difference in the distribution could be seen, but this created unreasliticly high pressure increases. In Figure 5.4, the pressure and concentration distribution after 15 min and 2hr are shown for $K = 1.3 \cdot 10^{-16} m^2$. Due to permeability changes, the elastic model produces a significantly lower pressure than the rigid model and, as expected, less spreading of the therapeutic agent is observed. Note that using the Young's modulus from Miller and Chinzei [35], the difference would be significant also for the permeability value of $1.82 \cdot 10^{-15} m^2$ (see Figure 5.3). Therefore, we conclude that it is important to take deformations into account in numerical models describing CED.

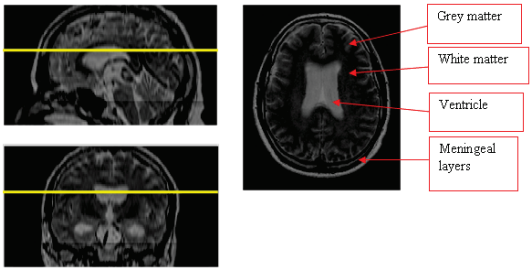

Figure 5.5: T_2 weighted MR-image of the same patient as the DT-images described in Sec.4.2. The cross section that can be seen to the right is through the line that can be seen from the left image. The different compartments are shown. Note that white matter appears darker than grey matter.

5.2 Implementation of Patient-Specific Parameters and Brain Structure

One of the main aims of this study was to investigate effects of anisotropy and heterogeneities on the final concentration distribution of therapeutic agents in brain tissue. As explained in Sec.4.3, Fractional Anisotropy (FA) was used to distinguish between grey and white matter and the tortuosity was used to delineate the ventricles, meningeal layers, and bones from the brain tissue (see Figure 5.5). Since the resolution of the DTI is quite low and only the transport within the parenchyma was considered, the meningeal layer, ventricles and bones were lumped together. Thus, we only distinguished between inside and outside the brain tissue and a low permeability was assigned to elements outside the parenchyma to mimic a no-flow boundary condition. The calibrated diffusion tensor and permeability tensors were used to account for heterogeneities and anisotropy of the tissue. These parameters were all read from a file and assigned element wise, where the voxel size in the DT-images equaled the size of the grid cells, i.e. $2 \cdot 2 \cdot 2mm^3$. The parameter values taken from the literature were the same as given in Table 5.1, unless otherwise specified. Due to computational limits, simulation of the whole brain was not possible; instead a smaller volume of interest were studied. All simulations were performed for 12 hours with an infusion rate of 0.3 ml/hr, and the infusion concentration was, as in the previous section, set to 10^{-7} mole of Gd-DTPA per mole water. In the plots, the normalized concentration is displayed; i.e. the actual concentration divided by the concentration of the agent in the infused fluid.

As in Sec.5.1, we employ Dirichlet boundary conditions (see Table 3.1). Which means that the displacement is forced to zero at the boundary of the VOI. Moreover, we cannot run long simulations since the drug will reach the boundary of the domain after a certain period of time.

The permeability value needed in the calibration procedure of Linninger et al. [32] for white matter was set to $1.82 \cdot 10^{-15} m^2$ [48]. To capture the resistance to the flow in grey matter regions, a reference K of one order of magnitude lower was assigned to it. Finally, outside the brain tissue, a K-value of three orders of magnitude lower than for grey matter was assigned. Darcy's law is not applicable for these regions since they represent free flow regions. However, since the meningeal layers and the boundaries to the ventricles are not resolved and it is assumed that the therapeutic agent cannot freely pass these boundaries, a low permeability was assigned to the entire region and Darcy's law was applied. For the porosity, it was also distinguished between grey- and white matter and inside and outside the brain tissue.

5.2.1 Spreading in 3D

A volume of interest (VOI) was chosen as shown in Figure 5.6 (1). The size of the domain was $6.0 \cdot 9.6 \cdot 5.4 cm^3$, with 38 840 nodes. The results can be seen in Figure 5.6. Note that the porosity field is shown in the background and that white matter appears black since it has lowest porosity. The isolines show the pressure field, divergence of the displacement and the normalized concentration distribution, in Figure 5.6 (2), (3), and (4) respectively. The divergence of the displacement is shown since both the porosity changes and the permeability changes will follow the same distribution pattern. Comparing the results with the isotropic case, the magnitudes of the primary variables are similar, but the distributions are significantly different. The results clearly show preferential flow in the white matter regions and it follows the pattern of the fiber tracts (see Sec. 4.2). Moreover, the location of the infusion is chosen in a region where the diffusion component in z-direction is large. This can clearly be seen as the agent spreads most in z-direction.

5.2.2 Effect of Different Permeability Fields

For the simulations described here, a different VOI was chosen to investigate how the location of the infusion affects the concentration distribution. This VOI represented the whole cross-section in the xy-plane and 1.6 cm in z-direction,

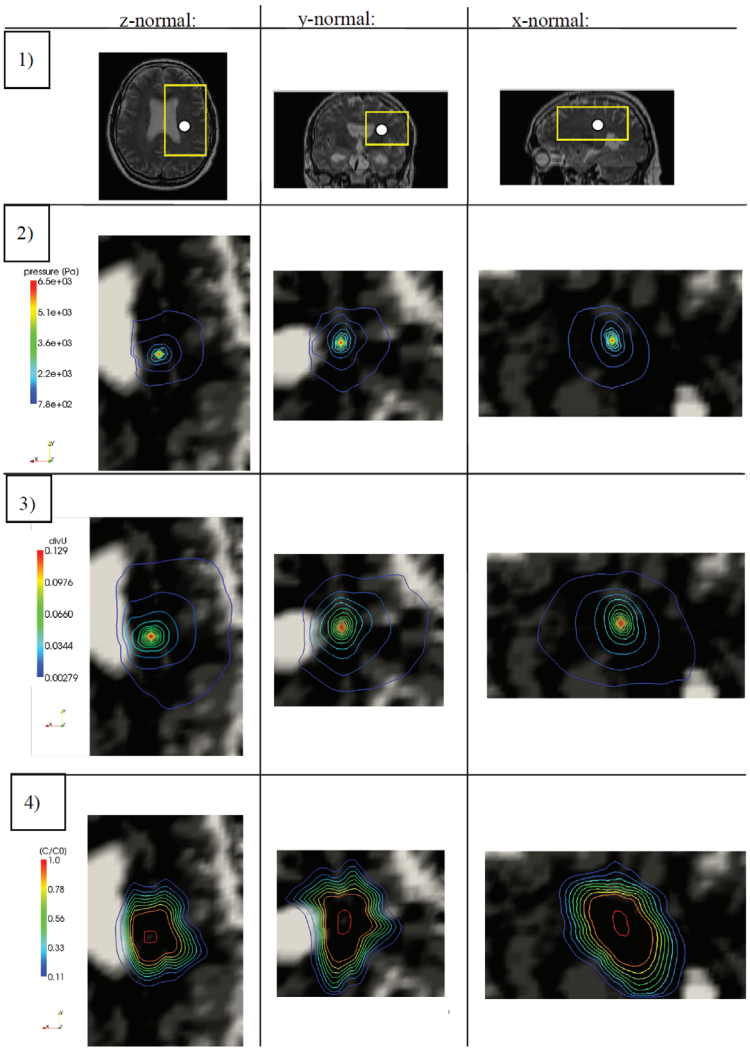

Figure 5.6: Plots showing the results after 12 hours of infusion at a rate of 3 ml/hr based on the the DTI data set from OVGU-Magdeburg University Hospital. 1) Cross sections showing the modelled domain. 2) Pressure fields. 3) Divergence of the displacement, which is shown since both the porosity changes and the permeability changes will follow the same distribution pattern. 4) Concentration distribution. Note, that agent spreads most in z-direction.

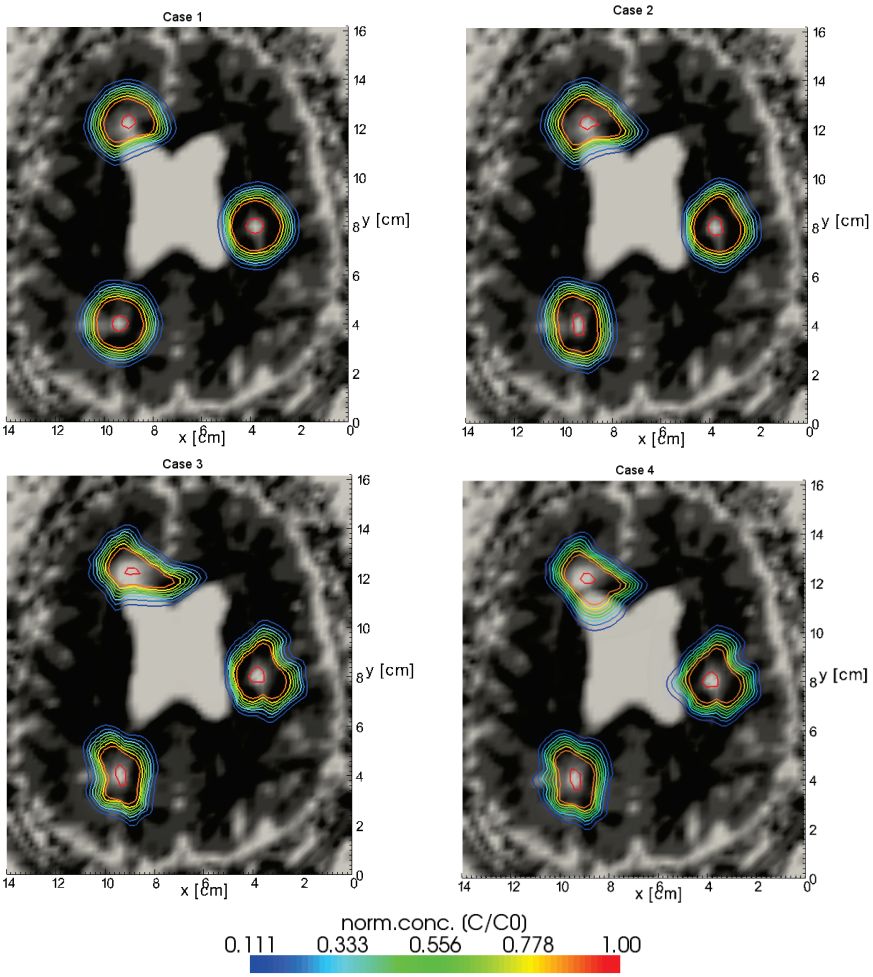

Figure 5.7: Distribution of normalized concentration for the four different cases: Case 1) Isotropic. Case 2) $\mathbf{K}_0$ equal for both grey and white matter. Case 3) $\mathbf{K}_0$ 10 times higher in the white matter regions than in the grey matter regions. Case 4) A high permeability is assigned to the areas outside the brain tissue.

Table 5.2: Different permeability values assigned to the different regions.

		Permeability $[m^2]$		
	Calibration	Outside	Grey Matter	White Matter
Case 1	No	$1.3 \cdot 10^{-19}$	$1.82 \cdot 10^{-15}$	$1.82 \cdot 10^{-15}$
Case 2	Yes	$1.3 \cdot 10^{-19}$	$1.82 \cdot 10^{-15}$	$1.82 \cdot 10^{-15}$
Case 3	Yes	$1.3 \cdot 10^{-19}$	$1.3 \cdot 10^{-16}$	$1.82 \cdot 10^{-15}$
Case 4	Yes	$1.3 \cdot 10^{-13}$	$1.3 \cdot 10^{-16}$	$1.82 \cdot 10^{-15}$

which translates to a domain of $14 \cdot 16.2 \cdot 1.6 cm^3$ with 45 360 nodes. In the following, four different cases with different permeability fields (given in Table 5.2) are compared. The source term, i.e. the location of the infusion, was set at three different locations in the xy-plane (see Figure 5.7). In Case 1, all parameters were initially kept constant, apart from a lower permeability value assigned to the regions defined to be outside the brain tissue. As no calibration of the permeability and diffusion coefficient was done, the brain tissue was assumed to be homogeneous and isotropic. In Case 2, the calibration was performed, but K was set to be equal for grey and white matter. In the two latter cases $K_{wm} = 10K_{gm}$. Thus, case 3 was identical with the simulation done in the previous section, while in Case 4 the permeability outside the brain tissue was set to be three orders of magnitude higher than for the grey matter.

As can be seen in Figure 5.7, the results of Case 1 show that the agent spreads spherically from the injection point apart from in the vicinity of the ventricles. For Case 2, the effect of the anisotropy and heterogeneities as a result of the calibration procedure can be seen. However, in Case 3, the preferential patterns are more evident since K of white matter is one order of magnitude higher than that of grey matter. If results from clinical trials, which indicate similar permeability for grey and white matter, are valid, then the question arises whether Case 2 is sufficient to describe the flow pattern seen during CED. The reason for the resistance to the flow in grey matter is still an open question, but may be related to difference in elastic properties of the media. It could be that there are stronger permeability changes in grey matter than in white matter. If grey matter has a significantly lower Young's modulus than white matter lower pressures and less spreading could be explained by larger deformations in grey matter. Another explanation could be that the coefficient β needed in non-linear equation for the permeability change (eq. 3.15) is significantly different for grey and white matter. Implementing this, the model may reproduce similar pressure elevation

in both regions, even though the permeability and Lamé parameters are in the same order of magnitude. But, this does not explain the physical reason for the observed flow resistance.

In Case 4 the assumption that macromolecules are hindered from entering the CSF was tested. If macromolecules are free to pass the meningeal layers a much larger leakage to CSF will be observed. This is done by assigning a high permeability to the regions defined outside the brain and shows a significant leakage to CSF if the injection was done in the vicinity of the ventricles.

6 Summary and Conclusion

The purpose of this study was to show the workflow from MRI measurements to a computational model with realistic parameters. Patient-specific anatomy and parameters were implemented in a numerical model, which describes flow and transport in an elastic deformable matrix. Information about the anatomy, heterogeneities, and anisotropy of the tissue was obtained from DTI. Fractional anisotropy (FA) was used to distinguish between grey and white matter and tortuosity to differentiate between inside and outside the brain tissue. Moreover, the DT-images were used to determine the orientation of the white matter fiber tracts and calibrate the permeability and diffusion tensors. The resolution of the DT-images used here was 2 mm. This is too low to resolve the meningeal layers. To be able to successfully delineate these geometrical boundaries, DT-images with higher resolution will be needed. As can be seen in Section 5.1.1, the resolution of the mesh affects all results and a mesh with a finer resolution would yield a better estimation of both pressure and displacement. However, the current results are qualitatively valuable and demonstrates that, for the concentration distribution to be affected by deformation, the Lamé parameters and/or the permeability must be low. Comparing a rigid model to the poro-elastic model showed the importance of including elasticity in numerical models describing flow and transport during CED. Furthermore, it demonstrated the importance of reliable parameter values. Finally, the parameters obtained from the DT-images were implemented and the effects of anisotropy and heterogeneity were studied. The calibration was shown to be successful and resulted in preferential flow in the direction of the white matter fiber tracts. The next step will be to include non-linear deformation [47] and perform simulations with a finer mesh based on DTI data with higher resolution.

7 Acknowledgements

We thank the German Research Foundation (DFG) for the funding within the international Research Training Group "Non-Linearities and Upscaling in Porous Media" (NUPUS). Next we would like to thank dr. K. Kopitzki and prof. dr. J. Voges from Otto-von-Guercke-Universitaet Magdeburg for providing MR-data.

References

[1] J. W. Baish, P. A. Netti, and R. K. Jain. Transmural coupling of fluid flow in microcirculatory network and interstitium in tumors. *Microvascular Research*, 53:128–141, 1997.

[2] P. Basser. Interstitial pressure, volume, and flow during infusion into brain tissue. *Microvascular Research*, 44:143–165, 1992.

[3] P. Basser and C. Pierpaoli. Microstructural and physiological features of tissues elucidated by quantitative-diffusion-tensor mri. *Journal of Magnetic Resonance, Series B*, 111:209–219, 1996.

[4] P. Basser, J. Mattiello, and D. Lebihan. Mr diffusion tensor spectroscopy and imaging. *Biophysical Journal*, 66:259–267, 1994.

[5] P. Basser, J. Mattielo, and D. Lebihan. Estimation of the effective self-diffusion tensor from the nmr spin-echo. *Journal of Magnetic Resonance, ser.B*, 103:247–254, 1994.

[6] L. Baxter and R. Jain. Transport of fluid and macromolecules in tumors; the role of interstitial pressure and convection. *Microvascular Research*, 37: 77–104, 1989.

[7] B. Bender and U. Klose. Cerebrospinal fluid and interstitial fluid volume measurements in the human brain at 3t with epi. *Magnetic Resonance in Medicine*, 61:834–841, 2009.

[8] M. Biot. Theory of elasticity and consolidation for a porous anisotropic solid. *Journal of Applied Physics*, 25:182–185, 1955.

[9] R. Bobo, A. L. D.W., Akbasak, P. Morrison, R. Dedrick, and E. Oldfield. Convection-enhanced delivery of macromolecules in the brain. *Proc. Natl. Acad. Sci. USA*, 91:2076–2080, 1994.

[10] W. Brown. *Journal of Chemical Physics*, 23:1514–1517, 1955.

[11] X. Chen and M. Sarntinoranont. Biphasic finite element model of solute transport for direct infusion into nervous tissue. *Annals of Biomedical Engineering*, 35:2145–2158, 2007.

[12] Z. Chen, W. Broaddus, R. Viswanathan, R. Raghavan, and G. Gillies. Intraparenchymal drug delivery via positive-pressure infusion: Experimental and modeling studies of poroelasticity in brain phantom gels. *IEEE Transactions on Biomedical Engineering*, 49(2):85–96, 2002.

[13] S. Cheng and L. E. Bilston. Unconfined compression of white matter. *Journal of Biomechanics*, 40:117–124, 2007.

[14] S. Cheng, E. Clarke, and L. Bilston. Rheological properties of the tissues of the central nervous system: A review. *Medical Engineering and Physics*, 30:1318–1337, 2008.

[15] S. Cowin and L. Cardoso. Fabric dependence of wave propagation in anisotropic porous media. *Biomechanical Modeling in Mechanobiology*, 10: 39–65, 2011.

[16] T. Dutta-Roy, A. Wittek, and K. Miller. Biomechanical modelling of normal pressure hydrocephalus. *Journal of Biomechanics*, 41:2263–2271, 2008.

[17] B. Flemisch, M. Darcis, K. Erbertseder, B. Faigle, A. Lauser, K. Mosthaf, S. Muthing, P. Nuske, A. Tatomir, M. Wolff, and R. Helmig. Dumux: Dune for multi-phase, component, scale, physics, ... flow and transport in porous media. *Advances in Water Resources*, In Press, Corrected Proofs, 2011. doi: DOI:10.1016/j.advwatres.2011.03.007.

[18] J. Garcia and J. Smith. A biphasic hyperelastic model for the analysis of fluid and mass transport in brain tissue. *Annals of Biomedical Engineering*, 37:375–386, 2009.

[19] G. Gillies, J. Smith, J. Humphrey, and W. Broaddus. Positive pressure infusion of therapeutic agents into brain tissues: Mathematical and experimental simulations. *Technology and Health Care*, 13:235–243, 2005.

[20] R. Groothuis. The blood-brain and blood-tumor barriers: A review of stragies for increasing drug delivery. *Neuro-Oncology*, pages 45–59, 2000.

[21] P. Hagmann, L. Jonasson, P. Maeder, J. Thiran, V. Wedeen, and R. Meuli. Understanding diffusion mr imaging techniques: From scalar diffusion weighted imagin to diffusion tensor imaging and beyond. *RadioGraphics*, 26:S205–S223, 2006.

[22] M. Hassanizadeh and W. Gray. General conservation equations for multi phase systems: 3. constitutive theory for porous media flow. *Advances in Water Resources*, 3:25–40, 1980.

[23] R. Helmig. *Multiphase Flow and Transport Processes in the Subsurface.* Springer-Verlag, Heidelberg,, 1997.

[24] M. Holz, S. Hei, and A. Sacco. Temperature-dependent self-diffusion coefficients of water and six selected molecular liquids for calibration in accurate 1h nmr pfg measurements. *Phys. Chem. Chem. Phys.*, 2:4740–4742, 2000.

[25] M. Kaczmarek, R. Subramaniam, and S. Neff. The hydromechanics of hydrocephalus: Steady-state solutions for cylindrical geometry. *Bulletin of Mathematical Biology*, 59(2):295–323, 1997.

[26] S. Kalyanasundaram, V. Calhoun, and K. Leong. A finite element model for predicting the distribution of drugs intracranially to the brain. *The American Journal of Physiology*, 273:R1810–R1821, 1997.

[27] H. Kim, M. Lizak, G. Tansey, K. Csaky, M. Robinson, P. Yuan, N. Wang, and R. Lutz. Study of ocular transport of drugs released from an intravitreal implant using magnetic resonance imaging. *Annals of Biomedical Engineering*, 33(2):150–164, 2005.

[28] J. Kim, G. Garett, X. Chen, T. Mareci, and M. Sarntinoranont. Voxelized model of interstitial transport in the rat spinal cord following direct infusion into white matter. *Journal of Biomechanical Engineering*, 131:071007 (8 pages), 2009.

[29] J. H. Kim, T. Mareci, and M. Sarntinoranont. A voxelized model of direct infusion into the corpus callosum and hippocampus of the rat brain: model development and parameter analysis. *Medical and Biological Engineering and Computing*, 48:203–214, 2010.

[30] D. Klatt, U. Hamhaber, P. Asbach, J. Braun, and I. Sack. Noninvasive assessment of the rheological behavior of human organs using multifrequency mr elastography: a study of brain and liver viscoelasticity. *PHYSICS IN MEDICINE AND BIOLOGY*, 52:7281–7294, 2007.

[31] W. Lai and W. Mow. Drag-induced compression of articular cartilage during a permeation experiment. *Biorheology*, 17(1-2):111–123, 1980.

[32] A. Linninger, M. Somayaji, T. Erickson, X. Guo, and R. Penn. Computational methods for predicting drug transport. *Journal of Biomechanics*, 41:2176–2178, 2008 a.

[33] A. Linninger, M. Somayaji, M. Mekarsk, and L. Zhang. Prediction of convection-enhanced drug delivery to the human brain. *Journal of Theoretical Biology*, 250:125–138, 2008 b.

[34] S. McGuire, D. Zaharoff, and F. Yuan. Nonlinear dependence of hydraulic conductivity on tissue deformation during intratumoral infusion. *Ann.Biomed.Eng*, 37(7):1173–1181, 2006.

[35] K. Miller and K. Chinzei. Mechanical properties of brain tissue in tension. *Journal of Biomechanics*, 35:483–490, 2002.

[36] P. F. Morrison, D. W. Laske, H. Bobo, E. Oldfield, and R. Dedrick. High-flow microinfusion: tissue penetration and pharmacodynamics. *Am J Physiol Regulatory Integrative Comp Physiol*, 266:292–305, 1994.

[37] P. Netti, L. Baxter, Y. Boucher, R. Skalak, and K. Rakesh. Time-dependent behavior of interstitial fluid pressure in solid tumors: Implications for drug delivery. *Cancer Research*, 55:5451–5458, 1995.

[38] P. Netti, L. Baxter, Y. Boucher, R. Skalak, and R. Jain. Macro- and microscopic fluid transport in living tissues: Applications to solid tumors. *AIChE Journal*, 43(3):818–831, 1997.

[39] C. Nicholson. Diffusion and related transport mechanisms in the brain tissue. *Reports on Progress in Physics*, 64:815–884, 2001.

[40] A. Odgaard. Three-dimensional methods for quantification of cancellous bone architecture. *Bone*, 20(4):315–328, April 1997.

[41] A. Odgaard, J. Kabel, B. van Rietbergen, M. Dalstra, and R. Huiskes. Fabric and elastic principal directions of cancellous bone are closely related. *Journal of Biomechanics*, 30(5):487–495, 1997.

[42] S. Prabhu, W. Broaddus, G. Gillies, W. Loudon, Z.-J. Chen, and B. Smith. Distribution of macromolecular dyes in brain using positivepressure infusion: a model for direct controlled delivery of therapeutic agents. *Surgical Neurology*, 50:367–375, 1998.

[43] R. Raghavan, M. Brady, M. Rodriguez-Ponze, A. Hartlep, C. Pedain, and J. Sampson. Convection-enhanced delivery of therapeutics for brain disease, and its optimization. *Neurosurgical Focus*, 20(3):E12, 2006.

[44] M. Sarntinoranont, R. Banerjee, R. Lonser, and P. Morrison. A computational model of direct interstitial infusion of macromolecules into spinal cord. *Annals of Biomedical Engineering*, 31(4):448–461, 2003.

[45] M. Sarntinoranont, X. Chen, J. Zhao, and T. Mareci. Computational model of interstitial transport in the spinal cord using diffusion tensor imaging. *Ann. of Biomed. Engr.*, 34:1304–1321, 2006.

[46] A. Sen and S. Torquato. Effective conductivity of anisotropic two-phase composite media. *Physical review B*, 39:4504–4515, 1988.

[47] J. Smith and J. Garcia. A nonlinear biphasic model of flow-controlled infusions in brain: Mass transport analyses. *Journal of Biomechanics*, 44: 524–531, 2011.

[48] J. Smith and A. Humphrey. Interstitial transport and transvascular fluid exchange during infusion into brain and tumor tissue. *Microvascular Research*, 73:58–73, 2007.

[49] J. A. Smith and J. A. Garcia. A nonlinear biphasic model of flow-controlled infusion in brain: Fluid transport and tissue deformation analyses. *Journal of Biomechanics*, 42:2017–2025, 2009.

[50] Z. Taylor and K. Miller. Reassessment of brain elasticity for analyses of biomechanisms of hydocephalus. *Journal of Biomechanics*, 37:1263–1269, 2004.

[51] D. Tuch, V. Wedeen, A. Dale, J. George, and J. Belliveau. Conductivity tensor mapping of the human brain using diffusion tensor mri. *Proc. Nat. Acad. Sci.*, 98:11697–11701, 2001.

[52] I. Vorisek and E. Sykova. Measuring diffusion parameters in the brain: comparing the real-time iontophoretic method and diffusion-weighted magnetic resonance. *Acta Physiol.*, 195:101–110, 2009.

[53] X.-Y. Zhang, J. Luck, W. Dewhirst, and F. Yuan. Interstitial hydraulic conductivity in a fibrosarcoma. *American Journal of Physiology*, 279:H2726–H2734, 2000.

Paper II

CSF flow in Chiari I and syringomyelia from the perspective of Computational Fluid Dynamics

CSF flow in Chiari I and syringomyelia from the perspective of Computational Fluid Dynamics

Karen-Helene Støverud, Kent-André Mardal, Victor Haughton, Hans Petter Langtangen

Abstract

Introduction: Phase contrast MR in patients with the Chiari I malformation demonstrates abnormal CSF flow in the foramen magnum and upper cervical spinal canal, related to abnormal pressure gradients. The purpose of this study was to analyze the role of CSF pressure in the pathogenesis of syringomyelia, with computational models.

Methods: The spinal cord was modeled as a cylindrical poro-elastic structure with homogenous and isotropic permeability. The permeability was then made heterogeneous and anisotropic to represent the different properties of the central canal, gray and white matter. Fluid with a defined pressure, varying both in time and space, was prescribed in the SAS. Simulations were performed to quantify deformations and fluid movement within the cord.

Results: In the simulations with uniform permeability fluid moved into the cord in regions of higher pressure and out of the cord in regions of lower pressure. With permeability differences simulating gray and white matter the pattern was more complex, but similar. Adding the central spinal canal, fluid moved into the cord as in the previous case. However, preferential flow along the central canal hindered fluid from flowing back into the SAS.

Conclusions: Pressure gradients in the SAS produce movement of fluid in the spinal cord. Assuming different relative permeability in gray matter, white matter and the central spinal canal, abnormal CSF gradients lead to accumulation of fluid within and adjacent to the spinal cord central canal.

1 Introduction

Oscillatory CSF flow in the Subarachnoid Space (SAS) is coupled to the cardiac cycle. In systole the arteries in the brain expands and since the skull is rigid CSF

is forced to flow out of the cranial vault into the spinal SAS. During diastole the flow is reversed and CSF flows back into the cranial SAS. In Chiari I patients increased flow velocities are observed with PC MR [1, 2, 5, 7, 9, 13, 14, 16]. Yet, with the present criteria, PC MR does not effectively differentiate symptomatic Chiari malformations from asymptomatic ones. To gain a better insight of cyclic CSF flow and how it affects the spinal cord tissue, mathematical and computational models are potentially powerful tools. In the spinal subarachnoid space, if the inlet and outlet velocities are known, the pressure and velocity fields can be determined at every point in the anatomy for any period of time. Linge et al. [11] studied CSF velocity and pressure in spatio-temporal detail in an idealized geometry and found greater velocities anterior than posterior to the cord and greater velocities below than at the foramen magnum. Moreover, jets and bidirectional flow, i.e. synchronous cephalad and caudad flow, were evident. The advantage of an idealized geometry is that anatomic features can be changed one at the time to mimic both normal and pathologic conditions. For instance, Hentschel et al. [8] visualized how decreasing the cross-sectional area of the SAS results in increased CSF velocities in an idealized geometry. Roldan et al. [15] created patient-specific geometries of the cervical SAS in a normal volunteer and in a Chiari patient. Velocity profiles obtained from PC MR were used as inlet and outlet velocities. Roldan et al. found, as did Linge, that peak velocities and pressure gradients increased in the Chiari patient compared to the healthy volunteer. Thus, both the study by Linge et al. [11] and Roldan et al. [15] concluded that CSF flow is characterized by jets, synchronous bidirectional flow and greater velocities anterior than posterior to the cord both in normals and Chiari patients. The difference is that in Chiari patients all these phenomena are increased. In terms of CSF pressure, Chiari patients have larger and steeper pressure gradients in the SAS than normal subjects (see Figure 1.1). PC MR studies have been used to validate the velocity profiles calculated by computational models. This was done for a cross-section at the level of foramen magnum [14, 15] and at multiple cross-sections in a study by Shah et al. [16]. The comparison from Roldan et al. [15] is shown in Figure 1.2. As mentioned, Chiari patients have steeper pressure gradients in the regions where the SAS is narrowed. In the following, the effect of abnormal CSF pressures on the spinal cord will be studied.

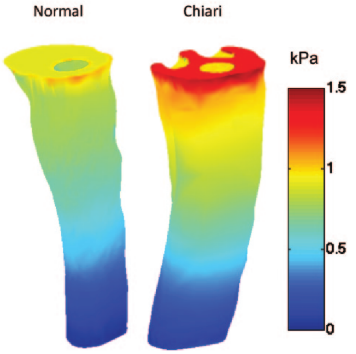

Figure 1.1: Pressure distribution at the inlet and along the outer spinal canal surface for the normal (left) and Chiari I (right) models during peak systole. A 1-5-fold higher pressure gradient was found in the Chiari I model. (from Roldan et al. [15])

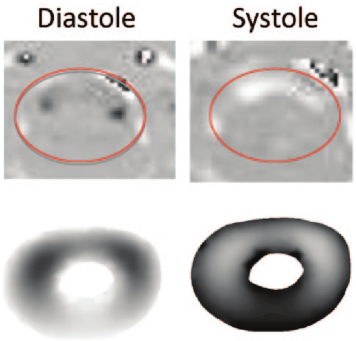

Figure 1.2: Comparison of PC-MR recorded velocity profiles (top) and results from simulations (bottom) in the Chiari I model during diastole (left) and systole (right). Reasonable qualitative agreement is evident by inspection (from Roldan et al. [15])

2 Methods

2.1 Computational Fluid Dynamics

Computational models are widely used by scientists and engineers in numerous fields from the oil industry to biomechanics. In the following, computational models are used to describe pressure and velocity in the SAS and investigate how CSF pressure gradients affect the spinal cord. Flow through the SAS and the interstitial space of the spinal cord is described by Newtons 2nd law, conservation of mass and material parameters. These physical laws are expressed in terms of mathematical equations, discretized and implemented with the finite element method in the FEniCS project [12].

2.2 Quantifying fluid flow and deformations

in the spinal cord tissue The mathematical model is based on the consolidation theory for an elastic porous medium developed by Biot [3]. The spinal cord is modeled as a porous structure with voids, through which fluids can flow. A linear-elastic porous medium has the additional property of being deformable under a given load, returning to the initial state when the load is removed. In the model, the spinal cord is treated as a linear-elastic porous medium where the neurons, glial cells and vasculature make up the solid matrix through which extracellular fluid moves [6, 10]. We used Youngs modulus and Poisson ratio to describe the elastic properties of the cord tissue, and permeability to represents the resistance to flow in a porous medium. Values for these material parameters were obtained from Smith and Humphrey [17] and Cheng et al. [4]. The Youngs modulus and Poisson ratio were assumed to be uniform, while the permeability was assumed to be heterogeneous, with gray matter having a lower permeability than white matter. Furthermore, the fiber structure in the white matter was assumed to cause anisotropic flow resistance with lower resistance in the direction of the fibers than transversely. Gray matter, was assumed to have isotropic resistance. To mimic the central canal a higher permeability was assigned to the central canal of the spinal cord model. Fluid with a defined pressure, based on the pressure profile shown in Figure 1.1 Roldan et al. [15], was prescribed in the SAS. The longitudinal pressure gradient was assigned to the boundary of the model. To represent the partial obstruction of the SAS in Chiari patients a steeper pressure gradient was applied at the level of the tonsils. Below this level, a less steep gradient was applied. Simulations were performed to quantify deformations and fluid movement within the interstitial space of the spinal cord

under different conditions. First with a uniform permeability, then with heterogeneous and anisotropic permeability representing the different properties of gray and white matter and finally with a central canal in which a low value for resistance was assumed.

3 Results

In the simulations with uniform permeability in the cord fluid moved into the cord in regions of higher pressure and out of the cord in regions of lower pressure. In the model with permeability differences simulating gray and white matter, the pattern was more complex, but similar. With the addition of the central spinal canal (see Figure 3.1), fluid moved into the cord as in the previous case. However, preferential flow along the central canal and diminished flow back into the SAS was observed. In regions of high pressure (see Figure 3.1 (middle)) the cord undergoes compression and the interstitial space in the cord diminishes in size. In regions of lower pressure the tissue expands and the interstitial space becomes larger, producing the appearance of edema and the presyrinx state. With a uniform permeability the contraction and expansion are concentrated in the region with the steepest pressure gradient. With the inclusion of the central canal the expansion and contraction appears in a different level in the model. Thus, fluid accumulates in the central spinal canal below the fluid accumulating in the cord.

4 Conclusions

Computational modeling has proven to be a powerful technique for characterizing oscillatory CSF flow and pressure. It provides full 3D profiles with higher spatial and temporal resolution than PC MR. The results from computational models predicts increased jets, bidirectional flow and regions with steeper pressure gradients in Chiari I compared to healthy volunteers. Computer simulations confirm the effect of tonsilar herniation on CSF flow, and show that the alterations in flow can explain the presyrinx state and the development of syringomyelia. Pressure gradients in the SAS produce movement of the interstitial fluid in the spinal cord. Assuming different relative permeability in gray matter, white matter and the central spinal canal, abnormal pressure gradients lead to accumulation of fluid within the cord below the steepest pressure gradient and fluid in the spinal cord central canal below the region where interstitial fluid

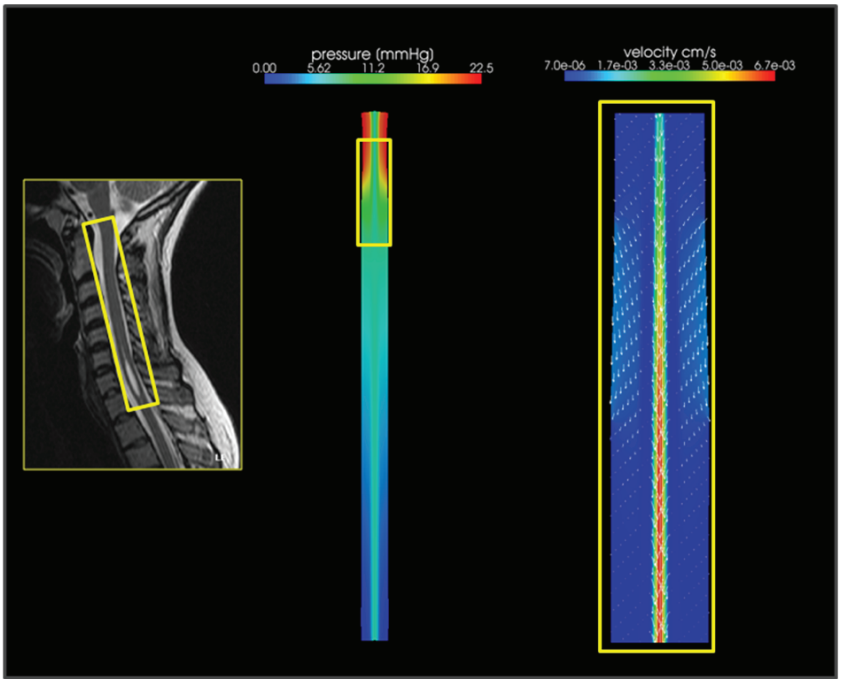

Figure 3.1: MR image of a patient with syringomyelia, where a ROI is indicated to show the modeled region. (middle) The pressure field obtained assuming different permeability of the central canal, grey and white matter. (right) The velocity profile shown for the region with steepest pressure gradient. The colors indicate the magnitude and the arrows the direction of the flow of the interstitial/extracellular fluid. Fluid enters the spinal cord in regions of high pressures. Furthermore, preferential flow along the central canal and diminished flow back into the SAS was observed.

accumulations.

References

[1] R. A. Armonda, C. M. Citrin, T. Foley, and R. G. Ellenbogen. Quantitative cine-mode magnetic resonance of Chiari I malformation: An analysis of cerebrospinal fluid dynamics. *Neurosurgery*, 35(2):214–224, 1994.

[2] R. A. Bhadelia, A. R. Bogdan, S. M. Wolpert, S. Lev, B. A. Appignani, and C. B. Heilman. Cerebrospinal fluid flow waveforms: Analysis in patients with Chiari I malformation by means of gated phase-contrast MR imaging velocity measurements. *Radiology*, 196:195–202, 1995.

[3] M. Biot. General theory of three-dimensional consolidation. *Journal of Applied Physics*, 12:155–164, 1941.

[4] S. Cheng, E. C. Clarke, and L. E. Bilston. Rheological properties of the tissues of the central nervous system: a review. *Medical Engineering and Physics*, 30:1318–1337, 2008.

[5] D. Enzmann and N. J. Pelc. Normal flow patterns of intracranial and spinal cerebrospinal fluid defined with phase-contrast cine MR imaging. *Radiology*, 178:467–474, 1991.

[6] G. Gillies, J. Smith, J. Humphrey, and W. Broaddus. Positive pressure infusion of therapeutic agents into brain tissues: Mathematical and experimental simulations. *Technology and Health Care*, 13:235–243, 2005.

[7] D. Greitz, K. Ericson, and O. Flodmark. Pathogenesis and mechanics of spinal cord cysts. *International Journal of Neuroradiology*, 5(2):61–78, 1999.

[8] S. Hentschel, K. A. Mardal, A. E. Løvgren, S. O. Linge, and V. Haughton. Characterization of cyclic CSF flow in the foramen magnum and upper cervical spinal canal with MR flow imaging and computational fluid dynamics. *American Journal of Neuroradiology*, 31:997–1002, 2010.

[9] B. J. Iskandar, M. Quigley, and V. Haughton. Foramen magnum cerebrospinal fluid flow characteristics in children with Chiari I malformation before and after decompression. *Journal of Neurosurgery*, 60:707–711, 2004.

[10] M. Kaczmarek, R. P. Subramaniam, and S. R. Neff. The hydromechanics of hydrocephalus: Steady-state solutions for cylindrical geometry. *Bulletin of Mathematical Biology*, 59(2):295–323, 1997.

[11] S. O. Linge, V. Haughton, A. E. Løvgren, K. A. Mardal, and H. P. Langtangen. CSF flow dynamics at the craniovertebral junction studied with an idealized model of the subarachnoid space and computational flow analysis. *American Journal of Neuroradiology*, 31:185–192, 2010.

[12] A. Logg and G. N. Wells. Dolfin: Automated finite element computing. *ACM Transactions on Mathematical Software*, 37(2):1–28, Apr. 2010. ISSN 00983500. doi: 10.1145/1731022.1731030.

[13] G. Pinna, F. Alessandrini, A. Alfieri, M. Rossi, and A. Bricolo. Cerebrospinal fluid flow dynamics study in Chiari I malformation: implications for syrinx formation. *Neurosurgical Focus*, 8, 2000.

[14] M. F. Quigley, B. J. Iskandar, M. A. Quigley, M. N. Nicosia, and V. Haughton. Cerebrospinal fluid flow in foramen magnum: Temporal and spatial patterns at MR imaging in volunteers and in patients with Chiari I malformation. *Radiology*, 232:229–232, 2004.

[15] A. Roldan, O. Wieben, V. Haughton, T. Osswald, and N. Chesler. Characterization of csf hydrodynamics in the presence and absence of tonsillar ectopia by means of computational flow analysis. *American Journal of Neuroradiology*, 30:941–946, 2009.

[16] S. Shah, V. Haughton, and A. M. del Río. CSF flow through the upper cervical spinal canal in Chiari I malformation. *American Journal of Neuroradiology*, 32(6):1149–1153, 2011.

[17] J. Smith and A. Humphrey. Interstitial transport and transvascular fluid exchange during infusion into brain and tumor tissue. *Microvascular Research*, 73:58–73, 2007.

Paper III

CSF pressure and velocity in obstructions of the subarachnoid spaces

CSF pressure and velocity in obstructions of the subarachnoid spaces

Karen H. Støverud, Hans Petter Langtangen, Victor Haughton, and Kent-Andre Mardal

Abstract

Obstruction of CSF flow, according to some theories, produces a pressure drop in the subarachnoid space in accordance with the Bernoulli theorem, that explains the development of syringomyelia below the obstruction. However, Bernoulli's principle applies to inviscid stationary flow unlike CSF flow. Therefore, we perform a series of computational experiments to investigate the relationship between pressure drop, flow velocities, and obstructions under physiologic conditions.

We created geometric models with dimensions approximating the spinal subarachnoid space with varying degrees of obstruction. Pressures and velocities for constant and oscillatory flow of a viscid fluid were calculated with the Navier-Stokes equations. Pressure and velocity along the length of the models were also calculated by the Bernoulli equation and compared with the results from the Navier-Stokes equations.

In the models, fluid velocities and pressure gradients were approximately inversely proportional to the percent of the channel that remained open. Pressure gradients increased minimally with 35% obstruction and with a factor 1.4, 2.2 and 5.0 respectively with 60, 75 and 85% obstruction. Bernoullis law underestimated pressure changes by at least a factor 2 and predicted a pressure increase downstream of the obstruction, which does not occur. For oscillatory flow the phase difference between pressure maxima and velocity maxima changed with the degree of obstruction.

Inertia and viscosity which are not factored into the Bernoulli equation affect CSF flow. Obstruction of CSF flow in the cervical spinal canal increases pressure gradients and velocities and decreases the phase lag between pressure and velocity.

1 Introduction

An obstruction of the subarachnoid space, such ectopic position of the cerebellar tonsils in the Chiari I malformation, increases pressure gradients and velocities

in the CSF during the cardiac cycle [1, 6, 29, 36]. These changes have yet not been adequately quantified because of deficiencies in measurement techniques and because of the confounding effect of inter-individual variations. The role of flow obstruction in Chiari and syringomyelia has not been adequately evaluated [34].

Previous studies do not clarify whether viscous and inertial forces must be considered in the analysis of CSF flow. In one theory of syringomyelia pathogenesis, CSF pressure and velocity have an inverse relationship as predicted by the Bernoulli equation, that lacks terms for inertia and viscosity [12, 13]. Other literature suggests that viscous and inertial forces have a significant effect on CSF dynamics [25]. In a physical model of obstruction in the spinal subarachnoid space, pressure diminishes gradually with distance along unobstructed portions of the model and more steeply in regions of obstruction without an increase in pressure downstream from the obstruction, predicted in the absence of viscous forces [26]. Studies of CSF pressure and velocity performed with computational fluid dynamic (CFD) show phase differences between peak CSF pressure and peak velocity, an indication that viscous and inertial effects have a role in CSF flow [7, 22, 23]. Recent theories suggest that the timing of the velocity and pressure pulsations affects the CSF flow in the perivascular spaces [4], and obstructions disturb the phase-shift between these pulsations [7]. A systematic study of the nonlinear relation between velocity, pressure and obstruction under reasonable physiological conditions has not been performed.

CFD in patient-specific geometries has been used and validated in the evaluation of CSF flow [15, 31, 32]. Utilizing idealized geometries in place of patient-specific models in CFD permits selected variables to be studied in isolation [18, 22, 23, 25]. We created a simplified model of obstruction and used realistic parameters for CSF viscosity and oscillation. We calculated pressure and velocity with the Navier-Stokes equations which have terms for viscosity and inertia. We compared these results with calculations from the Bernoulli equation, in which viscous and inertial forces are neglected.

2 Methods

2.1 Geometric models

Idealized models of the cervical spinal subarachnoid space with a 1.5 cm diameter outer cylinder and a 1.0 cm diameter inner cylinder both 10 cm length were made in NETGEN [33]. The walls of the models were assumed to be imper-

meable and rigid. In one model the fluid space had the same cross-sectional area from the top to the bottom. In the other models, we placed an elliptical enlargement of the inner cylinder of 1.2, 1.33, 1.4 or 1.44 cm diameter at the midpoint of the model. The enlargement was 2 cm in length in each case. We converted the models into tetrahedral computational meshes consisting of interconnected nodes in the same program. The meshes consisted of approximately 4 million cells, with some variation related to the volume of the fluid space. The minimum distance between nodes was 0.2 mm and the maximum 2 mm. The finest resolutions were applied in the obstructed region. A layered mesh structure with higher resolution was used next to walls. The adequacy of the spatial resolution was tested by running the simulations with a coarser and a finer mesh. We calculated the average pressure difference from the time of maximum to the time of minimum pressure at the different mesh resolutions.

2.2 Simulations

We simulated constant and oscillatory flow through the models by solving the Navier-Stokes equations. The Navier-Stokes solver was implemented with the finite element library FEniCS [24] using a semi-implicit pressure correction scheme [8] and linear elements for both velocity and pressure. At the inflow and outflow boundaries, i.e., top and bottom of the geometric models, we defined a plug shaped velocity profile, constant in time or varying sinusoidally. The inflow velocity for constant flow was set to 3.5 cm/sec. The period of the sinusoidal inflow profile was set equal to 0.85 sec to simulate a typical heart rate and the stroke volume was set to 0.85 ml/per heartbeat to achieve a peak velocity at the inlet and outlet of 3.5 cm/sec. At the walls of the fluid space we assumed no-slip boundary condition. The fluid was prescribed as water at body temperature with density $\rho = 1.0 g/cm^3$ and viscosity $\mu = 7 \cdot 10^{-3} gsec/cm$. Gravity was neglected under the assumption that it is balanced by hydrostatic pressures. Flow was calculated at 0.25 milliseconds intervals for the sinusoidal flow profile and at 10 millisecond intervals for the constant profile, starting from resting conditions. For each time step, the Navier-Stokes equations were solved at every node in the computational mesh. For the constant inflow and outflow profile, the simulations were run until the pressure and velocity reached steady state. For the sinusoidal inflow and outflow rate, simulations were performed for four cycles. Snapshots of velocity and pressure were taken in Paraview [17] and were displayed as contour plots by means of Matplotlib in Python [20]. Flow patterns for 0.5 cm at each end of the models, where flow profiles had incompletely developed, were disregarded.

2.3 Quantitative comparison of velocities and pressure

Peak velocities at the midpoint of the model and maximal pressure differences between top and bottom were plotted for each model against the percent obstruction. A curve was fit to the points using `scipy.optimize.leastsq()` [21].

The pressures along the longitudinal axis were tabulated in Paraview for the constant flow rate and at t = 0.28 sec, t = 0.43, and t = 0.64 sec for the sinusoidal flow, with the module Matplotlib in Python [20].

Pressure drops at the level of the obstruction were also calculated from Bernoulli's Law $\left(\frac{1}{2}\rho\left(\mathbf{u}_1^2 - \mathbf{u}_2^2\right)\right)$ based on peak velocities in the straight part $(\mathbf{u}_2)$ and obstructed part $(\mathbf{u}_2)$ of the channel. For constant inflow rate we plotted $\frac{1}{2}\rho\mathbf{u}^2 + p$ along the model (ρ = density; $\mathbf{u}$ = velocity; p = pressure) using the computed velocities and pressures at the center of the fluid channel.

We calculated local maximal Womersley numbers (W)

$$W = L\sqrt{\frac{2\pi\rho}{T_s\mu}} \tag{2.1}$$

which describe the ratio of the local fluid acceleration to the viscous forces acting on it. The characteristic length (L) was defined as $L = \sqrt{\frac{A}{\pi}}$, where A represents the cross-sectional area at the midpoint of the model, and T_s the duration of systole, which was set to 0.43 sec.

We calculated local maximal Reynolds number, the ratio of inertial to viscous forces, as

$$Re = \frac{\rho\mathbf{u}_{max}L}{\mu}, \tag{2.2}$$

where $\mathbf{u}_{max}$ is the peak velocity.

3 Results

3.1 Geometric model

The model had cross sectional areas of the fluid space reduced by 35%, 60%, 75%, and 85% respectively for diameters of 1.2, 1.33, 1.4 and 1.44 cm. The models had a smooth transition from unobstructed to obstructed regions. For simulations at 3 mesh resolutions the average pressures differed with 0.002, 0.02, 0.02, 0.03, and 0.09 cmH2O for 0%, 35%, 60%, 75%, and 85% obstruction respectively. Peak velocities varied by up to 10%. Varying the resolution did

not affect the timing of peak velocities and pressures or the qualitative behavior of the solution.

3.2 Simulations

With flow started from rest, pressure and velocity stabilized by 3 seconds in the constant flow simulations. For the sinusoidal flow simulations, in all models, the velocity and pressure plots over time from the first to the fourth cycle were indistinguishable. The mean volume flux, that is the integral of the normal velocity over the cross sectional area, was constant along the length of the models, showing that volume (mass) conservation was fulfilled in the simulations. Axial images showed that velocity varied with distance from the walls, while pressure did not.

3.2.1 Unobstructed model

For the constant inflow and outflow rate the velocity had an unchanging profile along the length of the model. In the axial plane the velocity peaked in the center of the channel and progressively decreased towards the walls. For a sinusoidal inflow and outflow rate, velocity varied both with location in the channel and phase of the cycle. During times of high velocity, velocities varied from zero at the wall to maximal in the center of the channel (Figure 3.1). When flow reversed, flow in the center of the channel maintained the direction of flow during the last half cycle as flow near the wall began to move in the opposite direction; resulting in synchronous bidirectional flow.

For constant inflow, pressure changed linearly from top to bottom along the length of the model. With sinusoidal inflow and outflow, the pressure gradient oscillated continuously with peaks at t = 0.03 sec and t = 0.46 sec and zero gradient at t = 0.24 sec and t = 0.66 sec.

3.2.2 Obstructed models

In the obstructed models, the velocity profiles in the obstructed regions differed from those in the unobstructed model while in the regions away from the obstruction they did not differ visibly from those in the unobstructed model (Figure 3.1). With constant inflow and outflow rate, larger peak velocities were present in the narrowed region of the fluid space than in the regions upstream and downstream to the obstruction. For sinusoidal inflow and outflow conditions, velocities were greater in the region of obstruction than upstream or

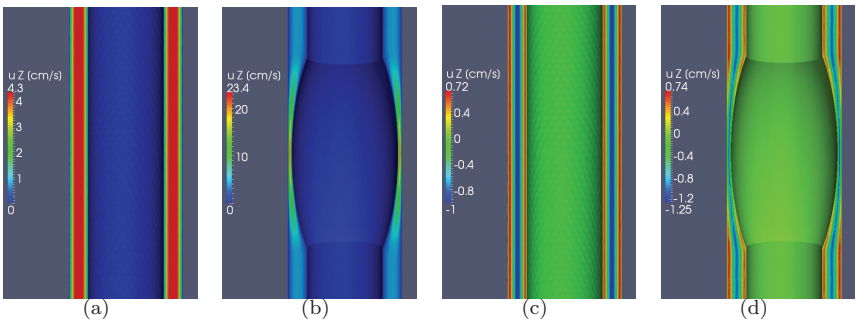

(a) (b) (c) (d)

Figure 3.1: Color display of velocities in the midline plane at maximal flow (a, b) and flow reversal (c, d) in the 0% (left) and 75% obstructed (right) models. At the time of maximal flow, the velocities in the fluid space have a maximum in the center of the channel and near zero flow at the edge of the channel. In the unobstructed model, velocities increased from zero at the edge to its maximum in the center of the channel. In the unobstructed model, velocities remain constant along the length of the model. In the obstructed model, fluid flows with greater velocity at the level of the obstruction. Above and below the obstruction, flow has the same velocities and velocity profile as in the unobstructed model. Mean flux, the integral over the cross sectional area is constant along the length of the model. At the time of flow reversal, velocities are positive in direction near the wall of the fluid chamber and negative in the center of the fluid space, indicating bidirectional flow. When flow reverses direction again, the negative and positive velocities occur again, with their locations with respect to the wall reversed. The mean velocity is zero at this time. In the obstructed model at the time of flow reversal, velocities at the level of obstruction are negative only. Above and below the obstruction, both positive and negative velocities are present (bidirectional flow)

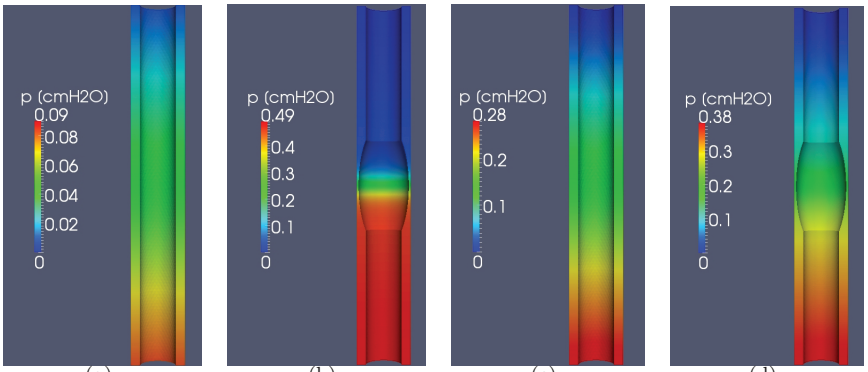

(a) (b) (c) (d)

Figure 3.2: Color display of pressures in the midline at the time of peak flow (left) and flow reversal (right) in the 0% and 75% obstructed models. In the unobstructed model pressure decreases progressively along the length of the model at the time of peak flow. In the obstructed model at peak flow, the pressure gradient is steeper at the level of obstruction than above and below the obstruction. At the time of flow reversal, pressure gradients in the unobstructed model are larger than at the time of peak flow. In the obstructed model the pressure decreases less steeply over the obstruction.

downstream to the obstruction, except during the phases of the cycle with least flow volumes. Peak velocities increased at the level of obstruction as the degree of obstruction increased. As in the unobstructed model, the velocity peaked in the center of the channel and decreased towards the wall, where it was zero. At the time when flow direction reversed, bidirectional flow was evident upstream and downstream to the obstruction and at the obstruction in models with less than 75% obstruction (Figure 3.1). Away from the obstruction, velocity profiles did not change along the long axis of the model.

For the constant flow condition, pressure varied along the length of the obstructed models nonlinearly, with greater decrease per unit length in regions of obstruction. The pressure decrease in the obstructed region varied with the degree of obstruction. For oscillatory inflow and outflow rate, the pressure varied with time and with position along the long axis of the model. As with the constant inflow rate, the pressure decreased more rapidly at the level of the obstruction than downstream or upstream to the obstruction during most

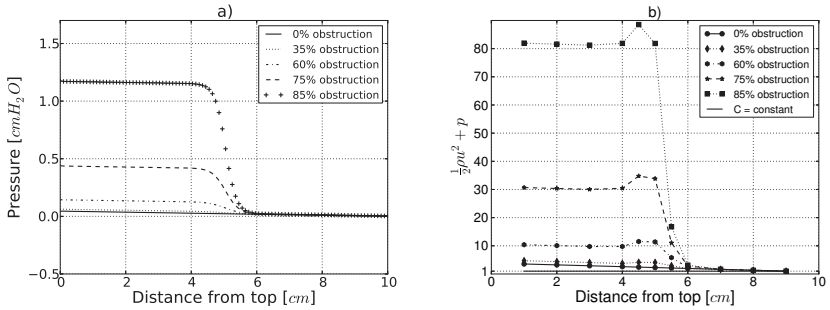

Figure 3.3: a) Plot of pressure in cmH20 during constant flow along the unobstructed and obstructed models. Pressure decreases steeply at the level of obstruction (4-6 cm from the top of the model) and diminishes less steeply along the unobstructed portions of the models. Pressure is assumed to be 0 at the bottom end of the model. b) In the Bernoulli equation, $\frac{1}{2}\rho\mathbf{u}^2 + p$, is assumed constant along a streamline. The deviation of this quantity from its value at the outlet shows the error in Bernoullis law as a function of the distance from the outlet. In unobstructed regions the deviations are relatively small, e.g., for the unobstructed model the deviation reaches a factor 3.5 at the top of the model. At the obstruction (4-6 cm from the top) the deviations are large, e.g. the deviation reaches a factor 60 at the level of an 85% obstruction.

of the cycle (Figure 3.2). The pressure profile along the length of the model varied with the phase of the cycle, having less steep gradients at the level of obstruction when the flow diminished and reversed (Figure 3.1). At times in the cycle, the pressure gradient was biphasic, that is it varied in one direction between the top and the bottom of the model and varied in a different direction over the obstruction (Figure 3.7).

3.3 Quantitative comparison of velocities and pressure

3.3.1 Constant flow

Velocity for the constant inflow condition, in the unobstructed model ranged from 0 at the wall to 5.3 cm/sec, in the center of the channel anywhere along the length of the model. In obstructed models, peak velocities in the obstructed regions were 7.9, 13.7, 23.1, and 34.0 cm/sec with 35, 60, 75 and 85% obstruction respectively.

Pressure differences for constant flow were 0.04 cmH2O in the unobstructed model and 0.06, 0.14, 0.43, 1.17 cmH2O with a 35%, 60%, 75% and 85% obstruction respectively Figure 3.3(a).

By the Bernoulli equation $\left(\frac{1}{2}\rho\mathbf{u}^2 + p = constant\right)$ the pressure difference was 0.04, 0.08, 0.2 and 0.3 cmH2O with a 35%, 60%, 75% and 85% obstruction respectively, considerably lower than the pressure differences calculated for constant flow with the Navier-Stokes equations. Using the computed velocities and pressures, the term $\frac{1}{2}\rho\mathbf{u}^2 + p$, which is assumed invariable in the Bernoulli equation deviated from the value at the inflow by a factor of 3.5 to 80 in the obstruction models Figure 3.3(b).

3.3.2 Oscillatory flow

For oscillating inflow, peak velocity in the unobstructed model was 5.2 cm/sec, near the center of the channel anywhere along the length of the model. When flow reversed, velocities of 1 cm/sec were present one direction with a velocity of 0.7 cm/sec in the opposite direction. In obstructed models, peak velocities were 7.7, 13.8, 23.4, and 35 cm/sec respectively (Figure 3.4). The velocity was inversely proportional to the percent of cross sectional area remaining. The obstructed models had bidirectional flow upstream and downstream to the obstruction of similar magnitude as in the unobstructed model. In the obstructed region, bidirectional flow was apparent in models with up to 60% obstruction.

Pressure differences reached 0.3, 0.4, 0.6, and 1.3 cmH2O for the 35, 60, 75 and 85% obstruction respectively compared to 0.26 cmH2O in the unobstructed model (Figure 3.5).

The timing of the maximal pressure differential varied with degree of obstruction. For the 0% obstruction the pressure gradient peaked at t = 0.46 sec, a 75 degree phase shift compared to velocity (Figure 3.6). With increasing obstruction, the phase difference changed to 72, 59, 35 and 10 degrees for the 35%, 60%, 75% and 85% obstruction respectively. Concordantly, pressure differences at peak velocity changed as the degree of obstruction changed. At peak flow, the pressure difference over the obstacle increased from 0.03, 0.1, 0.4 to 1.2 cmH2O respectively for the 35%, 60%, 75% and 85% obstruction models (Figure 3.6). The change in pressure gradient at the level of obstruction had a different temporal pattern than it had upstream and downstream to the obstruction (Figure 3.7(b)).

Deviations of the term $\frac{1}{2}\rho\mathbf{u}^2 + p$ in the Bernoulli equation at locations along the model from inflow were greater for oscillatory flow than for constant flow.

Womersley numbers ranged from 7 at the level of 85% obstruction to 18 at

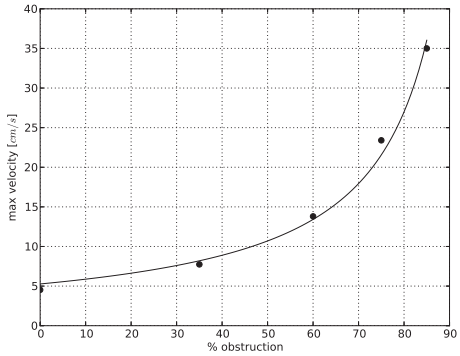

Figure 3.4: Plot of peak velocities as a function of obstruction of the fluid space. The dots represent the computed peak velocities and the solid line the fitted curve. The velocity increases at 35and continues to increase inverse proportionally to the percent of channel that remains open.

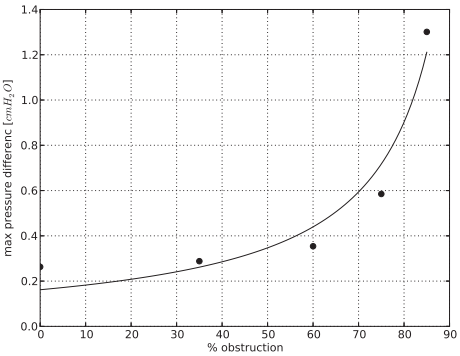

Figure 3.5: Plot of pressure difference between top and bottom of the models as a function of percent of obstruction of the fluid space. Pressure differences increase slowly for obstruction of 60% or less and steeply and more steeply for obstructions of 75 and 85%. The curve shows that the pressure is nearly inverse proportional to the percent of the channel that remains open.

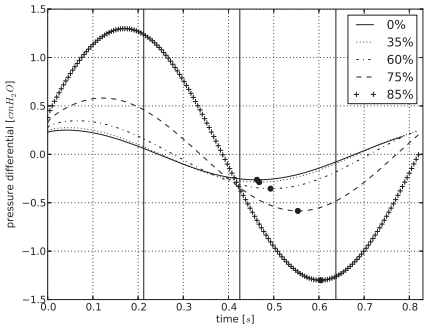

Figure 3.6: Plot of pressure difference between top and bottom of the models as a function of time in the cycle. As the level of obstruction increases, the magnitude of pressure difference increases. As the degree of obstruction increases the time of the maximal pressure processes to a later time in the cycle. In the unobstructed model the pressure gradient peaks at 0.46 sec; in the most obstructed model it peaks at 0.61 sec, a change of 65 degrees in the cardiac cycle.

unobstructed levels. For Womersley numbers less than 10, pressure and velocity were nearly in phase. For Womersley numbers greater than 10, pressure gradient and velocity differed in phase by as much as 75 degrees. Bidirectional flow occurred in a model only when the Womersley number exceeded 10. The local Reynolds numbers ranged from about 350 to 1050 at peak velocity. Reynolds numbers increased as obstruction increased.

4 Discussion

Obstruction of the subarachnoid space in the model produced non-linear increases in velocities and pressures. It reduced synchronous bidirectional flow in the vicinity of the obstruction, caused larger and multiphasic pressure gradients and changed the phase difference between velocity and pressure oscillations. It changed pressures and velocities differently for oscillatory than for constant flow, due to inertial forces. Pressures and velocities did not accord with Bernoullis law, which neglects inertial and viscous forces in effect in CSF. Specifically pressure did not increase downstream of an obstruction as the Bernoulli law predicts

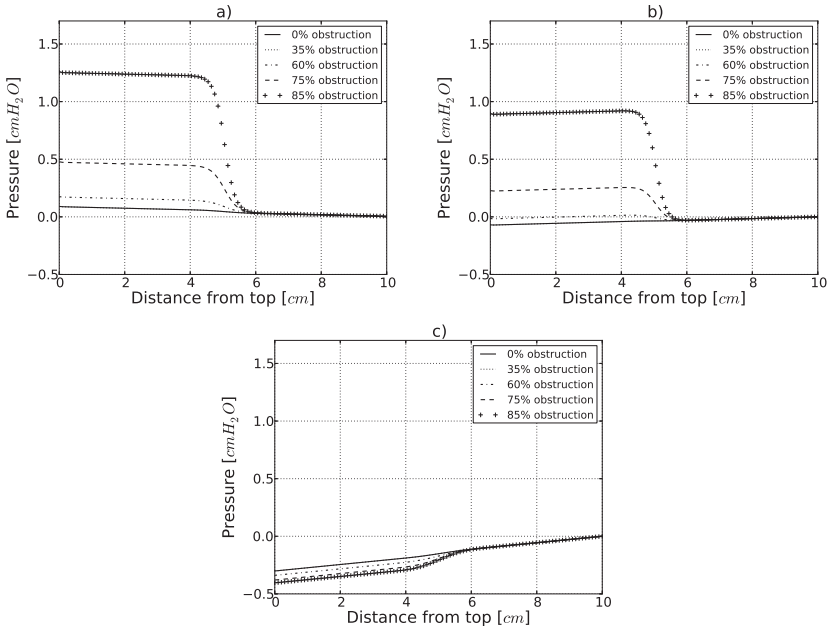

Figure 3.7: Plots of pressure along the length of the unobstructed and obstructed models to illustrate different pressure fields during oscillatory flow. One pattern (a) has pressure diminishing with distance along the model more steeply near the obstruction than at a distance from the obstruction. This pattern occurs at peak inflow (t = 0.21). At another time in the cycle (b), pressure has a bimodal fluctuation along the models, with pressure decreasing with distance near the obstruction. This occurs when flow is in the process of reversing (t = 0.28 sec). It reflects the fact that the pressure wave has a later phase near the obstruction than away from it. Another pattern (c) has pressure increasing along the models, more steeply near the obstruction than at a distance from it. This plot illustrates pressures at t = 0.43 sec.

for non-viscous fluids.

To isolate the effect of obstruction of the fluid space, the models were simplified in geometry and in flow patterns, although physiologically correct fluid viscosity and rate of flow oscillation were retained. The dimensions of the models and the length of the cycle accorded with normal human physiologic CSF flow metrics [14, 25]. In all simulations the stroke volume was kept constant. When the finer mesh was employed, peak inflow velocity decreased, because the boundary layer was better resolved. The maximum velocity difference of 10% does not impact the qualitative results or the conclusions. We have assumed rigid walls in the model since deformations of the spinal have a minor impact on the flow field during the cardiac cycle [11]. However, with this assumption we eliminated a dampening effect on pressure gradients, neglected possible pressure wave phenomena and ignored volume changes or compliance [1], which are second order effects for velocities and pressure. By eliminating permeability of the walls, we omit the fluid exchange between the spinal cord and CSF, which occurs normally [4, 35]. The amount of fluid exchange is currently impossible to measure, although it factors in several theories on the pathogenesis of syringomyelia [3, 4, 16, 27]. Using idealized geometric models and constant or sinusoidal flow as inflow and outflow boundary conditions, we oversimplified CSF flow, probably with the effect of overestimating maximum pressures and velocities in diastole and of underestimating maximum pressures and velocities in systole. The plug shape of the inflow and outflow profile created unphysiologic flow patterns for about 0.5 cm from both ends of the model and therefore these regions were disregarded.

Fluid velocities and pressures in the model are in physiologic ranges. The fluid velocities we observed in the unobstructed model, 5 cm/sec, agree with CSF velocities in normal human subjects [10, 19, 29]. With the highest degrees of obstruction, velocities in the simulations are higher than some published values for CSF [2, 10, 19, 28, 29], but concordant with recent 4D PCMR measurements [5, 6]. The calculated pressures and velocities in the models qualitatively agree with results in a physical model of oscillatory flow in the subarachnoid space [26]. In that model, pressure downstream from an obstruction continued to decrease, as in our study but in disagreement with predictions from Bernoulli's law. The maximal pressure differences we observed are in the range pressure calculated from PCMR measurements [1] or for idealized Chiari I subarachnoid space geometries [22, 23]. In our model, obstruction of 30 or 60% produced velocities from 8 to 14 cm/sec, in the range of velocities found in vivo in the Chiari I malformation [19, 29]. The pressure differentials in our models were substantially lower than what Martin et al. [26] reported although their results

are in qualitative agreement with ours. The phase difference between velocity and pressure oscillation diminished with increasing obstruction, accords with PC MR studies in which Chiari I patients have peak velocities at a different time in the cardiac cycle compared to controls Armonda et al. [2], Pinna et al. [28]. Our results are in agreement with the abnormal phase difference between arterial pulse pressure and CSF pressure in Chiari patients [4]. Synchronous bidirectional flow did not occur at the level of the obstruction in our models but did occur elsewhere. Bidirectional flow increases with increasing Womersley number, i.e, where the flow channel widens. Obstruction of the subarachnoid space has complex effects on CSF pressures, velocities and phase differences between the two. These data indicate that the complexity in CSF dynamics, like the complexity of some blood flow dynamics [9, 30] is not accurately predicted by Bernoulli's law which neglects inertial and viscous forces.

5 Conclusion

Obstruction of CSF flow in the cervical spinal canal increases pressure gradients and velocities and decreases the phase between pressure and velocity. Inertia and viscous forces affect CSF flow. Bernoullis law underestimates the magnitude of the pressure gradients at the obstruction and fails to display temporal differences between velocity and pressure. While inertial and viscous forces have been disregarded in some discussions of CSF flow, this study shows their effects must be factored into future discussions of CSF flow. The Bernoulli equation does not adequately explain CSF flow, despite its application in some theories.

References

[1] N. Alperin, M. Mazda, T. Lichtor, and S. H. Lee. From cerebrospinal fluid pulsation to noninvasive intracranial compliance and pressure measured by MRI flow studies. *Current Medical Imaging Reviews*, 2:117–129, 2006.

[2] R. A. Armonda, C. M. Citrin, T. Foley, and R. G. Ellenbogen. Quantitative cine-mode magnetic resonance of Chiari I malformation: An analysis of cerebrospinal fluid dynamics. *Neurosurgery*, 35(2):214–224, 1994.

[3] M. J. Ball and A. D. Dayan. Pathogenesis of syringomyelia. *The Lancet*, pages 799–801, 1972.

[4] L. E. Bilston, M. A. Stoodley, and D. F. Fletcher. The influence of the relative timing of arterial and subarachnoid space pulse waves on spinal perivascular cerebrospinal fluid flow as a possible factor in syrinx development. *Journal of neurosurgery*, 112(4):808–13, 2010. ISSN 1933-0693. doi: 10.3171/2009.5.JNS08945.

[5] A. C. Bunck, J.-R. Kröger, A. Jüttner, A. Brentrup, B. Fiedler, F. Schaarschmidt, G. R. Crelier, W. Schwindt, W. Heindel, T. Niederstadt, and D. Maintz. Magnetic resonance 4d flow characteristics of cerebrospinal fluid at the craniocervical junction and the cervical spinal canal. *European radiology*, 21(8):1788–1796, 2011.

[6] A. C. Bunck, J. R. Kroeger, A. Juettner, A. Brentrup, B. Fiedler, G. R. Crelier, B. Martin, W. Heindel, D. Maintz, W. Schwindt, and T. Niederstadt. Magnetic resonance 4D flow analysis of cerebrospinal fluid dynamics in Chiari I malformation with and without syringomyelia. *European radiology*, 22(9):1860–70, 2012. ISSN 1432-1084. doi: 10.1007/s00330-012-2457-7.

[7] S. Cheng, M. A. Stoodley, J. Wong, S. Hemley, D. F. Fletcher, and L. E. Bilston. The presence of arachnoiditis affects the characteristics of csf flow in the spinal subarachnoid space: A modelling study. *Journal of biomechanics*, pages 1–6, 2012. ISSN 1873-2380. doi: 10.1016/j.jbiomech.2012.01.050.

[8] A. J. Chorin. Numerical solution of the Navier-Stokes equations. *Math. Comp.*, 22:745–762, 1968.

[9] C. DeGroff, R. Shandas, J. Kwon, and L. Valdes-Cruz. Accuracy of the bernoulli equation for estimation of pressure gradient across stenotic blalock–taussig shunts: an in vitro and numerical study. *Pediatric cardiology*, 21(5):439–447, 2000.

[10] D. Enzmann and N. J. Pelc. Normal flow patterns of intracranial and spinal cerebrospinal fluid defined with phase-contrast cine MR imaging. *Radiology*, 178:467–474, 1991.

[11] L. Fin and R. Grebe. Three dimensional modeling of the cerebrospinal fluid dynamics and brain interactions in the aqueduct of sylvius. *Computer methods in biomechanics and biomedical engineering*, 6(3):163–70, June 2003. ISSN 1025-5842. doi: 10.1080/1025584031000097933.

[12] D. Greitz. Unravelling the riddle of syringomyelia. *Neurosurgical Review*, 29:164–251, 2006.

[13] D. Greitz, K. Ericson, and O. Flodmark. Pathogenesis and mechanics of spinal cord cysts. *International Journal of Neuroradiology*, 5(2):61–78, 1999.

[14] D. Greiz, J. Hannerz, T. Rahn, H. Bolander, and A. Ericsson. MR imaging of cerebrospinal fluid dynamics in health and disease. *Acta Radiologica*, 35: 204–211, 1994.

[15] S. Gupta, M. Soellinger, P. Boesiger, D. Poulikakos, and V. Kortcuoglu. Three-dimensional computational modeling of subject-specific cerebrospinal fluid flow in the subarachnoid space. *Journal of Biomedical Engineering*, 131, 2009.

[16] J. D. Heiss, N. Patronas, H. L. DeVroom, T. Shawker, R. Ennis, W. Kammerer, A. Eidsath, T. Talbot, J. Morris, E. Eskioglu, and E. H. Oldfield. Elucidating the pathophysiology of syringomyelia. *Journal of Neurosurgery*, 91:553–562, 1999.

[17] A. Henderson. *ParaView Guide, A Parallel Visualization Application*. Kitware Inc., 2008.

[18] S. Hentschel, K. A. Mardal, A. E. Løvgren, S. O. Linge, and V. Haughton. Characterization of cyclic CSF flow in the foramen magnum and upper cervical spinal canal with MR flow imaging and computational fluid dynamics. *American Journal of Neuroradiology*, 31:997–1002, 2010.

[19] E. Hofmann, M. Warmuth-Metz, M. Bendszus, and L. Solymosi. Phase-contrast MR imaging of the cervical csf and spinal cord: Volumetric motion analysis in patients with Chiari I malformation. *AJNR*, 21:151–158, 2000.

[20] J. D. Hunter. Matplotlib: A 2d graphics environment. *Computing in Science & Engineering*, 9:90–95, 2007.

[21] E. Jones, T. Oliphant, and P. Peterson. Scipy: Open source scientific tools for python. URL `http://www.scipy.org`.

[22] S. O. Linge, V. Haughton, A. E. Løvgren, K. A. Mardal, and H. P. Langtangen. CSF flow dynamics at the craniovertebral junction studied with an idealized model of the subarachnoid space and computational flow analysis. *American Journal of Neuroradiology*, 31:185–192, 2010.

[23] S. O. Linge, V. Haughton, A. E. Løvgren, K. A. Mardal, A. Helgeland, and H. P. Langtangen. Effect of tonsillar herniation on cyclic CSF flow studied with computational flow analysis. *AJNR. American journal of neuroradiology*, 32(8):1474–81, Sept. 2011. ISSN 1936-959X. doi: 10.3174/ajnr.A2496.

[24] A. Logg, K. A. Mardal, and G. Wells, editors. *Automated Solution of Differential Equations by the Finite Element Method*, volume 84 of *Lecture Notes in Computational Science and Engineering*. Springer, 2012. ISBN 978-3-642-23098-1. doi: 10.1007/978-3-642-23099-8.

[25] F. Loth, M. A. Yardimci, and N. Alperin. Hydrodynamic modeling of cerebrospinal fluid motion within the spinal cavity. *ASME J. Biomech. Engrg.*, 123:71–73, 2001. doi: 10.1115/1.2801670.

[26] B. A. Martin, R. Labuda, T. J. Royston, J. N. Oshinski, B. Iskandar, and F. Loth. Spinal subarachnoid space pressure measurements in an in vitro spinal stenosis model: implications on syringomyelia theories. *Journal of Biomechanical Engineering*, 132(11):1–11, 2010. ISSN 1528-8951. doi: 10.1115/1.4000089.

[27] E. H. Oldfield, K. Muraszko, T. H. Shawker, and N. J. Patronas. Pathophysiology of syringomyelia associated with Chiari I malformation of the cerebellar tonsils. *Journal of Neurosurgery*, 80:3–15, 1994.

[28] G. Pinna, F. Alessandrini, A. Alfieri, M. Rossi, and A. Bricolo. Cerebrospinal fluid flow dynamics study in Chiari I malformation: implications for syrinx formation. *Neurosurgical Focus*, 8, 2000.

[29] M. F. Quigley, B. J. Iskandar, M. A. Quigley, M. N. Nicosia, and V. Haughton. Cerebrospinal fluid flow in foramen magnum: Temporal and spatial patterns at MR imaging in volunteers and in patients with Chiari I malformation. *Radiology*, 232:229–232, 2004.

[30] R. Rieu, R. Pelissier, and K. Isaaz. Accuracy of the simplified bernoulli relationship in measuring pressure gradients across stenosis. *International angiology : a journal of the International Union of Angiology*, 8(4):210–5, 1989. ISSN 0392-9590.

[31] A. Roldan, O. Wieben, V. Haughton, T. Osswald, and N. Chesler. Characterization of csf hydrodynamics in the presence and absence of tonsillar

ectopia by means of computational flow analysis. *American Journal of Neuroradiology*, 30:941–946, 2009.

[32] G. Rutkowska, V. Haughton, S. Linge, and K. A. Mardal. Patient-specific 3D simulation of cyclic CSF flow at the craniocervical region. *AJNR. American Journal of Neuroradiology*, 33(9):1756–62, 2012. ISSN 1936-959X. doi: 10.3174/ajnr.A3047.

[33] J. Schöberl. Netgen -automatic mesh generator. URL `http://www.hpfem.jku.at/netgen/`.

[34] N. Shaffer, B. Martin, and F. Loth. Cerebrospinal fluid hydrodynamics in type I Chiari malformation. *Neurological research*, 33(3):247–60, 2011. ISSN 1743-1328. doi: 10.1179/016164111X12962202723805.

[35] M. A. Stoodley, N. R. Jones, L. Yang, and C. J. Brown. Mechanisms underlying the formation and enlargement of noncommunicating syringomyelia: experimental studies. *Neurosurg Focus*, 8(3), 2000.

[36] B. Williams. Simultaneous cerebral and spinal fluid pressure recordings. 2. cerebrospinal dissociation with lesions at the foramen magnum. *Acta Neurochirurgica*, 59:123–142, 1981.

Paper IV

Effect of pia mater, central canal, and geometry on wave propagation and fluid movement in the cervical spinal cord

Paper V

Computational investigation of CSF dynamics in the 4th ventricle, cranial and cervical subarachnoid space

Computational investigation of CSF dynamics in the 4th ventricle, cranial and cervical subarachnoid space

Karen Støverud, Hans Petter Langtangen and Kent-André Mardal

Abstract

Abnormal cerebrospinal fluid (CSF) dynamics is associated with neurological disorders such as the Chiari I malformation, in which parts of the cerebellum is displaced into the spinal canal. Currently there is no criterion that can distinguish symptomatic Chiari patients from asymptomatic or give an indicator for the optimal treatment of a given patient. Moreover, 4D phase contrast MR (PCMR) studies report more complex flow patterns than both computational fluid dynamics (CFD) and 2D PCMR. Therefore, there is a need for an improved understanding of the CSF dynamics.

In this study, we used CFD to simulate CSF flow and pressure in the cervical subarachnoid space (SAS), cerebellomedullary cistern, pontine cistern, and 4th ventricle in two Chiari patients and one control under subject-specific anatomy and flow conditions.

The results demonstrated substantial differences in flow velocities, pressure drop and flow resistance between the control and the Chiari patients and also between the two Chiari patients. Maximum pressure drop occurred at different times during the cardiac cycle in the different models.

This study reproduced flow jets and vortices seen in 4D PCMR, but did not explain preferential CSF flow observed in the posterior cervical SAS. This indicates that inclusion of at least parts of the cranial SAS is important to reproduce flow patterns seen in vivo.

1 List of Abbreviations

CSF	Cerebrospinal Fluid
SAS	Subarachnoid space
CS	Cervical SAS
C1	First cervical vertebrae
T1	First thoracic vertebrae
FM	Foramen Magnum
Aq	Aqueduct
Vol1	Patient with normal anatomy and flow
P2	Chiari patient 2
P4	Chiari patient 4
PCMR	Phase Contrast Magnetic Resonance imaging
V_{enc}	Velocity encoding

2 Introduction

The Chiari I malformation is a medical condition characterized by the displacement of the cerebellar tonsils through the foramen magnum (FM) into the spinal column (see Figure 2.1). The displaced cerebellar tonsils partially obstruct the subarachnoid space (SAS) at the level of the FM and compress the cerebellum. Symptoms range from severe headache to sleep apnea and muscle weakness. Secondary to a Chiari malformation many patients develop fluid filled cavities within the spinal cord tissue, a condition called syringomyelia. The exact relation between Chiari and syringomyelia remains unclear, but both conditions have been associated with abnormal cerebrospinal fluid (CSF) flow caused by the obstruction of the SAS.

Usually Chiari I is diagnosed from MR images by measuring the distance from the FM to the tip of the cerebellar tonsils. Unfortunately, there is no direct correlation between symptoms in Chiari patients and to which extent the cerebellar tonsils are displaced. Moreover, there is no criterion that can distinguishes symptomatic Chiari patients from asymptomatic ones or give an indicator for the optimal treatment of a given patient. Therefore, alternative measures are needed.

As mentioned, Chiari I is associated with abnormal CSF flow. Phase contrast MR (PCMR) imaging in patients with the Chiari I malformation demonstrates abnormal flow in the foramen magnum and upper spinal canal [3, 9, 10, 12, 28]. The abnormal flow is characterized by increased peak velocities, bidirectional flow, and flow jets. Further, phase differences between peak velocity in healthy

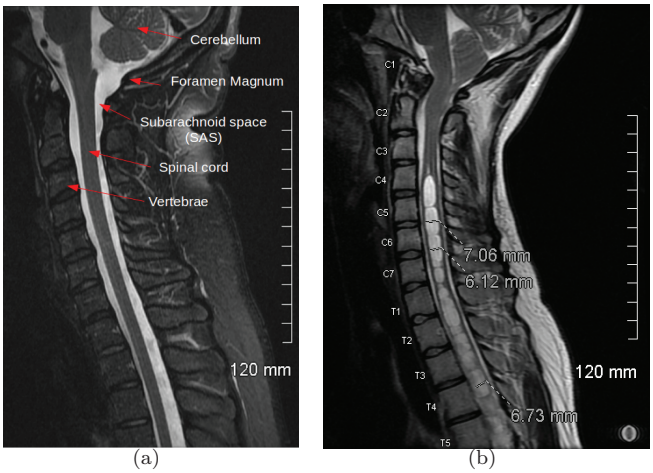

(a) (b)

Figure 2.1: (a) MR image of the cerebellum and spinal cord in a healthy individual. In all pictures white and grey regions indicate fluid and tissue, respectively. (b) Patient with both Chiari I malformation and syringomyelia. The Chiari malformation can clearly be seen by noting how thight the SAS around C1 is. Syringomyelia is identified as the white cavities of CSF within the grey spinal cord from C4 to T4. Notice that the SAS is tight all the way from C1 to T4 in the Chiari patient.

subjects and Chiari patients have been observed [10]. PCMR has become an increasingly popular tool. However, there is no agreement about which velocity features that indicate severity of the malformation [30].

Abnormal CSF velocities implicate abnormal pressure gradients. Measuring pressue is more involved than measuring velocity. Whether PCMR data can be used to obtain reliable pressure estimate is debatable, and pressure measurements are usually done invasively at one or a few locations [11, 35].

Computational fluid dynamics (CFD) provides both pressure and velocity with high temporal and spatial resolution, and has consequently become a popular tool. Both patient specific [14, 29, 37] and idealized geometries [18, 22, 24] have been used in CFD studies. Flow resistance and flow impedance potentially provide more precise measures of the severity of the SAS obstruction and may be quantified accurately by CFD [25, 30, 31].

CFD models have clearly improved our understanding of CSF hydrodynamics. However, 4D PCMR studies have shown [9, 10] more complex flow patterns and higher CSF velocities than found in both CFD and 2D PCMR. A recent study by Yiallourou et al. [37] compared 4D PCMR with CFD simulations, and found large discrepancies between the two approaches. Yiallourou et al. [37] suggested fine anatomical structures as one of the main reasons for the discrepancies. This hypothesis is also supported by a recent study by Mortensen et al. [26].

The aim of the present paper is to propose an alternative explanation of the discrepancies between 4D PCMR measurements and CFD, namely that the complex anatomy of the cranio-cervical junction in Chiari patients and phase-differences between CSF flow in the aqueduct and SAS need to be included for accurate flow calculations. Most CFD studies cut the geometry at or just above FM to reduce the complexity of the anatomy in the computer model. In fact, to the authors knowledge, only the model by Gupta et al. [14] includes the cerebellomedullary cistern, pontine cistern, and the 4th ventricle. However, they only considered flow down to the level of C1 in the normal SAS. In the present paper, we include both the cisterns and the 4th ventricle, and the geometry is cut just above the aqueduct in the rostral end and at the level of C4 in the caudal end. To investigate how the velocity patterns, the pressure drop, and the flow resistance across FM vary with the anatomy, we compare CFD simulations in two Chiari patients and one control subject with normal anatomy. The present paper represents a comprehensive and detailed computational study for understanding how cranial and cervical CSF flow is influenced by complex geometric features of the anatomy.

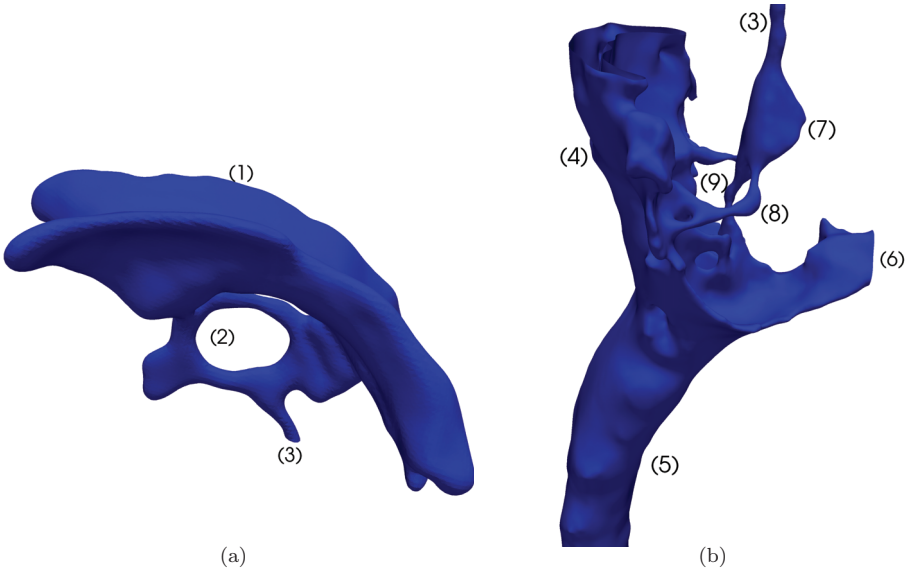

(a) (b)

Figure 2.2: Anatomy of the ventricles and SAS in the brain and cervical spine. Figure (a) shows (1) the lateral ventricles, (2) the 3rd ventricle, and (3) the aqueduct. Figure (b) shows (3) the lower part of the aqueduct, (4) the pontine cistern, (5) the cervical SAS, (6) cerebellomedullary cistern, (7) the 4th ventricle, (8) foramen luschka, and (9) foramen magendie.

3 Medical Background

3.1 Subarachnoid space (SAS) and ventricular system

The SAS is a fluid-filled space situated between the two innermost meningeal layers covering the brain and spinal cord, i.e., the arachnoid mater and the pia mater. The SAS is penetrated by the spinal nerve roots, blood vessels, dental ligaments, and the arachnoid trabeculae. Dental ligaments consist of pairs of thin sheets that connect the pia to the arachnoid mater. The trabeculae consists of a large number of filaments that form a cobweb like structure and becomes a part of the pial membrane. Within the SAS there are regions where the pia and the arachnoid mater are not in close approximation. These regions are called cisterns. In Figure 2.2 two of the cisterns are displayed, namely the pontine cistern and the cerebellomedullary cistern.

The ventricular system is interconected fluid-filled cavities within the brain, which are made up by the large lateral ventricles, and the third and the fourth ventricle (Figure 2.2). The lateral ventricles are connected to the third ventricle through the foramen monro, and the third ventricle is connected to the fourth ventricle by the aqueduct of sylvus. At each side of the fourth ventricle the foramen luschka connects the fourth ventricle to the pontine cistern, and at the bottom, the foramen magendie connects the fourth ventricle and the cerebellomedullary cistern, as illustrated in Figure 2.2.

3.2 Oscillatory CSF flow

The fluid occupying the ventricles and SAS of the brain and spinal cord is called cerebrospinal fluid (CSF) and has properties similar to water [8]. CSF is mainly produced in the ventricular system and enters the SAS through foramen magendie and foramen luschka. CSF flows in a pulsatile manner through the SAS and ventricular system in accordance with the cardiac cycle. In systole, when the blood pressure reaches its maximum value, the arteries in the brain expand, and, since the skull is rigid, CSF is forced to flow out of the cranial vault into the spinal SAS. This process occurs in different phases [4]. First, the CSF in the cranial SAS is flushed into the spinal SAS. Then, blood flows out of the cranial vault through the jugular veins and at the same time the fluid in the 4th ventricle flows into SAS. Finally, CSF flows from the third ventricle and aqueduct into the SAS. The fluid flow from the cranial SAS contributes with about 90% of the flow across FM, while the fluid from the ventricles contributes with only about 10% (see Figure 4.2). During diastole, when the blood pressure reaches

its minimum value, the flow is reversed and CSF flows back into the cranial SAS. Under pathological flow conditions, as those caused by the Chiari I malformation, both the timing and the magnitude of the flow may be significantly disturbed.

4 Methods

4.1 MRI

In the current study we used MR images from one control patient with normal anatomy and two Chiari patients. Throughout the text the control patient is referred to as Vol1 and the Chiari patients as P2 and P4. The patients were females at the age of 40, 26 and 63 years for Vol1, P2, and P4, respectively. P2 has a distinct syrinx at the level of C2.

The MR images was obtained at Oslo University Hospital on a 3T Siemens scanner (Skyra) for Vol1 and on a 3T Philips scanner (Achieva 2.5.3) for P2 and P4. For the segmentation of the SAS and ventricles for the CFD simulations we used T2-weighted turbo spin-echo sequences with a spacing of 0.5 mm x 0.5 mm or 1 mm x 1 mm in the sagital plane and slice thickness of 1 mm.

PCMR images was obtained on the same scanners at the level of FM and in the aqueduct. In the aqueduct the velocity encoding (V_{enc}) was set to 8 cm/s for P2 and P4, while it was set to 16 cm/s for Vol1. At the level of FM the V_{enc} was set to 6 cm/s for P2 and P4 and 10 cm/s for Vol1. The spatial resolution was 0.62 mm x 0.62 mm and 32 images was obtained per cardiac cycle using retrospective ECG-gating.

4.2 From MRI to patient specific geometries

The anatomy of the cervical subarachnoid space, pontine cistern, and the 4th ventricle including the aqueduct was reconstructed using the Vascular Model Tool Kit (VMTK) [2]. The segmentation algorithms in VMTK are based on level set methods (see Appendix A), which were used to extract surfaces representing the dura mater and the pia mater or brain tissue. The extracted surfaces were smoothed and opened in each end to create inflow and outflow boundaries. Finally, computational meshes were generated for Vol1, P2, and P4. In Figure 4.1 the MR images with the initial level set is displayed together with the final surface meshes.

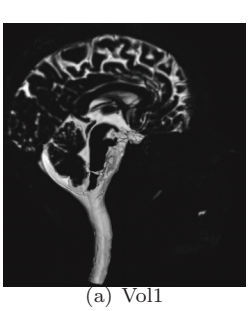

(a) Vol1

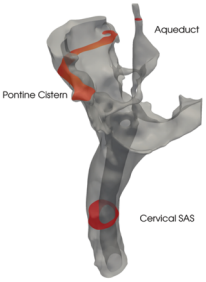

(b) Vol1

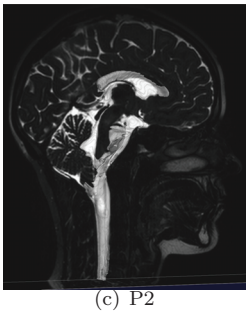

(c) P2

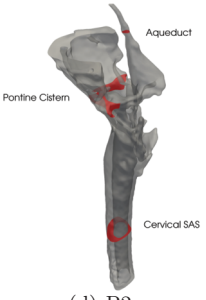

(d) P2

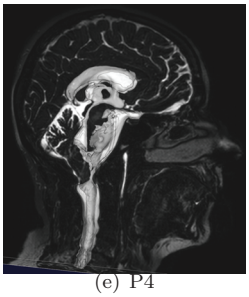

(e) P4

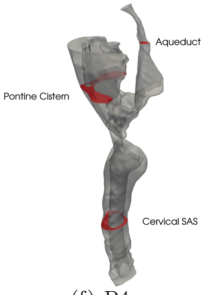

(f) P4

Figure 4.1: MR-images and the segmented surfaces in (a) Vol1, (c) P2, and (e) P4. Notice the very tight CSF space at the level of Foramen Magnum in P4. In (b), (d), and (f) the surface meshes are displayed and the selected cross-sections at which we evaluate the pressure are indicated in red.

4.3 Computational Fluid Dynamics

To simulate CSF flow through the spinal SAS, we applied the Navier-Stokes equations for an incompressible Newtonian fluid

$$\frac{\partial \mathbf{u}}{\partial t} + \mathbf{u} \cdot \nabla \mathbf{u} - \nabla \cdot \boldsymbol{\sigma}(\mathbf{u}, p) = 0, \tag{4.1}$$

$$\nabla \cdot \mathbf{u} = 0. \tag{4.2}$$

Here, $\boldsymbol{\sigma}$ is the Cauchy stress tensor, which is dependent on the strain tensor $\boldsymbol{\epsilon}$ and $\mathbf{u}$:

$$\boldsymbol{\sigma}(\mathbf{u}, p) = 2\nu\boldsymbol{\epsilon}(\mathbf{u}) - p\mathbf{I}, \tag{4.3}$$

$$\boldsymbol{\epsilon}(\mathbf{u}) = \frac{1}{2}\left(\nabla \mathbf{u} + \nabla^T \mathbf{u}\right). \tag{4.4}$$

The primary variables, $\mathbf{u}$ and p, describe the unknown CSF velocity and pressure, respectively, and $\nu = \mu/\rho$ is the kinematic viscosity, involving the fluid density ρ and the dynamic viscosity μ. CSF is, as mentioned, a water-like fluid and behaves as a Newtonian fluid with ρ and μ similar to water at body temperature [8]. Thus, in all simulations we used $\rho = 1000 \left[\frac{\text{kg}}{\text{m}^3}\right]$ and $\mu = 7.0 \cdot 10^{-4} \left[\frac{\text{kgs}}{\text{m}}\right]$.

To solve the governing equations we applied a semi–implicit incremental pressure correction scheme (IPCS). The discretized equations were implemented in the FEniCS [23] application `cbc.flow`.

A consequence of the splitting scheme is that a condition for the pressure must be assigned on the entire boundary. In this study we used homogenous Neumann boundary conditions $\partial p . \partial n = 0$ on all boundaries. Dirichlet conditions were employed for the velocity, as described in detail on page 9.

4.4 Patient specific boundary conditions

The PCMR data from the cranial SAS and the aqueduct was used as inflow/outflow boundary conditions at the caudal end and in the aqueduct of the model, respectively. This is plausible assuming mass conservation of CSF within the cranium and cervical spinal canal.

The PCMR data was analyzed in BioFlows (tidam.fr) [5]. Based on spectral segmentation a region of interest (ROI) was chosen, i.e., the region with CSF

flow. Then volume flux and velocity curves as a function of time were automatically calculated and saved in a spread sheet. The heart rates were 71, 86, and 77 beats per minute for Vol1, P2, and P4, respectively.

The quality of the measured data was high for P2. For P4, V_{enc} was set too low and an antialiasing filter was applied to achieve flow in a uniform direction at each time step. For Vol1, the V_{enc} value was set to 100 mm/s at FM, which was high and caused a low signal to noise ratio and thus uncertainties in the data. For this region we had to do parts of the segmentation manually instead of using spectral segmentation. In 2D PCMR the velocity component perpendicular to the selected slice is found. In the implementation the velocity was therefore multiplied by the normal vector ($\mathbf{n}$).

The resolution of the data is relatively low both in time and space. To be able to evaluate the boundary conditions at any point in time we interpolated between the measured points using cubic splines. The computed flux and corresponding splines can be seen in Figure 4.2. As expected, the flux in the aqueduct was delayed compared to the flux at level of FM, and this delay was most prominent in Vol1. Notice the low flow rate in the aqueduct of P2.

To construct velocity profiles $\mathbf{u}_{\Gamma_i}$ at the inflow/outfile boundaries Γ_i, we distributed the volume flux over the boundary according to a weighting function $\tau(x)$. This function was zero at the wall and increased with the distance from the wall. The velocity profile is then

$$\mathbf{u}_{\Gamma_i} = \frac{Q_i(t)\tau(x)}{\int_{\Gamma_i} \tau(x) d\Gamma_i}\mathbf{n} \tag{4.5}$$

Note that this velocity is not the physically correct velocity, but the imposed variation over the boundary is thought to lead to a shorter distance for developing the correct boundary layer compared to the common choice of a simple plug profile.

The above inflow/outflow conditions apply in the caudal end and in the aqueduct. However, we do not have information about the volume flux through the pontine and cerebellomedullary cisterns. In this study we used the the principle of volume conservation to assign velocity profiles at the remaining inflow/outflow boundaries. That is, we subtracted the flux through the aqueduct from the flux at FM, and the remaining flux was divided into the two areas and scaled by the areas. At the impermeable walls of the SAS we imposed a no-slip boundary condition: $\mathbf{u} = 0$.

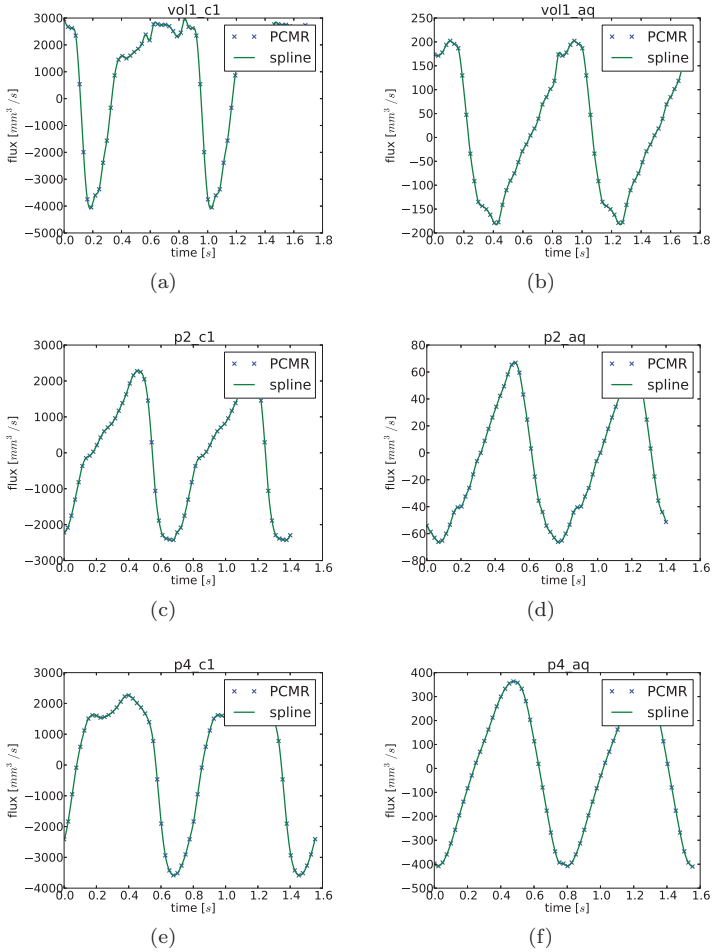

Figure 4.2: Volume flux through the SAS at the level of C1 and in the aqueduct. Figures (a, b) show fluxes in Vol1, (c, d) in P2 and (e, f) in P4. The flow through the aqueduct is approximately 10% of the flow at C1, except in P2 where the flow rate in the aqueduct is low. Notice that the flux in the aqueduct is delayed compared to the flux at the level of FM. This delay is most prominent in Vol1.

4.5 Computations

We simulated oscillatory flow in the SAS in the three segmented geometries. All simulations were performed with a time step of $\Delta t = 10^{-4}$ s for three cardiac cycles. Simulations were initiated with zero-flow velocity, but a steady periodic state was reached already in the second flow cycle. The sensitivity to the spatial resolution is described later.

For the velocity, we evaluated flow patterns at peak systolic inflow, while for the pressure, we computed the spatial average as a function of time at three selected slices in the cervical SAS (CS), aqueduct (Aq), and pontine cistern (PC), as indicated in Figure 4.1. Then we defined the pressure difference between PC and CS as

$$\Delta p_1 = p_{\mathrm{PC}} - p_{\mathrm{CS}}, \tag{4.6}$$

and the pressure difference between Aq and PC as

$$\Delta p_2 = p_{\mathrm{Aq}} - p_{\mathrm{PC}}. \tag{4.7}$$

4.5.1 Hydrodynamical measures

The obstruction of the SAS is expected to increase the flow resistance (R). Resistance between PC and CS was defined as

$$R_1 = \frac{\Delta p_{1_{\max}}}{Q_{CS_{\max}}}, \tag{4.8}$$

where $Q_{CS_{\max}}$ is the peak systolic flow at the cervical inlet. Similarly, resistance between Aq and PC was defined as

$$R_2 = \frac{\Delta p_{2_{\max}}}{Q_{\mathrm{Aq}_{\max}}}, \tag{4.9}$$

where $Q_{\mathrm{Aq}_{\max}}$ is the peak systolic flow in the aqueduct.

We estimated the phase difference θ between Δp and $\mathbf{u}$ by

$$\theta = \frac{t_{\mathbf{u}_{\max}} - t_{\Delta p_{1\max}}}{T}, \tag{4.10}$$

where $t_{\mathbf{u}_{\max}}$ represents the time of peak systolic velocities in CS, $t_{\Delta p_{1\max}}$ the time of peak differential pressure, and T the duration of caudal flow, i.e., duration of systole.

Finally, we computed the Reynolds number, $\mathrm{Re} = \frac{\rho \mathbf{u}_{\max} L}{\mu}$, at peak systolic flow in the aqueduct and in the cervical SAS (see Figure 4.1). We also estimated Re at the level of FM in Vol1 and in the narrow passages at the level of the obstructed SAS in P2 and P4. In the aqueduct L is the diameter of the fluid space at the chosen level. In the cervical SAS and at foramen magnum in Vol1 we defined L to be the diameter of the anterior SAS along the center line of the spinal cord. Further, $\mathbf{u}_{\max}$ was defined as the peak systolic velocity along the diameter L.

4.5.2 Sensitivity to spatial mesh resolution

To check the results for mesh independence, all simulations were performed on two meshes with different resolutions. The meshes corresponding to Vol1 had 9.95 and 18.5 million cells, for P2 the meshes had 8.02 and 16.8 million cells, and for P4 they had 7.91 and 18.9 million cells. We selected two slices where we compared the magnitude of the velocity ($|\mathbf{u}|$) along the lines indicated in Figure 5.7. We defined the maximum percentage difference between the velocities in the two meshes as

$$e_{|\mathbf{u}|} = 100\% \cdot \max \left| \frac{|\mathbf{u}_{\min}^{\mathbf{coarse}}| - |\mathbf{u}_{\min}^{\mathrm{fine}}|}{|\mathbf{u}_{\min}^{\mathrm{fine}}|} \right|, \tag{4.11}$$

where $|\mathbf{u}_{\min}|$ represents the magnitude of the peak systolic velocity. Note that negative velocities are in the caudal direction and positive velocities in the rostral direction. For the pressure we similarly defined the maximum difference between the computations in the two meshes as

$$e_{\Delta p_1} = 100\% \cdot \frac{\Delta p_{1_{\max}}^{\mathrm{coarse}} - \Delta p_{1_{\max}}^{\mathrm{fine}}}{\Delta p_{1_{\max}}^{\mathrm{fine}}}, \tag{4.12}$$

where $\Delta p_{1_{\max}}$ is the maximum pressure difference between the average pressure at the selected slices in the pontine cistern and cervical SAS.

5 Results

5.1 Pressure and pressure drop

Figure 5.1 displays the pressure drop Δp_1 as a function of the time percentage of the cardiac cycle. As mentioned, the pressure at each level represents a spatial

average at the given cross-section. The cardiac cycle was defined to start at flow reversal at the cervical inlet/outlet boundary $t_0 = t_{Q_{CS}=0}$. Maximum Δp_1 was 33.6, 44.4, and 83.9 Pa for Vol1, P2, and P4 respectively (Table 5.1), indicating that the pressure drop across FM increased with increasing levels of obstruction. At peak systolic flow, Δp_1 was close to zero in Vol1 and P2. P4 had $\Delta p_{1_{Q_{\max}}} = 53.6$ Pa, which is a factor ten higher than in P2 and P4 (Table 5.1).

The wave form of Q_{CS} varied between the subjects. Caudal flow lasted 26% of the cycle for Vol1, 47% for P2, and 37% for P4. Peak systolic flow was reached after 8, 17.5, and 14% of the cycle for Vol1, P2, and P4, respectively. Consequently, the maximum pressure differential did not coincide in the different models (see Figure 5.1).

In Figure 5.2, Δp_2 is displayed, and also here we have $t_0 = t_{Q_{CS}=0}$. Maximum Δp_2 was 13.1, 1.4, and 8.2 Pa for Vol1, P2, and P4, respectively (Table 5.1). Due to the low flow rate Q_{Aq} in P2, the peak of Δp_2 was low. Vol1 had the highest peak Δp_2, because of the narrow aqueduct, foramen luschka, and foramen magendie.

Peak Δp_2 did not coincide with peak Δp_1, because the flow in the aqueduct (Q_{Aq}) was delayed compared to the flow in the SAS (Q_{CS}). In Vol1, $Q_{\mathrm{Aq}_{\max}}$ occurred 28% later in the cycle than $Q_{CS_{\max}}$, while in P2 and P4, $Q_{\mathrm{Aq}_{\max}}$ was delayed by 15% and 16%, respectively. The $\Delta p_{2_{\min}}$ quantity coincided with diastolic peak flow $Q_{\mathrm{Aq}_{\max}}$ in Vol1, while systolic peak flow occurred close to $\Delta p_2 = 0$. For P4, Δp_2 was close to zero at peak systolic and diastolic flow, while Δp_2 peaked at flow reversal, i.e., when $Q_{Aq} = 0$.

Table 5.1: Peak systolic velocities at the three given levels (see Figure 4.1), and Δp at its maximum, at its minimum, and at the time of peak systolic flow ($Q_{\max}$).

	$\lvert\mathbf{u}_{\min}\rvert$ CS [mm/s]	$\lvert\mathbf{u}_{\min}\rvert$ Aq [mm/s]	$\lvert\mathbf{u}_{\min}\rvert$ FM [mm/s]	$\Delta p_{1_{\max}}$ [Pa]	$\Delta p_{1_{\min}}$ [Pa]	$\Delta p_{2_{\max}}$ [Pa]	$\Delta p_{2_{\min}}$ [Pa]	$\Delta p_{1_{t_{Q_{\max}}}}$ [Pa]
Vol1	59	134	27	33.6	-17.4	13.1	-14.4	2.8
P2	43	38	123	44.4	-14.6	1.4	-1.5	4.4
P4	98	116	400	83.9	-39.6	8.2	-6.4	53.6

5.2 Velocity

Figures 5.3, 5.4, and 5.5 display streamlines at the time of peak systolic inflow ($t_{Q_{CS_{\max}}}$) in Vol1, P2, and P4, respectively. The velocities increased from FM

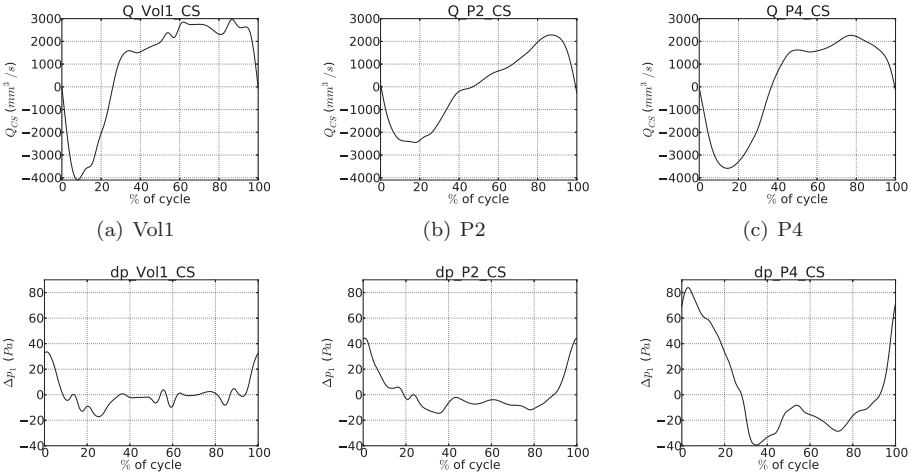

(a) Vol1 (b) P2 (c) P4

(d) Vol1 (e) P2 (f) P4

Figure 5.1: Plot of the volume flux in the cervical SAS (upper row) and pressure drop Δp_1 (lower row). The cycle was defined to start at $t_{Q_{CS}=0}$, which was close to peak pressure in all models. At the time of peak flow, the pressure drop Δp_1 was close to zero in Vol1 and P2, while Δp_1 was large in P4. The duration of systole was longest in P2 and shortest in Vol1.

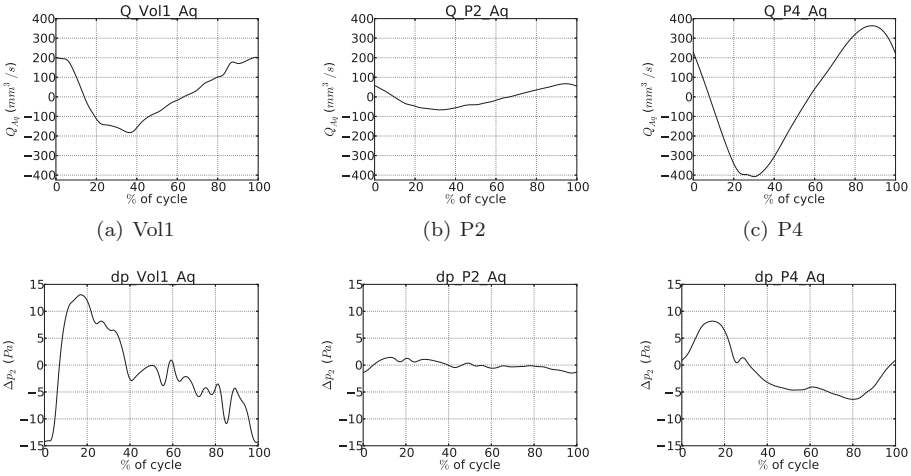

(a) Vol1 (b) P2 (c) P4

(d) Vol1 (e) P2 (f) P4

Figure 5.2: Plot of the volume flux in the aqueduct Q_{Aq} (upper row) and pressure drop Δp_2 (lower row). The cycle was defined to start at $t_{Q_{CS}=0}$ in the cervical SAS, where the volume flux was close to $Q_{\mathrm{Aq}_{\mathrm{max}}}$ in all cases. In Vol1, $\Delta p_{2_{\mathrm{min}}}$ coincided with diastolic peak flow $Q_{\mathrm{Aq}_{\mathrm{max}}}$, while systolic peak flow occurred close to $\Delta p_2 = 0$. For P2, Q_{Aq} was low resulting in small amplitudes of Q_{Aq}. For P4, Δp_2 was close to zero at peak systolic and diastolic flow, while Δp_2 peaked at flow reversal, i.e., when $Q_{Aq} = 0$.

and caudally in all models. Peak systolic velocities are listed in Table 5.1. In Vol1, the flow was uniform and unidirectional and maximum velocity in the cervical SAS was 59 mm/s, while the maximum velocity in the aqueduct was 81 mm/s. The time of peak systolic velocities in the cervical SAS did not coincide with peak velocities in the aqueduct. Therefore, there was flow in opposite directions and flow vortices forming in the 4th ventricle. The maximum velocities (123 mm/s) were higher in P2 than in Vol1, eventhough the inflow, $Q_{CS_{\max}}$, was lower. The maximum velocity occured in the narrow passage between the cranial and cervical SAS, where there was a jet and a tendency to vortex formation. In the cervical SAS, the maximum velocity for P2 was 43 mm/s and for P4 98 mm/s. The maximum velocities (400 mm/s) in P4 were almost four times as high as in P2. In the narrow channels connecting the cranial and cervical SAS flow, jets were forming and these extended below the narrow channels. Vortices formed in the region with larger cross-section areas (Figure 5.5). These vortices caused synchronous bidirectional flow.

Figure 5.6 shws peak systolic flow in the 4th ventricle. Due to a narrow aqueduct in Vol1, the maximum velocities were 134 mm/s in Vol1, compared to only 116 mm/s in P4, despite the fact that the inflow $Q_{\mathrm{Aq}_{\min}}$ was higher in the latter subject. The maximum velocities were low (38 mm/s) in P2 since the flow rate in the aqueduct was low (see Figure 5.2).

5.3 Hydrodynamical measures

The computed resistances R_1 and R_2 in Vol1, P2, and P4 are listed in Table 5.2. (Note that the units are $\frac{\mathrm{g}}{\mathrm{mm}^4\mathrm{s}}$). R_1 was a factor three higher in P4 compared to Vol1, which demonstrates that the resistance increased with increasing levels of obstruction. On the other hand, R_2 was highest in Vol1 due to the narrow aqueduct, foramen luschka and foramen magendie. In Table 5.2 also the phase difference θ is listed. The phase difference was smallest in Vol1 because the time from zero to peak systolic flow was short.

The Reynolds numbers in the cervical SAS (CS), aqueduct (Aq), and at FM are listed in Table 5.2. The Reynolds number in the aqueduct of P2 is low due to the low flow rate. At FM the Reynolds number was 96 in Vol1, 459 in P2, and 1314 in P4.

5.4 Mesh independence

In Figure 5.7 we have plotted the magnitude of peak systolic velocity along the lines in the selected slices for the coarse and fine mesh in Vol1. The resulting

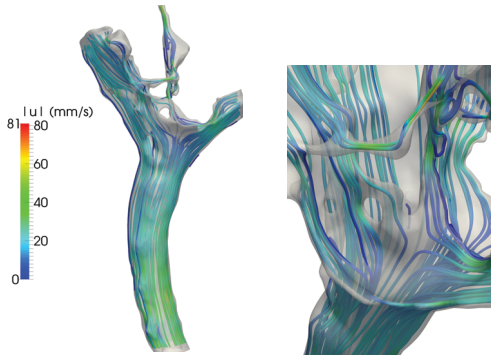

(a) (b)

Figure 5.3: Streamlines at the time of peak systolic inflow in Vol1. Figure (a) shows that the flow is uniform and unidirectional. In the cervical SAS, the velocities increased with distance from FM. Zooming in on flow details in (b) reveals that there was a tendency to vortex formation in the 4th ventricle because of flow in opposite directions.

Table 5.2: Reynolds number at peak systolic inflow, resistance at peak systolic and diastolic flow, and phase difference.

	Re_{CS} [-]	Re_{Aq} [-]	Re_{FM} [-]	$R1_{sys}$ $\left[\frac{\mathrm{g}}{\mathrm{mm^4 s}}\right]$	$R1_{dia}$ $\left[\frac{\mathrm{g}}{\mathrm{mm^4 s}}\right]$	$R2_{sys}$ $\left[\frac{\mathrm{g}}{\mathrm{mm^4 s}}\right]$	$R2_{dia}$ $\left[\frac{\mathrm{g}}{\mathrm{mm^4 s}}\right]$	θ [-]
Vol1	211	397	96	0.008	0.006	0.072	0.072	0.27
P2	156	38	459	0.018	0.006	0.022	0.022	0.36
P4	189	391	1314	0.023	0.017	0.020	0.020	0.31

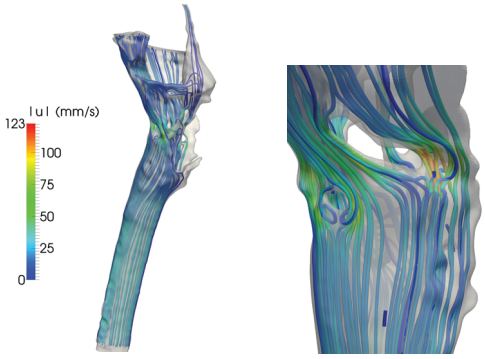

(a) (b)

Figure 5.4: Streamlines at the time of peak systolic inflow in P2. Figure (a) shows that the maximum velocities were higher in P2 than in Vol1, eventhough the peak inflow was lower. Figure (b) shows a jet in the narrow passage between the cranial and cervical SAS and a tendency to vortex formation.

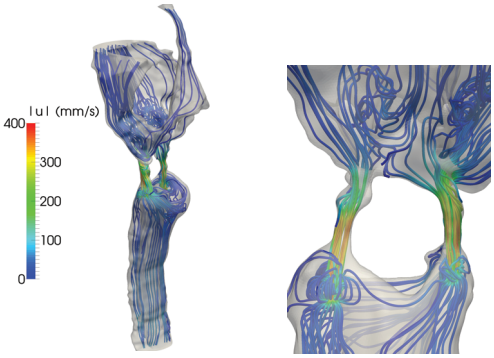

(a) (b)

Figure 5.5: Streamlines at the time of peak systolic inflow in P4. Figure (a) shows that the velocities were almost four times higher in P4 than in P2. Figure (b) illustrates that the flow jets extended below the narrow channels connecting the cranial and cervical SAS and in this region vortices were formed.

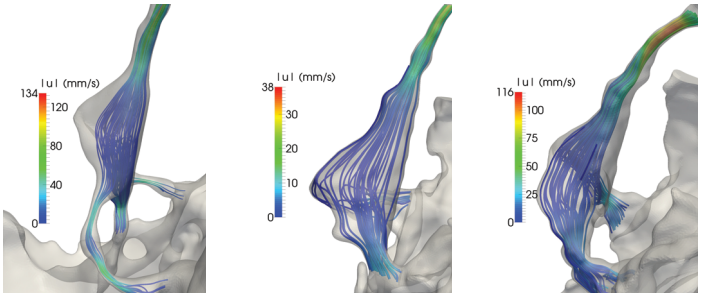

(a) (b) (c)

Figure 5.6: Peak systolic flow in the 4th ventricle. The streamlines shows that the flow is uniform and unidirectional. Figures (a), (b), and (c) come from Vol1, P2, and P4, respectively. Due to a narrow aqueduct, the maximum velocities were higher in Vol1 than P4, although the inflow was higher in the latter. The maximum velocities were low in P2 because of the low inflow rate.

curves for P2 and P4 were similar and are thus not displayed.

At peak systolic flow the maximum discrepancy defined in 4.11 was less or equal to 10% in all subjects outside the vortices. Due to low velocities close to the wall, the relative difference measure was in some cases larger than 10% here.

The differential pressure $\Delta p_{1_{\max}}$ varied by less than 1% between the two meshes for all three subjects.

6 Discussion

6.1 Summary

In the current study, we used CFD to simulate CSF flow and pressure in the cervical SAS, cisterns, and 4th ventricle in two Chiari patients and one control under subject-specific anatomy and flow conditions. The results demonstrated differences in flow velocities, pressure drop, and flow resistance between the control and the Chiari patients and also between the two Chiari patients. The peak systolic velocity at FM was almost a factor five higher in P2 than in Vol1 and a factor 15 higher in P4. The pressure drop across the FM ($\Delta p_{1_{\max}}$) was

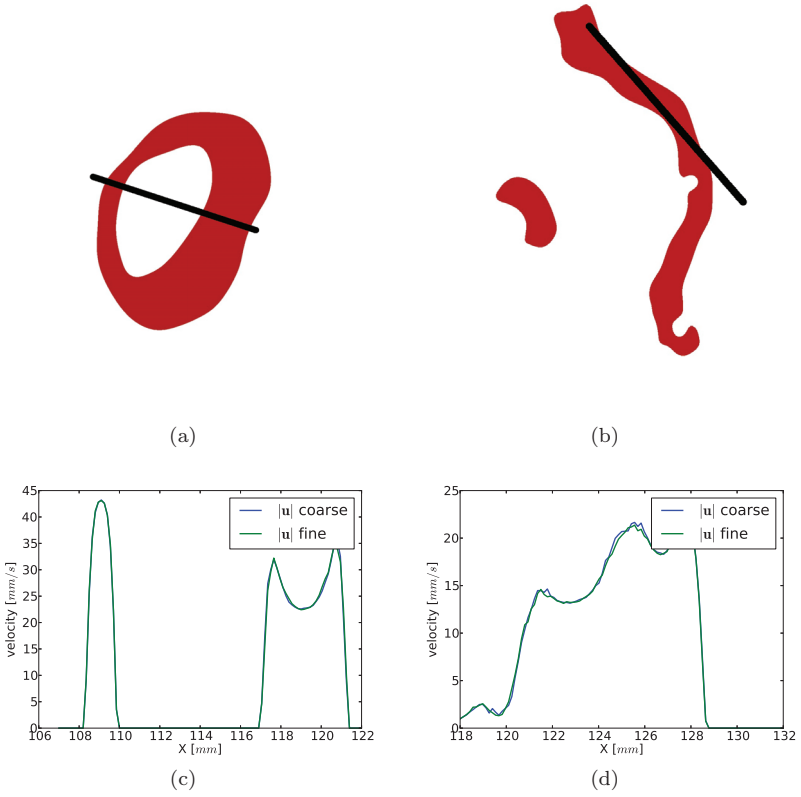

Figure 5.7: Plot of the magnitude of the velocity ($|\mathbf{u}|$) at peak systolic flow along the lines indicated in (a) and (b) for the coarse and the fine mesh in Vol1. The maximum difference in the velocities in the chosen sections was approximately 10%.

in the same range for Vol1 and P2, while it was a factor two higher in P4. Maximum pressure drop occurred at different times during the cardiac cycle in the different models.

The resistance (R_1) in P4 were slightly higher than in P2, and more than twice the resistance in Vol1. In general, the flow was more complex in the Chiari patients with jets forming at peak systolic flow, periods of synchronous bidirectional flow, and reduced phase difference between pressure and flow.

6.2 Limitations

There are a number of limitations in this study caused by uncertainties in the MR data and underlying assumptions in the CFD model.

In the analysis of the PCMR data, we had to use an anti-aliasing filter in P4, and in Vol1 the low signal to noise ratio made it necessary to define the flow region (ROI) manually. To limit the error, the computed flow curves were compared to flow curves computed directly at the MR scanner and found visually identical. Since we did not have PCMR data in the pontine and cerebellomedullary cistern we estimated the flow based on mass conservation. Only Vol1 has a flow inlet in the cerebellomedullary cistern and here the flow rate was scaled by area. However, it has been shown that the volume flow in the cerebellomedullary cistern is only 10% of the volume flow in the pontine cistern [15]. This fact probably leads to an overestimation of the CSF velocities in the cerebellomedullary cistern in Vol1, but in the cervical SAS this effect should be negliglible.

In P4, it is likely that some fluid escaped through other routes than the two narrow channels causing an overestimation of the velocities. In the segmentation process we might have underestimated the connected regions at FM. However, sagital PCMR images through the midline showed no flow at the level of FM and the segmented surfaces were checked by two neuroradiologists who judged them anatomically realistic.

Our computational model employed rigid walls and enforced mass conservation. However, in Yiallourou et al. [37] it was found that the volume flow was changing along the cervical SAS with peak flow at the level of C2, before it decreased caudally. Change in volume flow is most likely due to structural motion of the surrounding tissue.

As most CFD studies we neglected fine anatomical structures in the SAS because of the resolution of and noise in the MR data. Yiallourou et al. [37] argued that fine anatomical structures are one of the main reasons why CFD simulations, including the current study, demonstrate high flow rate in the pos-

terior SAS, while 4D PCMR clearly shows preferred flow in the anterior SAS [9, 10, 37]. This is plausible given that 90% of the CSF enters the cervical SAS via the pontine cistern [15] and the denseness of the trabeculae is lower in the anterior than posterior SAS [37]. It is also possible that the nerve roots and dental ligaments limit the flow from the anterior to the posterior SAS. The spinal nerves has been modeled explicitly in the literature [26], and the trabeculae has been represented in a Lattice-Boltzmann model [33] and also modeled by porous medium approach [14]. These studies show conflicting results regarding the importance of the fine structures.

6.3 Comparison to other studies

Ordinary 2D PCMR reports peak systolic velocities up to 100-120 mm/s in Chiari I patients [3, 6, 12, 13, 19, 27, 28, 32]. On the other hand, 4D PCMR studies have reported peak velocities ranging up to 380 mm/s and more complex flow patterns [10]. In the current study we observed peak velocities up to 400 mm/s and by including the pontine and cerebellomedullary cisterns we reproduced the flow jets and vortices observed in 4D PCMR. Especially in P4, the flow patterns in the region of FM were similar to data by Bunck et al. [10].

The peak velocities computed at systolic flow in P4 were high, resulting in a Reynolds number of about 1300, The high Reynolds numbers suggest that the assumption of laminar flow may be questionable as also suggested in a recent study [17]. The observed vortices resulted in synchronous bidirectional flow throughout the flow cycle and not only at the time of flow reversal as was the case in, e.g., [34].

The pressure drop was in accordance with previous CFD studies [7, 21, 22, 37] and comparable to measured values [16, 36]. The relation between CSF velocity and pressure is complex. For Vol1 and P2, our study confirmed previous studies showing that peak flow coincides with minimum pressure drop and peak pressure drop with flow reversal [7, 21], while in P4 the pressure drop at peak flow ($\Delta p_{t_{Q_{\max}}}$) is substantial. A similar phase shift has also been reported previously in models with severe obstructions [34] or arachnoiditis [7].

Theoretically, phase shifts of the CSF pressure relative to the arterial blood pressure facilitates flow of CSF into the spinal cord tissue and thereby causes a one way valve mechanism [7]. As mentioned, we observed a phase shift of the pressure relative to the velocity in the presence of a severe stenosis. However, peak systolic flow occurred later in the cardiac cycle in the Chiari patients than in the control. This is in accordance with Bunck et al. [10] and indicate that although the obstruction does not cause a phase shift, the CSF pressure might

be delayed compared to the arterial pressure.

The systolic peak velocities and the Reynolds number in the aqueduct were similar to Kurtcuoglu et al. [20], who modeled pulsatile flow through the 3rd ventricle and aqueduct. Periods of flow in opposite directions in the SAS and 4th ventricle were consistent with Gupta et al. [14], but due to lower flow rate the velocities were lower in that study.

Under normal flow conditions, CSF flow in the aqueduct (Q_{Aq}) is delayed compared to flow in the cervical SAS (Q_{CS}) [4]. In the PCMR data used in the present study, the delay is smaller in the Chiari patients than in Vol1, which implies increased pulse wave velocities and decreased compliance. Increased CSF pulse wave velocity are consistent with Bunck et al. [10] and decreased compliance has been suggested to play a role in syrinx formation [1, 16].

6.4 Conclusion

By incorporating a larger portion of subject-specific anatomy, the present study aimed at bridging the gap formely seen between CFD models and 4D PCMR measurements. This is the first study to to reproduce flow jets and vortices seen in 4D PCMR. However, our simulations did not explain preferential CSF flow in the posterior cervical SAS.

The obstruction at the level of FM caused a phase shift of the pressure relative to the velocity in one patient. Peak systolic velocities and flow resistance distinguished the Chiari patients from the patient with normal flow conditions, while peak pressure drop distinguished the patient with the most severe obstruction from the patient with a moderate obstruction. Implicating that resistance and peak velocities are useful measures to identify an obstruction caused by the cerebellar tonsil herniation, while increased pressure drops across FM indicate the severity of the obstruction.

7 Acknowledgement

Thanks to Geir Ringstad and Søren Bakke at Rikshospitalet for providing MRI data. Thanks to Adrian and Ingeborg for segmenting the surface geometries. Thanks to Olivier Balédent for adding support of PCMR data from Siemens scanners to his software (www.tidam.fr) and to Øyvind Evju helping me navigate within `cbc.flow`.

Appendices

A Level set methods

A level set function is a deformable 3D function that evolves in time to find the surface/contour in the image with the largest gradient, which is then defined as the zero level. Inside the surface the level set function is negative and outside the function it is positive. Or defined in mathematical terms, the goal of level set methods is to identify a region Ω bounded by a surface Γ. This is achieved by introducing a scalar function $\phi(\mathbf{x}, t)$ with the properties

$$\phi(\mathbf{x}, t) > 0 \qquad \mathbf{x} \notin \Omega \tag{A.1}$$

$$\phi(\mathbf{x}, t) \leq 0 \qquad \mathbf{x} \in \Omega, \tag{A.2}$$

which implies that the surface Γ lies at the zero level set of $\phi(\mathbf{x}, t)$. The motion of the surface ϕ is given by

$$\frac{\partial \phi}{\partial t} + \mathbf{v} \cdot |\nabla \phi| \tag{A.3}$$

In this study the goal was to distinguish the CSF space from the brain tissue, i.e., we want to extract a surface representing the dura mater and the pia mater or brain tissue. In T2-weighted MR-images CSF appear bright with high signal intensity and tissue dark with a low signal intensity. The level set method takes advantage of the steep gradient in the signal intensity at the interface between tissue and CSF.

VMTK provides several level set methods within the `vmtklevelsetsegmentation` routine and in this study we used the method `colliding fronts`. In colliding fronts the initialization is done by placing two seeds on the image. One front from each seed will then propagate until they cross each other to form an initial surface. The propagation speed is proportional to the image intensity. To limit the extend of the surface an upper and/or lower threshold may be specified. The SAS has numerous small structures causing low signal and the image resolution are limited. As a result the initial surface created with `colliding fronts` have holes, and parts known to be anatomically connected may not. To fill in holes and connect thin passages we used the option `-seed` in the `vmtklevelsetsegmentation`, which is a manual segmentation procedure where the result is dependent on the visual evaluation of the user. After the initial surface has been created it is deformed according to Equation A.3 and there are four parameters the user can tweak to control

the deformation. First, you can specify the number of deformation steps or iterations, which should be large enough such that the surface do not change from one iteration to the next. Second, you can set a propagation scaling to inflate and a curvature scaling to regularize the initial surface. Finally, you can modify the advection scaling such that the final surface lies at the peak of $|\nabla\phi|$. To control the process and improve the result only a small region was segmented at the time and then merged into one final level set function, which were used to extract the surface, where the level set function was zero. The extracted surfaces and MR-images of Vol1 and P4 are displayed in Figure 4.1.

References

[1] N. Alperin, A. Sivaramakrishnan, , and T. Lichtor. Magnetic resonance imagingbased measurements of cerebrospinal fluid and blood flow as indicators of intracranial compliance in patients with chiari malformation. *J Neurosurg*, 103:46–52, 2005.

[2] L. Antiga, M. Piccinelli, L. Botti, B. Ene-Iordache, A. Remuzzi, and D. A. Steinman. An image-based modeling framework for patient-specific computational hemodynamics. *Medical & biological engineering & computing*, 46(11):1097–1112, 2008.

[3] R. A. Armonda, C. M. Citrin, T. Foley, and R. G. Ellenbogen. Quantitative cine-mode magnetic resonance of Chiari I malformation: An analysis of cerebrospinal fluid dynamics. *Neurosurgery*, 35(2):214–224, 1994.

[4] O. Balédent. *Adult Hydrocephalus*, chapter Imaging of the cerebrospinal fluid circulation, pages 121–138. Cambridge university press, 2014.

[5] O. Balédent, M. C. Henry-Feugeas, and I. Idy-Peretti. Cerebrospinal fluid dynamics and relation with blood flow: a magnetic resonance study with semiautomated cerebrospinal fluid segmentation. *Investigative radiology*, 36(7):368–377, 2001.

[6] R. A. Bhadelia, A. R. Bogdan, S. M. Wolpert, S. Lev, B. A. Appignani, and C. B. Heilman. Cerebrospinal fluid flow waveforms: Analysis in patients with Chiari I malformation by means of gated phase-contrast MR imaging velocity measurements. *Radiology*, 196:195–202, 1995.

[7] L. E. Bilston, M. A. Stoodley, and D. F. Fletcher. The influence of the relative timing of arterial and subarachnoid space pulse waves on spinal

perivascular cerebrospinal fluid flow as a possible factor in syrinx development. *Journal of neurosurgery*, 112(4):808–13, 2010. ISSN 1933-0693. doi: 10.3171/2009.5.JNS08945.

[8] I. G. Bloomfield, I. H. Johnston, and L. E. Bilston. Effects of proteins, blood cells and glucose on the viscosity of cerebrospinal fluid. *Pediatr Nerosurg*, 28:246–251, 1998.

[9] A. C. Bunck, J.-R. Kröger, A. Jüttner, A. Brentrup, B. Fiedler, F. Schaarschmidt, G. R. Crelier, W. Schwindt, W. Heindel, T. Niederstadt, and D. Maintz. Magnetic resonance 4d flow characteristics of cerebrospinal fluid at the craniocervical junction and the cervical spinal canal. *European radiology*, 21(8):1788–1796, 2011.

[10] A. C. Bunck, J. R. Kroeger, A. Juettner, A. Brentrup, B. Fiedler, G. R. Crelier, B. Martin, W. Heindel, D. Maintz, W. Schwindt, and T. Niederstadt. Magnetic resonance 4D flow analysis of cerebrospinal fluid dynamics in Chiari I malformation with and without syringomyelia. *European radiology*, 22(9):1860–70, 2012. ISSN 1432-1084. doi: 10.1007/s00330-012-2457-7.

[11] P. K. Eide. Comparison of simultaneous continuous intracranial pressure (ICP) signals from icp sensors placed within the brain parenchyma and the epidural space. *Medical engineering & physics*, 30(1):34–40, 2008. ISSN 1350-4533. doi: 10.1016/j.medengphy.2007.01.005.

[12] D. Enzmann and N. J. Pelc. Normal flow patterns of intracranial and spinal cerebrospinal fluid defined with phase-contrast cine MR imaging. *Radiology*, 178:467–474, 1991.

[13] D. Greitz, K. Ericson, and O. Flodmark. Pathogenesis and mechanics of spinal cord cysts. *International Journal of Neuroradiology*, 5(2):61–78, 1999.

[14] S. Gupta, M. Soellinger, P. Boesiger, D. Poulikakos, and V. Kortcuoglu. Three-dimensional computational modeling of subject-specific cerebrospinal fluid flow in the subarachnoid space. *Journal of Biomedical Engineering*, 131, 2009.

[15] S. Gupta, M. Soellinger, D. M. Grzybowski, P. Boesiger, J. Biddiscombe, D. Poulikakos, and V. Kurtcuoglu. Cerebrospinal fluid dynamics in the

human cranial subarachnoid space: an overlooked mediator of cerebral disease. I. computational model. *Journal of The Royal Society Interface*, 7 (49):1195–1204, 2010.

[16] J. D. Heiss, N. Patronas, H. L. DeVroom, T. Shawker, R. Ennis, W. Kammerer, A. Eidsath, T. Talbot, J. Morris, E. Eskioglu, and E. H. Oldfield. Elucidating the pathophysiology of syringomyelia. *Journal of Neurosurgery*, 91:553–562, 1999.

[17] A. Helgeland, K.-A. Mardal, V. Haughton, and B. A. Pettersson Reif. Numerical simulations of the pulsating flow of cerebrospinal fluid flow in the cervical spinal canal of a Chiari patient. *Journal of Biomechanics*, 2014.

[18] S. Hentschel, K. A. Mardal, A. E. Løvgren, S. O. Linge, and V. Haughton. Characterization of cyclic CSF flow in the foramen magnum and upper cervical spinal canal with MR flow imaging and computational fluid dynamics. *American Journal of Neuroradiology*, 31:997–1002, 2010.

[19] B. J. Iskandar, M. Quigley, and V. Haughton. Foramen magnum cerebrospinal fluid flow characteristics in children with Chiari I malformation before and after decompression. *Journal of Neurosurgery*, 60:707–711, 2004.

[20] V. Kurtcuoglu, M. Soellinger, P. Summers, K. Boomsma, D. Poulikakos, P. Boesiger, and Y. Ventikos. Computational investigation of subject-specific cerebrospinal fluid flow in the third ventricle and aqueduct of sylvius. *Journal of biomechanics*, 40(6):1235–1245, 2007.

[21] S. O. Linge, V. Haughton, A. E. Løvgren, K. A. Mardal, and H. P. Langtangen. CSF flow dynamics at the craniovertebral junction studied with an idealized model of the subarachnoid space and computational flow analysis. *American Journal of Neuroradiology*, 31:185–192, 2010.

[22] S. O. Linge, V. Haughton, A. E. Løvgren, K. A. Mardal, A. Helgeland, and H. P. Langtangen. Effect of tonsillar herniation on cyclic CSF flow studied with computational flow analysis. *AJNR. American journal of neuroradiology*, 32(8):1474–81, Sept. 2011. ISSN 1936-959X. doi: 10.3174/ajnr.A2496.

[23] A. Logg, K. A. Mardal, and G. Wells, editors. *Automated Solution of Differential Equations by the Finite Element Method*, volume 84 of *Lecture Notes in Computational Science and Engineering*. Springer, 2012. ISBN 978-3-642-23098-1. doi: 10.1007/978-3-642-23099-8.

[24] F. Loth, M. A. Yardimci, and N. Alperin. Hydrodynamic modeling of cerebrospinal fluid motion within the spinal cavity. *ASME J. Biomech. Engrg.*, 123:71–73, 2001. doi: 10.1115/1.2801670.

[25] B. A. Martin, W. Kalata, N. Shaffer, P. Fischer, M. Luciano, and F. Loth. Hydrodynamic and longitudinal impedance analysis of cerebrospinal fluid dynamics at the craniovertebral junction in type I Chiari malformation. *PloS one*, 8(10):e75335, 2013.

[26] M. Mortensen, K. A. Mardal, S. H. Pahlavian, and B. A. Martin. Preliminary study of the impact of spinal cord nerve roots and denticulate ligaments on drug movement in the cervical spinal subarachnoid space. In *Proceedings of the 26th Nordic Seminar on Computational Mechanics*, 2013.

[27] G. Pinna, F. Alessandrini, A. Alfieri, M. Rossi, and A. Bricolo. Cerebrospinal fluid flow dynamics study in Chiari I malformation: implications for syrinx formation. *Neurosurgical Focus*, 8, 2000.

[28] M. F. Quigley, B. J. Iskandar, M. A. Quigley, M. N. Nicosia, and V. Haughton. Cerebrospinal fluid flow in foramen magnum: Temporal and spatial patterns at MR imaging in volunteers and in patients with Chiari I malformation. *Radiology*, 232:229–232, 2004.

[29] G. Rutkowska, V. Haughton, S. Linge, and K. A. Mardal. Patient-specific 3D simulation of cyclic CSF flow at the craniocervical region. *AJNR. American Journal of Neuroradiology*, 33(9):1756–62, 2012. ISSN 1936-959X. doi: 10.3174/ajnr.A3047.

[30] N. Shaffer, B. Martin, and F. Loth. Cerebrospinal fluid hydrodynamics in type I Chiari malformation. *Neurological research*, 33(3):247–60, 2011. ISSN 1743-1328. doi: 10.1179/016164111X12962202723805.

[31] N. Shaffer, B. A. Martin, B. Rocque, C. Madura, O. Wieben, B. Iskandar, S. Dombrowski, M. Luciano, J. N. Oshinski, and F. Loth. Cerebrospinal fluid flow impedance is elevated in type I Chiari malformation. *Journal of Biomechanical Engineering*, Accepted Manuscript, 2013. doi: doi:10.1115/1.4026316.

[32] S. Shah, V. Haughton, and A. M. del Río. CSF flow through the upper cervical spinal canal in Chiari I malformation. *American Journal of Neuroradiology*, 32(6):1149–1153, 2011.

[33] H. W. Stockman. Effect of anatomical fine structure on the flow of cerebrospinal fluid in the spinal subarachnoid space. *Journal of biomechanical engineering*, 128(1):106–114, 2006.

[34] K. H. Støverud, H. P. Langtangen, V. Haughton, and K. A. Mardal. CSF pressure and velocity in obstructions of the subarachnoid spaces. *NRJ Digital*, 3(5):163–171, 2013.

[35] B. Williams. Cerebrospinal fluid pressure changes in response to coughing. *Brain*, 99:331–346, 1976.

[36] B. Williams. Simultaneous cerebral and spinal fluid pressure recordings. I. technique, physiology, and normal results. *Acta Neurochir (Wien)*, 58(3-4): 167–85, 1981.

[37] T. I. Yiallourou, J. R. Kröger, N. Stergiopulos, D. Maintz, B. Martin, and A. C. Bunck. Comparison of 4d phase-contrast MRI flow measurements to computational fluid dynamics simulations of cerebrospinal fluid motion in the cervical spine. *PloS one*, 7(12):e52284, 2012. ISSN 1932-6203. doi: 10.1371/journal.pone.0052284.